

# Experimental study of pionic fusion $4\text{He}(3\text{He},\pi^0)^7\text{Be}$

---

Gašparić, Igor

Doctoral thesis / Disertacija

2011

Degree Grantor / Ustanova koja je dodijelila akademski / stručni stupanj: **University of Zagreb, Faculty of Science / Sveučilište u Zagrebu, Prirodoslovno-matematički fakultet**

Permanent link / Trajna poveznica: <https://um.nsk.hr/um:nbn:hr:217:671706>

Rights / Prava: [In copyright](#)/[Zaštićeno autorskim pravom.](#)

Download date / Datum preuzimanja: **2024-11-29**



Repository / Repozitorij:

[Repository of the Faculty of Science - University of Zagreb](#)





**University of Zagreb**  
Faculty of Science  
Department of Physics

Igor Gašparić

**Experimental study of pionic  
fusion  ${}^4\text{He}({}^3\text{He}, \pi^0){}^7\text{Be}$**

Doctoral Thesis

Zagreb, 2011



**Sveučilište u Zagrebu**  
Prirodoslovno-matematički fakultet  
Fizički odsjek

Igor Gašparić

**Eksperimentalno proučavanje  
pionske fuzije  ${}^4\text{He}({}^3\text{He}, \pi^0){}^7\text{Be}$**

Doktorski rad

Zagreb, 2011.



**University of Zagreb**  
Faculty of Science  
Department of Physics

Igor Gašparić

**Experimental study of pionic  
fusion  ${}^4\text{He}({}^3\text{He}, \pi^0){}^7\text{Be}$**

Doctoral Thesis

Supervisor:  
Prof.dr.sc. Roman Čaplar

Zagreb, 2011



**Sveučilište u Zagrebu**  
Prirodoslovno-matematički fakultet  
Fizički odsjek

Igor Gašparić

**Eksperimentalno proučavanje  
pionske fuzije  ${}^4\text{He}({}^3\text{He}, \pi^0){}^7\text{Be}$**

Doktorski rad

Mentor:  
Prof.dr.sc. Roman Čaplar

Zagreb, 2011.

# Acknowledgements/Zahvale

This work would not be done without help of many colleagues, friends, and family.

I would like to thank my thesis supervisor Prof. Roman Čaplar for his guidance and support during this long time of my graduate study. I am also grateful for freedom and encouragement to work on other projects which, although being sometimes stressful, allowed me to gain more knowledge and skills. I had incredible luck to have had two great teachers - Prof. Herbert Löhner and Dr. Jose Bacelar. My warmest gratitude goes to Herbert whose knowledge, determination, precision, and clarity were most helpful in my work from the beginning in the detector lab to the careful reading of the manuscript. Jose's sharp and humorous comments, apart from being extremely useful in the experiment and in the data analysis, created a positive atmosphere and made me really enjoy this work. I also express my thanks to Prof. Matko Milin, Prof. Slobodan Brant, Prof. Dubravko Klabučar, and Prof. Nils Paar for participation in the evaluation committee of my thesis.

My special thanks go to Dr. Mladen Kiš who introduced me to the experimental nuclear physics and has done enormous work to get the Plastic Ball detector working. He always had the right answers to all of my question related to the experimental techniques and equipment. Mladene, hvala ti najljepša na svemu, a posebno za onaj neformalni dio koji dolazi uz ovaj posao.

Nuclear physics experiments cannot be prepared and carried out without involvement of many colleagues. Here I would like to thank Leila who as a PhD student spent long hours in the experimental hall with me. I am especially thankful to Nasser and Johan for their constructive participation in the experiment and the pleasant company. I acknowledge taking part in the experiment of my colleagues: Hamid, Ela, Hosein Mardanpour, Sugat, Ahmad, Mohammad, and Hossein Moeni. I am indebted to the technical staff of the KVI for the effort made in the preparation of the experiment.

Posebno bih zahvalio voditelju Laboratorija za nuklearnu fiziku, dr. Zoranu Basraku na njegovoj beskrajnoj podršci, savjetima i ohrabrivanju tijekom mog doktorskog studija. Nadalje, zahvalio bih Suzani, Miloradu, Branimiru, Saši, Zdenki, Ljiljani, Darku, odbojkaškoj i košarkaškoj ekipi te ostalim kolegama i prijateljima s Instituta Ruđer Bošković na ugodnom i zabavnom društvu.

Velika hvala mojim starim prijateljima Dejanu, Juri, Marku, Hrvoju, Hrvoju i Hrvoju na beskonačnim ludim raspravama, neprekidnom zadirivanju i podršci. Posebno se "zahvaljujem" Dejanu na savjetima prilikom izbora fakulteta i na njegovoj "pedagoškoj" podršci u mom poslu.

I najvažnije, zahvaljujem svojoj prekrasnoj obitelji bez koje sve ovo ne bi imalo smisla - supruzi Renati i djeci Petru, Dori i Lovri na njihovoj velikoj ljubavi, razumijevanju i odricanju. Velika hvala i Renatinim i mojim roditeljima za neumornu i beskrajnu podršku.

## Experimental study of pionic fusion ${}^4\text{He}({}^3\text{He}, \pi^0){}^7\text{Be}$

Igor Gašparić

Ruđer Bošković Institute, Bijenička 54, Zagreb

Pionic fusion reactions where two nuclei fuse into a new one by emitting a pion need a highly coherent mechanism and therefore give an insight into the collective motion of nucleons in nuclei. The reaction  ${}^4\text{He}({}^3\text{He}, \pi^0){}^7\text{Be}$  has been studied experimentally at beam energies about 10 MeV above the coherent production threshold.

The experiment was performed at KVI, Groningen using the AGOR accelerator facility. The created nuclei were detected in a phoswich detector array in the focal plane of the Big-Bite Spectrometer in coincidence with the photons from neutral pion decay which were detected in the Plastic Ball detector. The Plastic Ball contains 552 phoswich detectors covering polar laboratory angles  $50^\circ < \theta < 160^\circ$  in almost the full azimuthal range. To improve the photon detection efficiency an active inner shell of 64 CsI(Tl) crystals is put inside the Plastic Ball.

The fused nuclei are identified by a pulse-shape analysis and a time-of-flight measurement. They are clearly correlated with two photons detected in the Plastic Ball at mutually large opening angles corresponding to pion decay. The event selection yields approximately 500 background-free pionic fusion events. The pion angular distribution is corrected for the acceptance and the efficiency obtained from Monte Carlo simulations and normalized with the beam current. The measured differential cross section is compared to available theoretical calculations. The Legendre polynomial fit gives the total cross section  $\sigma = (53 \pm 9)$  nb.

Keywords: pionic fusion, subthreshold pion production, CsI(Tl) scintillator, phoswich, magnetic spectrometer  
Supervisor: Prof. dr. sc. Roman Čapljar (IRB)  
Reviewers: Prof. dr. sc. Matko Milin (PMF), Prof. dr. sc. Roman Čapljar (IRB), Prof. dr. sc. Herbert Löhner (KVI, Groningen), Prof. dr. sc. Nils Paar (PMF), Prof. dr. sc. Dubravko Klabučar (PMF)  
Thesis accepted: 14.6.2011



## **Eksperimentalno proučavanje pionske fuzije ${}^4\text{He}({}^3\text{He}, \pi^0){}^7\text{Be}$**

Igor Gašparić

Institut Ruđer Bošković, Bijenička 54, Zagreb

Reakcija pionske fuzije u kojoj se dvije jezgre fuzioniraju u novu emitirajući pritom pion, zahtijeva veoma koherentni mehanizam i stoga pruža uvid u kolektivno gibanje nukleona u jezgri. Reakcija  ${}^4\text{He}({}^3\text{He}, \pi^0){}^7\text{Be}$  je eksperimentalno proučavana na energiji snopa od oko 10 MeV iznad praga.

Eksperiment je izveden na KVI-u, u Groningenu na akceleratoru AGOR. Stvorene jezgre su opažene pomoću niza *phoswich* detektora u fokalnoj ravnini Big-Bite spektrometra istovremeno s fotonima proizašlim iz raspada neutralnog piona i detektiranim u Plastic Ball detektoru. Plastic Ball sadrži 552 *phoswich* detektora koji pokrivaju laboratorijste polarne kuteve  $50^\circ < \theta < 160^\circ$  u gotovo cijelom azimutalnom rasponu. Da bi se poboljšala efikasnost detekcije fotona unutar Plastic Ball detektora postavljena su 64 kristala CsI(Tl).

Složena jezgre su identificirane analizom oblika signala i mjerenjem vremena proleta. One su korelirane s dva fotona opažena u Plastic Ball detektoru s velikim kutem između njihovih smjerova što odgovara raspadu piona. Izborom događaja dobije se oko 500 događaja pionske fuzije bez pozadine. Kutna raspodjela piona je korigirana prema akceptanciji i efikasnosti koje su dobivene iz simulacija i normalizirane prema struji snopa. Mjereni diferencijalni udarni presjek uspoređen je s postojećim teorijskim proračunima. Prilagodba na red Legendreovih polinoma daje za ukupni udarni presjek  $\sigma = (53 \pm 9)$  nb.

Ključne riječi: pionska fuzija, stvaranje piona ispod praga, CsI(Tl) scintilator, phoswich, magnetski spektrometar  
Mentor: prof. dr. sc. Roman Čaplar (IRB)  
Ocjenjivači: prof. dr. sc. Matko Milin (PMF), prof. dr. sc. Roman Čaplar (IRB), prof. dr. sc. Herbert Löhner (KVI, Groningen), prof. dr. sc. Nils Paar (PMF), prof. dr. sc. Dubravko Klabučar (PMF)  
Rad prihvaćen: 14.6.2011.

# Extended abstract in Croatian

## Uvod

### Nuklearna fizika i pion

Atomska jezgra i nukleoni proučavaju se već cijelo jedno stoljeće. Otkriveno je da nukleoni također imaju strukturu i da je sila koja djeluje između njih zapravo rezidualno međudjelovanje elementarnih čestica kvarkova koji izmjenjuju gluone. Njihovo ponašanje je dobro opisano kvantnom kromodinamikom (QCD) na visokim energijama. Na nižim energijama, koje karakteriziraju pojave vezane uz atomsku jezgru, QCD je neperturbativna i stoga teško primjenjiva. Kvarkovi nisu izolirani već se pojavljuju u grupama od po tri kvarka u barionima ili kao parovi kvarka i antikvarka u mezonima. Pojave u nuklearnoj fizici do energija pobuđenja od 1 GeV najefikasnije se opisuju pomoću bariona i mezona koji su relevantni stupnjevi slobode u ovom području energija.

Inspiriran uspjehom kvantne elektrodinamike, Yukawa je 1935 godine predložio silu izmjene između nukleona preko čestice konačne mase budući da je ta sila konačnog doseg. Kasnije su te čestice - pioni - otkrivene u kozmičkim zrakama i stvorene u laboratoriju.

Postoje tri vrste piona:  $\pi^0$ ,  $\pi^+$  i  $\pi^-$  i oni odgovaraju trima stanjima čestice izospina 1. Nabijeni pioni raspadaju se slabom silom sporo i mogu biti opaženi direktno dok se neutralni pioni raspadaju elektromagnetski u dva fotona još u meti i mogu se opaziti indirektno preko istovremene detekcije ta dva fotona.

## Stvaranje piona u nuklearnim reakcijama

Pion je sastavni dio svih pojava u nuklearnoj fizici budući da nukleoni međudjeluju izmjenom virtualnog piona. Da bi se više saznalo o toj sili potrebno je proučavati i procese u kojima se javlja i realni pion. Nuklearne reakcije u kojima nastaju pioni proučavaju se u velikom opsegu energija i različitih kombinacija projektila i meta. Može se proučavati sam mehanizam nastanka piona ili se pion koristi kao proba za dobivanje informacija o npr. strukturi atomske jezgre ili odvijanju sudara teških iona. Jednako su interesantna istraživanja vezana uz elementarnu interakciju piona i nukleona kao i proučavanje sustava velikog broja nukleona.

U bilo kojoj nuklearnoj reakciji ako je dovoljno energije na raspolaganju i ako izborna pravila ne zabranjuju, može se stvoriti pion. U sudaru dvaju nukleona u kojem jedan nukleon miruje potrebna je kinetička energija od 290 (280) MeV za stvaranje nabijenog (neutralnog) piona. Vezanjem piona i nukleona dominira pobuđenje  $\Delta$  rezonancije - pobuđenog stanja nukleona spina  $3/2$ , izospina  $3/2$  i mase 1232 MeV. Budući da je za pobuđenje  $\Delta$ -rezonancije potrebna energija od oko 150 MeV, na niskim energijama su važniji drugi mehanizmi poput interakcije u s-valu kao i nerezonantog pseudovektorskog  $\pi NN$  vezanja.

Pioni stvoreni u sudaru jezgara, jako međudjeluju s nukleonima tih jezgara prije nego napuste reakcijsku zonu. Time omogućuju istraživanje svojstava nuklearne tvari kao što su jednadžba stanja nuklearne tvari ili moguće promjene svojstava i međudjelovanja bariona uronjenih u nuklearni medij. Stvaranje piona u takvim sudarima na energijama oko energije praga stvaranja piona u elementarnom sudaru dvaju nukleona dobro je opisano dominantnim kanalom, tj.  $\Delta$  rezonancijom.

Za reakcije stvaranja piona karakterističan je veliki prijenos količine gibanja što znači da je vrlo važan doprinos kratkodosežnih sila između nukleona. Opis tog prijenosa količine gibanja je vrlo velik izazov za modele temeljene na kiraloj perturbacijskoj teoriji. U posljednje vrijeme taj je pristup dominantan u teorijskom istraživanju sile između nukleona.

Također je moguće stvoriti pion na energijama nižim od 280 MeV po

nukleonu, ali za to je potrebno kolektivno djelovanje više od dva nukleona. Najizravnije objašnjenje ove pojave je bilo to da nukleoni unutar projektila i mete izvode fermijevo gibanje koje se superponira na relativno gibanje projektila i mete pa relativno gibanje dvaju nukleona iz projektila i mete može imati energiju veću od praga stvarnja piona. Međutim, uz ovu pretpostavku postavljena je granica od 50 A MeV ispod kojeg bi stvaranje piona bilo nemoguće. Eksperimenti su pokazali da je stvaranje piona moguće i na puno nižim energijama pa čak i do same kinematičke granice. Brojni modeli su razvijeni kako bi se objasnila ova pojava. Svi su morali sadržavati neki kolektivni mehanizam da bi mogli opisati nastanak piona ispod pretpostavljene granice, ali i puno veće izmjerene udarne presjeke u "dozvoljenom" području.

## Pionska fuzija

Ekstreman primjer stvaranja piona u području ispod praga stvaranja u osnovnom sustavu dva nukleona je pionska fuzija. U toj reakciji svi nukleoni moraju doprinijeti i uložiti svoju kinetičku energiju kako bi se stvorio pion. Uz pion nastaje i jezgra u osnovnom ili nekom nisko pobuđenom stanju. To stanje je određeno kvantnim brojevima spina, pariteta i izospina što omogućava selekciju određenog izlaznog kanala, jednostavniju analizu i jasniji uvid u mehanizam reakcije.

Motivacija za proučavanje ovakve reakcije je dvojaka. S jedne strane potrebno je pronaći mehanizam koji će izbjeći termalizaciju sustava i svu raspoloživu energiju početnog gibanja pretvoriti u jedan stupanj slobode. Taj mehanizam se mora temeljiti na osnovnom procesu s dva nukleona koji je i sam predmet intenzivnog istraživanja. S druge strane struktura nastale jezgre ima kritičnu ulogu jer svi nukleoni moraju sudjelovati. Osobito je važna valna funkcija za velike količine gibanja zbog velikog prijenosa količine gibanja u reakcijama nastanka piona.

Prve reakcije pionske fuzije opažene su početkom sedamdesetih u reakcijama s protonima. Nešto kasnije opažena je i pionska fuzija s jezgrama helija. Za razliku od reakcija  $A(p,\pi)A+1$  eksperimentalnih podataka s kom-

pleksnijim projektilima nema baš mnogo. Eksperimentalni rezultati potakli su razvoj nekoliko modela pionske fuzije.

Budući da je pionska fuzija reakcija u kojem nastaju dva tijela, za određivanje kinematike reakcije potrebno je izmjeriti samo jednu kinetičku varijablu, npr. kut piona prema snopu. Eksperimenti napravljeni do sada (tab. 1.1) detektiraju ili pion ili nastalu jezgru u spektrometru. Za detekciju nastale jezgre potrebno je samo detektorom pokriti uski stožac oko smjera snopa jer je ta jezgra kinematički ograničena na to područje. S druge strane teški ion pati od velikih gubitaka energije pri prolasku kroz materijal (npr. kroz metu).

## Skica ovog rada

U sljedećem poglavlju prikazana je teorijska podloga za proučavani proces. To uključuje opis kinematike i izbornih pravila. Spomenuti su mehanizmi osnovnog procesa. Modeli koji opisuju reakciju koja se mjerila u ovom eksperimentu detaljnije su predstavljani. Eksperimentalni postav opisan je u trećem poglavlju. Naglasak je stavljen na detektore koji su u ovom eksperimentu prvi puta korišteni. Simulacije koji su nezaobilazni dio ove analize prikazane su u četvrtom poglavlju. Nakon toga, slijedi analiza podataka od kalibracije detektora do izvrjednjavanja konačnih udarnih presjeka. U predzadnjem poglavlju prikazani su konačni rezultati te uspoređeni s predviđanjima modela i ostalim eksperimentalnim podacima. Zadnje poglavlje donosi zaključke.

# Teorijska podloga

## Kinematika i izborna pravila

Osnovna ograničenja na kinematiku reakcije postavljena su zakonima sačuvanja količine gibanja i energije. Osim toga, zbog dodatnih simetrija koje poštuje jaka sila, veličine poput ukupnog momenta količine gibanja, pariteta i izospina moraju biti sačuvane.

Pion ne može biti stvoren iz samo jednog nukleona. Da bi se kompenzerala promjena količine gibanja nastala pretvorbom kinetičke energije u novu česticu, potreban je još barem jedan nukleon. U međudjelovanju dvaju nukleona, količina gibanja i energija su raspodjeljeni tako da su zakoni sačuvanja zadovoljeni.

Za elementarni proces nastanka neutralnog piona dobiva se iz zakona sačuvanja energije i količine gibanja minimalna kinetička energija snopa od 280 MeV. Dva nukleona kao čestice sa spinom  $\frac{1}{2}$  mogu biti u stanju ukupnog spina 0 ili 1. Taj se spin veže s orbitalnim momentom količine gibanja njihovog relativnog gibanja i gibanja piona u ukupni moment količine gibanja. Ukupni moment količine gibanja u reakciji je sačuvan. Slično razmatranje vrijedi i za izospin.

U slučaju pionske fuzije isto tako moraju biti zadovoljeni zakoni sačuvanja. Kinetička energija snopa po nukleonu potrebna za stvaranje piona manja je od 280 MeV. Osnovna stanja projektila  ${}^3\text{He}$  i mete  ${}^4\text{He}$  su  $\frac{1}{2}^+$  i  $0^+$ . Stanje piona je  $0^-$ . Energija snopa je 258 MeV što daje višak energije od 12 MeV u sustavu centra mase u konačnom stanju. Budući da se u ovom eksperimentu detektira jezgra  ${}^7\text{Be}$ , stanja koja su nestabilna s obzirom

na emisiju čestica se ne detektiraju. Dakle, ostaju samo moguća dva konačna stanja - osnovno stanje  $\frac{3}{2}^-$  i prvo pobuđeno stanje  $\frac{1}{2}^-$  na energiji od 0.43 MeV. Ta stanja su vrlo bliska i korišteni eksperimentalni postav ih ne može razlučiti. Slični eksperimenti samo sa izobarnim analogonom  ${}^7\text{Li}$  su izvedeni ranije i modeli su uzeli u obzir da se ta stanja ne mogu razlučiti pa su proračuni napravljeni za oba stanja zajedno.

## Udarni presjek

U ovom odjeljku su prikazane osnovne formule za udarni presjek. Diferencijalni udarni presjek za pionsku fuziju osnovna je observabla koja se koristi za uspoređivanje teorije i eksperimentalnih rezultata. Budući da su u konačnom stanju dvije čestice i snop nije polariziran, diferencijalni udarni presjek je funkcija samo jedne kinematičke varijable (polarnog kuta piona dok o azimutalnom ne ovisi). Sastoji se od dijela koji ovisi o faznom prostoru, odnosno o kinematici i dijela koji ovisi o dinamici reakcije. Dinamika je opisana amplitudom prijelaza između početnog stanja opisanog relativnim gibanjem projektila i mete, te njihovom internom strukturom i konačnog stanja opisanog valnom funkcijom nastale jezgre i gibanja piona.

## Međudjelovanje piona i nukleona

Temelj međudjelovanja piona i nukleona je  $\pi\text{NN}$  vezanje čiji parametri su određeni prilagodbom na eksperimentalne podatke za elastično raspršenje piona na nukleonima. Raspršenje piona na nukleonima na malim energijama uključuje raspršenje u stanju parcijalnog vala s, nerezonantno raspršenje u p-valu i rezonantno raspršenje u p-valu preko  $\Delta$ -rezonancije. Zadnji mehanizam je dominantan osim pri vrlo niskim energijama gdje s-val dolazi do izražaja.

Na energijama većim od praga stvaranja piona gore spomenuti mehanizmi su uključeni s tim da zbog zakona sačuvanja moraju oba nukleona sudjelovati u interakciji. Vrlo važno je u opis uključiti međudjelovanja nukleona u

početnom i konačnom stanju. Osim toga, bez interakcije nukleona u početnom ili konačnom stanju stvaranje piona u procesu koji uključuje samo jedan nukleon ( $\pi NN$  nerezonantno pseudovektorsko vezanje) je nemoguće.

Pokazalo se da ovi osnovni mehanizmi ne opisuju dobro udarne presjeke za procese nastajanja piona pri pragu nastajanja pa su uključeni dodatni - izmjena težih mezona i raspršenje u s-valu za pione izvan masene ljuske. Svi postojeći modeli pionske fuzije koriste samo dominante mehanizme nerezonantnog ili rezonantnog stvaranja piona u p-valu. Uključivanje svih mogućih mehanizama pokazalo bi kako oni utječu na proces pionske fuzije. Prema dosadašnjim rezultatima doprinosi tih mehanizama su maleni, čak i na vrlo niskim energijama malo iznad praga stvaranja.

## Modeli pionske fuzije

Pionska fuzija je specifična reakcija jer zahtijeva doprinos svih nukleona u reakciji. Pritom je stvorena jezra u vezanom stanju točno određenih kvantnih brojeva odnosno valne funkcije. Pitanje je kako konstruirati kolektivni mehanizam iz elementarnih NN reakcija koji će efikasno zaobići termalizaciju, odnosno raspodjelu energije po svim nukleonima i usmjeriti je u stvaranje samo jedne čestice - piona.

Kao što se vidi, dva su važna aspekta reakcije pionske fuzije: koherentni mehanizam i struktura jezgara u ulaznom kanalu kao i njihovo relativno gibanje, te struktura jezgre u konačnom stanju. Posebnost ove reakcije je veliki prijenos količine gibanja s početnog stanja na konačno. Na to je osobito osjetljiv dio valne funkcije u području visokih količina gibanja.

Prva opažanja ekskluzivnog stvaranja piona u reakcijama s lakim jezgrama potaknula su razvoj modela koji će biti opisani i korišteni za usporedbu mjerenjima. Budući da do sada nije napravljeno mjerenje reakcije  ${}^4\text{He}({}^3\text{He}, \pi^0){}^7\text{Be}$ , većina modela se nije bavila tom reakcijom. Međutim izmjerena je reakcija  ${}^4\text{He}({}^3\text{He}, \pi^+){}^7\text{Li}$  koja je s prijašnjom vezana izospinskom simetrijom pa se uz pretpostavku zanemarivog narušenja te simetrije, mogu modeli jednostavno prilagoditi.



## Prijelazno pobuđenje $\Delta$ -rezonancije

Prvi model koje je predložen temelji se na pobuđenju  $\Delta$ -rezonancije unutar jezgre [61], kao privremene pohrane energije i zaobilaznice termalizacije sustava.  $\Delta$ -rezonancija se jako veže na sustav piona i nukleona i raspada se u njih. Za pobuđivanje slobodne  $\Delta$ -rezonancije potrebna je energija koja je veća od rapoložive, ali stvaranje vezanog stanja jezgri snižava energiju prijelaznog stanja što omogućava odvijanje reakcije.

Proces se odvija u tri koraka. Prvi je tzv. "paljenje" u kojem dolazna jezgra usporava zbog interacija između nukleona iz projektila i mete. Time se relativno kolektivno gibanje pretvara u kolektivno pobuđenje  $\Delta$ -bariona vezanog u jezgri. Stvorena  $\Delta$ -rezonancija propagira kroz jezgru preko mogućih stanja. Za olakšanje računa, energije tih stanja su usrednjene. Zatim se pobuđeno stanje raspada na pion i konačnu jezgru u osnovnom ili prvom pobuđenom stanju. Valna funkcija konačnog stanja sastoji se od grozdova koji odgovaraju projektilu i meti i koji su vezani unutar novonastale jezgre. Takve strukture su preferirane u ovakvoj reakciji.

Zbog izospinske simetrije, ovaj se model može primijeniti na sličnu reakciju koja se ovdje proučava.

## Poluempirički model

Drugi model opisuje reakciju pomoću jednostavnije reakcije [64]. Pretpostavlja da proton iz mete međudjeluje s projektilom stvarajući pion i alfa-česticu. Za tu reakciju postoje mjereni udarni presjeci koji se iskoriste za dobivanje amplitude prijelaza. Ta se amplituda prijelaza uključuje u amplitudu prijelaza kompleksne reakcije zajedno s operatorima koji stvaraju međustanje i konačnu jezgru. Ovaj model također koristi grozdastu strukturu jezgre koja nastaje u reakciji.

## Model međudjelujućih grozdova

Za razliku od prethodna dva modela, model međudjelujućih grozdova [67] uvodi i jake korelacije među njima, međudjelovanja u početnom stanju i

Paulijev princip. U ovom modelu operator koji se koristi za stvaranje piona je nerezonantno pseudovektorsko vezanje piona i nukleona u obliku invarijantnom na Galilejeve transformacije. Ostali mehanizmi poput pobuđenja  $\Delta$ -rezonancije su zanemareni.

Usporedba rezultata dobivenih s grozdastom valnom funkcijom i valnom funkcijom iz modela ljustaka pokazuje kako iz modela međudjelujućih grozdova proizlazi udarni presjek veći za red veličine od onog iz modela ljustaka. Također pokazuje da je dominantan mehanizam stvaranja piona na projektilskom klasteru. Relativno gibanje grozdova s velikom relativnom količinom gibanja bitno je za povećanje udarnog presjeka u odnosu na onaj iz modela ljustaka.

# Eksperimentalni postav

Eksperiment je izveden na Kernfysisch Versneller Instituut (KVI) u Groningenu u Nizozemskoj sa snopom  $^3\text{He}$  iz akceleratora AGOR. Eksperimentalni postav (sl. 3.2) uključuje detektor Plastic Ball (PB) koji je već ranije korišten u nizu eksperimenata na KVI-u i izvan njega kao i KVI-ov magnetski spektrometar Big-Bite Spectrometer (BBS). Novi detektori Inner Shell (IS) i Heavy-Ion (HI) napravljeni su posebno za eksperimente s pionskom fuzijom.

## Meta od tekućeg helija

Da bi se postigao visoki luminozitet, korištena je meta od tekućeg helija proizvedena na KVI-u. Sastoji se od spremnika u kojem je tekući helij na 4 K i koji se neprestano dovodi iz velikog spremnika (dewar). Niža temperatura oko 2 K u spremniku mete postiže se ispumpavanjem. Meta od tekućeg helija nalazi se u malom aluminijskom cilindru zatvorenom s tankim folijama od mylara. Debljina mete od  $135 \text{ mg/cm}^2$  ozbiljan je problem koji zahtijeva posebnu pažnju prilikom analize podataka.

## Magnetski spektrometar Big-Bite Spectrometer

Spektrometar BBS se sastoji od dva kvadrupola i jednog dipola. Postavljen je bio na  $0^\circ$  prema snopu što zbog kinematike reakcije implicira veliku akceptanciju za teške ione nastale u reakciji i izašle iz mete. Snop je sakupljan u Faradayevoj čaši unutar spektrometra dok su teški ioni iz reakcije skretani prema fokalnoj ravnini.

## Detektor za teške ione

Detektor za teške ione (HI) postavljen je u vakuumsku komoru ispred fokalne ravnine spektrometra. Sastoji se od dva niza od po 30 phoswich detektora koji se nalaze jedan iznad drugog. Pojedini HI detektor je kristal CsI(Tl) dimenzija  $4\text{ cm} \times 1.3\text{ cm} \times 1.3\text{ cm}$  na čijoj se jednoj strani nalazi tanki sloj ( $80\text{ }\mu\text{m}$ ) plastičnog scintilatora. Svjetlosni signal iz scintilatora se očitava pomoću fotomultiplikatora. Kombinacija sporog i brzog scintilatora omogućava analizu oblika signala i identifikaciju iona.

## Elektronika

Signali iz fotomultiplikatora obrađivani su na standardni način korištenjem CAMAC i NIM elektronike. Najprije je signal cijepa u dva od kojih jedan odlazi u diskriminator i koristi se za mjerenje vremena, stvaranje signala vrata u analogno-digitalnom pretvaraču (QDC) i odlučivanje u okidaču. Drugi se dugim kablovima vodi u QDC. Tu se integrira vratima različite duljine što omogućava analizu oblika signala. Signal okidača započinje brojanje u vremensko-digitalnom pretvaraču dok diskriminirani signal iz detektora zaustavlja brojanje.

## Ovisnost o visokom naponu i zasićenje fotomultiplikatorskih cijevi

Prilikom testiranja detektora za teške ione primijećeno je izobličenje signala s porastom visokog napona. Svi su naponi podešeni tako da se izobličenje signala izbjegne.

## Sustav detekcije fotona

Detektor Plastic Ball je već korišten kao fotonski detektor iako je njegova prvobitna namjena bila detekcija teških iona. Pokazalo se da je efikasnost i energijska razlučivost fotona skromna pa je za ovaj eksperiment izrađen aktivni fotonski pretvarač - detektor Inner Shell. PB detektor sastoji se od

552 phoswich modula duljine 34 cm oblika krnje piramide s trokutastom bazom. Svaki modul napravljen je od brzog plastičnog scintilatora na kojem se nalazi tanki sloj sporog kristala  $\text{CaF}_2$  (4 mm). Na suprotnoj strani nalazi se fotomultiplikatorska cijev koja svjetlosni signal iz oba scintilatora pretvara u električni signal. Pojedini modul pokriva prostorni kut od 17 msr, a cijeli detektor pokriva polarne kutove od  $50^\circ$  do  $160^\circ$  i gotovo cijeli azimut.

IS detektor je umetnut unutar PB detektora i pokriva polarne kutove od  $90^\circ$  do  $150^\circ$ . Sastoji se od 64 kristala  $\text{CsI(Tl)}$  koji se očitavaju malim fotomultiplikatorskim cijevima. Kristali su oblika prizme peterostranog i šesterostranog presjeka poslagani tako da tvore polusferu. Detektori zaustavljaju nabijene čestice pa u PB detektoru na stražnjim kutevima dolaze samo fotoni. Razlučivost određivanja kuteva fotona je  $6^\circ$  (FWHM) za prednje, a  $9^\circ$  (FWHM) za stražnje detektore. Efikasnost detekcije fotona s IS detektorom iznosi preko 70% dok je za sam PB detektor oko 45%.

## Elektronika

Slično prije spomenutom detektoru teških iona signali iz fotonskih detektora su obrađeni tako da se cijepaju i jedan signal ide na diskriminator pa se koristi u okidaču i za startanje brojanja u vremensko-digitalno pretvaraču. Drugi signal odlazi linijama za kašnjenje u analogno-digitalni pretvarač. Signali iz PB detektora se još jednom cijepaju da bi se integriranjem vratima različitih duljina omogućila analiza oblika signala i razdvajanje fotona od protona.

## Prikupljanje podataka

Svi detektori su očitavani preko elektroničkih CAMAC modula. Oni su povezani u sustav kojem se upravlja preko VME procesora. Software za prikupljanje podataka je standardni KVI-ov software nadograđen kodom za nove detektore.

## **Okidač**

Nekoliko signala okida početak očitavanja podataka. Najvažniji je signal koji je nastao od signala iz HI i stražnjih PB detektora koji su stigli istovremeno. Prednji detektori nisu zasjenjeni IS detektorom tako da su pod naletom velikog broja iona, najviše protona, te je frekvencija slučajnih istovremenih signala sa signalima iz HI detektora prevelika. Signal iz PB detektora prolazi dužim kablovima jer je nastao ranije od signala u HI detektoru zbog vremena proleta teškog iona.

## **Brojači**

Uz događaje generirane okidačem na disk se otprilike svake sekunde upisuje događaj u kojem se nalaze podaci o ukupnom broju signala koji su stigli iz pojedinog detektora, ukupni naboj, odnosno struja snopa i proteklo vrijeme od zadnjeg takvog upisa. Upisuje se broj signala koji je elektronika zabilježila, broj signala koji je došao za vrijeme "živog vremena" i broj signala koji je prihvaćen od sustava za prikupljanje podataka. Ukupna frekvencija prikupljanja događaja je oko 300 Hz.

# Simulacija reakcije pionske fuzije

Simulacije su neophodne za analizu podataka prikupljenih kompliciranim sustavom detektora. Već u samom planiranju eksperimenta potrebno je znati koje su ograničavajući faktori u slučaju proučavane reakcije (npr. kinematika). Također je potrebno ocijeniti i razumijeti odziv pojedinačnih detektora ovisno o svojstvima čestica koje ulaze u detektor. Neke karakteristike detektora u nedostatku dodatnih mjerenja mogu se dobiti iz simuliranih podataka. Isto tako i ukupni odziv cijelog detektorskog sustava na pojedinu reakciju kao i učinak pojedinih koraka u analizi mogu se bolje upoznati i poboljšati. I konačno, sam fizikalni proces se može uspješnije proučavati jer se često ne mjeri izravno tražena veličina već neka observabla koja ovisi o njoj. Simulacijama se mogu kontrolirati veze između tih veličina.

Za ovaj eksperiment simulacije su napravljene na nekoliko razina. Prva je najobičnija generacija velikog broja događaja koji zadovoljavaju zakone sačuvanja energije i količine gibanja. Time je određena kinematika pojedinog događaja i vidi se raspodjela pojedinih čestica u faznom prostoru.

## Implementacija teorijskih predviđanja

Svakom tom događaju može se korištenjem fizikalnog modela pridružiti statistička težina tako da konačna raspodjela odgovara distribuciji koju predviđa model. Tako se mogu uspoređivati različiti fizikalni modeli s trivijalnom distribucijom po faznom prostoru koja proizlazi samo iz kinematike.

## Akceptancija detektora

Zatim se čestice koje imaju količine gibanja generirane u prvom koraku propuštaju kroz simulaciju detektora (GEANT3). Za svaki pojedinačni detektor dobije se depozicija energije od svake čestice i tu se može proučavati odziv detektora (npr. kolika će biti efikasnost za detekciju pojedinih čestica). U konačnici se svi podaci po detektorima mogu analizirati kao što se analiziraju i realni podaci prikupljeni u eksperimentu.

Na ovaj se način dobiju informacije o tome koja je akceptancija detektora i to se onda koristi u normalizaciji podataka iz mjerenja kako bi se dobili udarni presjeci. Vrlo bitna stvar u ovom eksperimentu je utjecaj debele mete na detekciju nastalih iona u reakciji. Ta korekcija je također dobijena iz ovih simulacija.

## Kinematička rekonstrukcija

Zbog konačne razlučivosti detektora rekonstruirana kinematika pojedinog događaja nije savršena pa je konačna raspodjela iskrivljena u odnosu na pravu. Rezultati ovih simulacija su korišteni da bi se dobila prava raspodjela događaja, a samim time i ispravni diferencijalni udarni presjek.



# Analiza podataka

Reakcija koja se mjeri ima vrlo mali udarni presjek u odnosu na reakcije koje stvaraju pozadinu. Velikim dijelom se već tijekom prikupljanja podataka odbacuje velik dio pozadine tako da se uzimaju samo oni događaji u kojima su HI detektor i PB detektor proizveli signal istovremeno, odnosno točnije rečeno, iz iste reakcije. Budući da je prednji dio PB detektora zapljusnut velikim brojem fragmenata (uglavnom protona) iz nuklearnih reakcija, signali prednjih detektora su izuzeti iz okidača. I uz sve to, prikupljeni podaci većinom sadržavaju nasumične koincidencije signala iz oba detektora. Stoga je analiza neophodna za izbor dobrih događaja.

## Kalibracija

### Detektor teških iona

Detektor teških iona se koristi za detekciju nabijenih čestica emitiranih pod malim kutem u odnosu na snop. Mjere se količina gibanja, energija i vrijeme proleta čestice. Iz analize oblika signala identificiraju se različiti ioni.

### Kalibracija količine gibanja

Elastično raspršeni ioni  $^4\text{He}$ ,  $^{12}\text{C}$ ,  $^{16}\text{O}$ ,  $^{19}\text{F}$  i  $^{20}\text{Ne}$  na teškoj meti  $^{197}\text{Au}$  u uski otvor na nekom kutu raspršenja imaju dobro definiranu energiju i količinu gibanja. Ovisno o magnetskom polju dipola spektrometra ioni će završiti na različitim mjestima u fokalnoj ravnini, odnosno u različitim pojedinim HI detektorima. Iz toga se može odrediti relacija između rigiditeta čestice

i položaja u fokalnoj ravnini. Osim toga, iz širine vrha može se odrediti razlučivost količine gibanja koja je 1.1% FWHM.

### **Kalibracija energije**

U energijskom spektru pojedinog detektora pojavljuju se vrhovi koji odgovaraju različitim ionima. Ti su vrhovi korišteni za relativnu kalibraciju tako da su podešeni na iste vrijednosti. Nestabilnosti tijekom eksperimenta su izgladene podešavanjem kalibracijskih parametara tijekom eksperimenta. Opažena nelinearnost između energije čestice i signala onemogućava određivanje energije čestica iz ovih spektara.

I da je moguće precizno odrediti energiju čestice, to bi kao i u slučaju mjerenja količine gibanja bila energija nakon izlaska iz mete koja se uvelike razlikuje od one u trenutku nastajanja iona zbog gubitka energije u debeloj meti.

### **Ponašanje svjetlosnog signala**

Kalibracija količine gibanja se može iskoristiti za određivanje kinetičke energije s kojom čestica ulazi u detektor i koju deponira u detektoru jer su sve čestice zaustavljene u scintilatoru. Problem je što se u spektrima mjeri veličina svjetlosnog signala koji općenito nije linearan s deponiranom energijom.

Položaj vrhova te njihov pomak prilikom promjene magnetskog polja dipola spektrometra pokazuju nelinearnost. Stoga se informacija iz analogno-digitalnog pretvarača nije koristila za određivanje energije čestica već samo za odvajanje različitih iona.

### **Analiza oblika signala**

Kombinacija phoswich detektora i magnetskog spektrometra je snažno oruđe za identifikaciju iona. Svaka čestica koja upada u određeni detektor u fokalnoj ravnini ima dobro definiranu energiju i stoga dobro definiranu depoziciju energije u pojedinim scintilatorima. Stoga je analizom oblika signala moguće razlikovati različite ione kao različite nakupine signala u 2-dimenzionalnom

dijagramu koji prikazuje iznos dobiven kratkom integracijom signala u odnosu ma iznos dobiven dugom integracijom signala (sl. 5.7).

Identifikacija iona preko analize oblika signala potvrđena je mjerenjem vremena proleta iona.

### **Mjerenje vremena proleta**

U eksperimentu je mjereno vrijeme između signala iz PB detektora i signala iz HI detektora. Većina iona nastalih u meti je korelirano s fotonima koji nastaju u istoj reakciji. Sporiji ioni će imati veće vrijednosti u vremenskom spektru. Vrijeme proleta proporcionalno je omjeru mase i naboja čestice u pojedinom HI detektoru na određenom mjestu u fokalnoj ravnini. Dobro identificirani ioni su iskorišteni za kalibraciju vremena proleta, odnosno omjera mase i naboja. Samim HI detektorom postiže se relativno čist signal  ${}^7\text{Be}$  uz 8% pozadine (sl. 5.12).

### **Detektori fotona**

Detektorima fotona identificiraju se fotoni, određuju im se kutevi emisije iz položaja detektora i energija fotona iz deponirane energije u oba detektora. Istovremena pojava signala u IS i PB detektorima koji se nalaze na bliskim kutevima jedan je od potpisa fotona jer nabijene čestice su u potpunosti zaustavljene u IS kristalu. U PB detektorima na prednjim kutevima analiza oblika signala omogućuje odbacivanje nabijenih čestica.

Primijećeno je, a isto se vidi u simulacijama, da jedan foton može proizvesti prekinuti pljusak čiji signali se javljaju i u udaljenijim detektorima. Stoga se prilikom grupiranja detektora u grozdove uzimaju i daljnji susjedi. Kut emisije fotona se određuje iz prosječnog položaja detektora koji su proizveli signal s tim da veći signal ima veću težinu prilikom određivanja prosječnog položaja.

Energijska kalibracija se napravila u dva koraka. Najprije je napravljena relativna kalibracija svih detektora s podacima iz eksperimenta i iz mjerenja kozmičkih zraka. Za apsolutnu kalibraciju su korištene kozmičke zrake koje prolaze duž jednog detektora ne deponirajući energiju u susjedima.

## Izbor događaja

Dobri događaji koji odgovaraju reakciji koja se proučava moraju sadržavati  ${}^7\text{Be}$  u HI detektoru i dva fotona u fotonskim detektorima. Sve te čestice moraju dolaziti istovremeno iz iste reakcije.

Izvršna identifikacija dobrih događaja potvrđena je korelacijom detekcije iona  ${}^7\text{Be}$  u HI detektoru s detekcijom dva fotona u fotonskim detektorima tako da je kut između njihovih smjerova veći od  $120^\circ$  što odgovara kinematici dva fotona nastala u raspadu sporog neutralnog piona (sl. 5.20).

Primijećeno je da fotoni s malom energijom uglavnom dolaze iz pozadine pa su odbačeni fotoni s manjom energijom od 5 MeV. Time je pozadina svedena na zanemariv broj događaja ( $\sim 1\%$ ) pa se može sa sigurnošću reći da su svi tako odabrani događaji reakcije pionske fuzije.

## Kinematička rekonstrukcija

Za kinematičku rekonstrukciju pionske fuzije dovoljno je odrediti jednu varijablu, npr. kut piona u sustavu centra mase. Za to određivanje koriste se zakoni sačuvanja energije i količine gibanja. U konačnom su stanju tri čestice pa postoji 5 nezavisnih kinematičkih varijabli koje su izmjerene. To su po dva kuta za svaki foton i energija jednog fotona. Uzima se onaj foton koji ima veću deponiranu energiju. Rekonstruirana invarijantna masa dvaju fotona odgovara masi neutralnog piona.

Raspodjela po polarnom kutu piona se treba korigirati budući da je kut dobiven iz varijabli izmjerenih s nekom greškom. Korekcija se određuje iz simulacija usporedbom početnih kuteva piona s onima koji su dobiveni rekonstrukcijom simuliranih podataka (sl. 5.23).

## Izračunavanje udarnog presjeka

Diferencijalni udarni presjek po kutu dobiva se iz korigirane kutne raspodjele tako da se ta raspodjela normira prema ukupnom luminozitetu i korigira za akceptanciju detektora.

## Luminozitet

Luminozitet se određuje iz struje snopa koja se mjeri tijekom cijelog eksperimenta i gustoće mete koja se odredi iz temperature koja se također prati. Stabilnost gustoće se vidi u stabilnom (unutar 8%) omjeru broja signala iz detektora i naboja snopa. Taj se luminozitet korigira za mrtvo vrijeme koje se određuje iz podataka sakupljenih s brojača svake sekunde tijekom eksperimenta.

## Akceptancija

Zbog ograničene geometrije i efikasnosti detektora ne mogu sve reakcije koje se dogode biti detektirane. Osim toga, primjena nekih uvjeta u analizi kako bi se smanjila pozadina, odbacije takodjer i dobre događaje. Sve to je uzeto u obzir u GEANT3 simulacijama iz kojih je određen faktor korekcije u ovisnosti o kinematici reakcije, odnosno kutu piona.

U obzir su uzeti geometrija fotonskih detektora, geometrija otvora spektrometra, odbacivanje fotona s manjom energijom od 5 MeV i gubitak energije iona u meti od tekućeg helija te akceptancija HI detektora ovisna o impulsu čestice (sl. 5.27).

# Rezultati i rasprava

Normiranjem konačne kutne razdiobe na mjereni luminozitet i akceptanciju detektora dobiven je diferencijalni udarni presjek proučavane reakcije (sl. 6.1). Zbog cilindrične simetrije reakcije diferencijalni udarni presjek ovisi samo o kutu emisije piona u odnosu na snop. Prednji polarni kutevi nisu pokriveni zbog geometrije PB detektora i potisnuća događaja zbog apsorpcije iona u meti.

Ograničena kutna raspodjela je ekstrapolirana na cijeli raspon polarnih kuteva prilagodbom na red Legendreovih polinoma različitog stupnja. Za reakcije blizu praga očekuje se da su prisutni samo mali parcijalni valovi.

Najbolja prilagodba po  $\chi^2$  testu dobije se za razvoj do Legendreovog polinoma trećeg stupnja. Razvoj pokazuje da su u konačnom stanju reakcije prisutni parcijalni d-valovi. Iz prilagodbe se može odrediti ukupni udarni presjek koji iznosi  $\sigma_{tot} = (53 \pm 9)$  nb. Ovdje je greška statistička, a dodatne sistemske neodređenosti dolaze od greške luminoziteta (7%), korekcije akceptancije (4%) i preostale pozadine (1%).

Usporedba izmjerenih udarnih presjeka s izračunima raspoloživih modela prikazana je na sl. 6.2. Ukupni udarni presjek dobro se slaže s predviđanjima modela s prijelaznim pobuđenjem  $\Delta$ -rezonancije [61] i modela međudjelujućih grozdova [67]. Kutne raspodjele se malo razlikuju, osobito na stražnjim kutevima. Međutim teorijske razdiobe imaju slični oblik kao i eksperimentalna što znači da sadrže doprinos pionskog parcijalnog d-vala. Poluempirički model [64] ne reproducira dobro ni ukupni udarni presjek, niti oblik raspodjele.

Zanimljivo je primijetiti da prva dva modela daju slične rezultate iako je mehanizam stvaranja piona različit. Naime, u prvom je pion stvoren

isključivo preko  $\Delta$ -rezonancije, a u drugom isključivo nerezonantno.

Ukupni udarni presjek reakcije  ${}^4\text{He}({}^3\text{He},\pi^0){}^7\text{Be}$  uspoređen je s dosadašnjim eksperimentalnim udarnim presjecima za slične reakcije (sl. 6.3). Vidljivo je da udarni presjek naglo pada s porastom broja nukleona u reakciji i to preko nekoliko redova veličine. Nova mjerenja se uklapaju u takav trend. Međutim, postoje velike razlike u udarnom presjeku za različite reakcije s istim brojem nukleona. To dolazi od ovisnosti udarnog presjeka o energiji snopa u reakciji, o nuklearnoj strukturi konačnog stanja i vrsti piona koji je nastao, tj. o izospinu u reakciji. U reakcijama stvarnja piona na višim energijama gdje je dominantni mehanizam stvaranje u individualnim nukleon-nukleon sudarima, udarni presjek raste s produktom broja nukleona u meti i broja nukleona u projektilu, a struktura konačne jezgre je nebitna. U reakciji pionske fuzije moraju sudjelovati svi nukleoni što naglašava utjecaj strukture konačnog stanja, a vjerojatnost koherentne reakcije se smanjuje drastično s povećanjem broja nukleona.

# Zaključci i perspektiva

Izvedena su dva eksperimenta na institutu KVI u Groningenu u Nizozemskoj u kojima se proučavala pionska fuzija. Neutralni pion je stvoren u reakcijama  ${}^4\text{He}({}^3\text{He},\pi^0){}^7\text{Be}$  and  ${}^6\text{Li}({}^4\text{He},\pi^0){}^{10}\text{B}$  [57, 58] pri energijama u sustavu centra mase koje su samo oko 10 MeV iznad praga reakcije.

Takve reakcije su ekstremni primjer nuklearnih reakcija u kojima je gotovo sva raspoloživa energija iskorištena za stvaranje piona. U njima je potreban visok stupanj koherencije svih nukleona. Mehanizam koji bi opisivao ovakvu vrstu reakcije je još nedovoljno poznat. Osim toga, reakcije stvaranja piona blizu praga odlikuju se velikim prijenosom količine gibanja, što je vrlo osjetljivo na komponente nuklearnih valnih funkcija s velikim količinama gibanja. Te komponente su povezane s kratkodosežnim korelacijama između nukleona u jezgri. Nadalje, reakcije blizu praga pogodne su za proučavanje zbog ograničenog faznog prostora i jednostavnije analize konfiguracija u početnom i konačnom stanju.

Eksperimentalni podaci o reakcijama pionske fuzije su rijetki pa su stoga nova mjerenja neophodna za poboljšanje razumijevanja reakcijskog mehanizma kao i nuklearnih valnih funkcija velike količine gibanja.

U eksperimentu opisanom u ovom radu, sve nastale čestice u konačnom stanju detektirane su istovremeno. Za tu je svrhu razvijen, provjeren i primijenjen kompleksan sustav detektora. Neutralni pioni se raspadaju u meti i detektirani su pomoću dvaju fotona nastalih u pionskom raspadu. Detektor Plastic Ball pokriva 70% prostornog kuta s time da svaki od 552 modula pokriva 17 msr. Svaki modul je phoswich detektor i stoga omogućava razlikovanje fotona i nabijenih čestica na temelju analize oblika signala. Uz to, detektor daje brz signal koji se koristi za okidanje skupljanja podataka i određi-



vanje vremena. Zbog loše energijske razlučivosti i efikasnosti u mjerenju fotona, razvijen je novi detektor Inner Shell koji djeluje kao aktivni pretvarač fotona unutar PB detektora. IS detektor pokriva samo stražnju hemisferu što ograničava određivanje energije za samo jedan foton. Nadogradnjom IS detektora na prednje kuteve, uvelike bi se povećale mogućnosti ovog sustava detektora.

Nastala jezgra je detektirana i identificirana sustavom magnetskog spektrometra (Big-Bite Spectrometer) i nizom phoswich detektora postavljenih u fokalnu ravninu spektrometra (Heavy-Ion detector). Ovakav sustav moćno je oruđe u identifikaciji iona naboja  $Z \leq 5$  na temelju analize količine gibanja, oblika signala i mjerenja vremena proleta.

Veliki luminozitet je postignut korištenjem mete od tekućeg helija. Zbog debljine mete velik dio energije nastale jezgre je apsorbiran u meti. Taj je gubitak nadiđen u analizi pomoću simulacija. Plinska meta bi smanjila ovaj gubitak, ali i luminozitet, te otežala određivanje njene debljine.

Približno 500 događaja sa zanemarivom pozadinom (1%) je izdvojeno analizom podataka. Kinematika je određena iz mjerenih kuteva oba fotona i energije jednog od njih. Zbog konačne razlučivosti tih veličina, kinematika je korigirana na temelju podataka dobivenih iz simulacija. Normalizacijom pomoću mjerenog luminoziteta i simulirane akceptancije detektora dobiven je diferencijalni udarni presjek, a njegovom prilagodbom na red Legendreovih polinoma i ukupni udarni presjek.

Eksperimentalni podaci su uspoređeni s teorijskim predviđanjima triju različitih modela. Dva od njih (model s prijelaznim  $\Delta$  međustanjem [61] i model međudjelujućih grozdova [67]) relativno dobro opisuju ukupni udarni presjek i nešto lošije diferencijalni. Međutim, oblik distribucije pokazuje asimetriju između prednjih i stražnjih kuteva te ukazuje da neočekivanu prisutnost pionskog parcijalnog d-vala što je opaženo i u mjerenim podacima. Ova dva modela daju slične rezultate iako su im mehanizmi stvaranja piona različiti. S druge strane, oba koriste grozdastu strukturu u opisivanju konačnog nuklearnog stanja što ukazuje na dominantni utjecaj strukture na reakciju. Da bi se rasčistile nedoumice potreban je konzistentni izračun koji bi sadržavao oba mehanizma stvaranja piona kao i druge koji su u oba modela zanemareni.

Treći model koji poluempirički koristi jednostavniju reakciju [64] ne reproducira dobro mjerene podatke.

Mjereni udarni presjek je također uspoređen s mjerenim udarnim presjecima drugih reakcija pionske fuzije. Rezultat ovog mjerenja konzistentan je s ostalima što se tiče ovisnosti udarnog presjeka o broju nukleona prisutnih u reakciji. Podaci pokazuju i da su varijacije udarnog presjeka za sustave iste veličine velike do jednog reda veličine. To je stoga što udarni presjek ovisi i o raspoloživoj energiji, strukturi nuklearnih stanja i izospinskoj strukturi početnog i konačnog stanja. Bez obzira na to, strmi pad udarnog presjeka s porastom broja nukleona u reakciji je vrlo izražen.

Da bi se razdvojili utjecaji pojedinih gore spomenutih parametara i izvukli precizniji zaključci, potrebna su nova sustavna mjerenja različitih reakcija pionske fuzije. Mnogo parametara utječe na usporedbu udarnih presjeka - energija iznad praga reakcije, struktura niskoležećih stanja i vrsta piona, pa su stoga i sustavna mjerenja, gdje se samo jedan od tih parametara mijenja, neophodna. Također je pokrivenost velikog dijela faznog prostora neophodan uvjet da bi se doprinosi različitih parcijalnih valova razdvojili. Jednom kad je mehanizam reakcije dovoljno poznat, pionska fuzija se može koristiti kao jedinstvena proba za kratkodosežne korelacije nukleona u jezgrama.

# Contents

<b>Extended abstract in Croatian</b>	<b>ix</b>
<b>1 Introduction</b>	<b>1</b>
1.1 Nuclear physics and pion . . . . .	1
1.2 Pion production in nuclear reactions . . . . .	4
1.3 Pionic fusion . . . . .	10
1.4 Outline of this work . . . . .	14
<b>2 Theoretical background</b>	<b>15</b>
2.1 Kinematics and selection rules of the reaction . . . . .	15
2.2 Cross section formalism . . . . .	21
2.3 Pion-nucleon interaction . . . . .	22
2.4 Models for pionic fusion . . . . .	24
2.4.1 Intermediate $\Delta$ resonance excitation . . . . .	25
2.4.2 Semi-empirical model . . . . .	28
2.4.3 Interaction cluster model . . . . .	30
<b>3 Experimental setup</b>	<b>34</b>
3.1 The liquid helium target . . . . .	37
3.2 The Big-Bite Spectrometer . . . . .	39
3.3 The Heavy-Ion detector . . . . .	41
3.3.1 Readout electronics . . . . .	43
3.3.2 High-voltage dependence and tube saturation . . . . .	46
3.4 Photon detection system . . . . .	46
3.4.1 Plastic Ball and Inner Shell electronics . . . . .	52

## CONTENTS

3.5	The data acquisition . . . . .	53
3.5.1	The trigger . . . . .	54
3.5.2	The scalers . . . . .	55
<b>4</b>	<b>Simulation of the pionic-fusion reaction</b>	<b>58</b>
4.1	Implementation of the theoretical predictions . . . . .	64
4.2	Detector acceptance . . . . .	66
4.3	Kinematical reconstruction . . . . .	67
<b>5</b>	<b>Data analysis</b>	<b>69</b>
5.1	Calibration . . . . .	69
5.1.1	Heavy-Ion detector . . . . .	69
5.1.2	Photon detectors . . . . .	84
5.2	Event selection . . . . .	90
5.3	Kinematical reconstruction . . . . .	93
5.4	Cross section evaluation . . . . .	98
5.4.1	Luminosity . . . . .	99
5.4.2	The acceptance . . . . .	101
<b>6</b>	<b>Results and discussion</b>	<b>106</b>
<b>7</b>	<b>Conclusions and outlook</b>	<b>113</b>
	<b>Bibliography</b>	<b>117</b>
	<b>Curriculum vitae</b>	<b>i</b>
	<b>List of CC publications</b>	<b>ii</b>

# Chapter 1

## Introduction

### 1.1 Nuclear physics and pion

The atomic nucleus has been intensively studied for a century. Although an enormous knowledge has been achieved, many phenomena are still not fully understood and research is going on. One of the basic questions is how to describe a complex nucleus or nuclear reaction from its constituents and their interactions. Another one is the relation of these phenomena to even more fundamental particles and interactions.

The current state of the modern theory of nuclear force is reviewed in [1]. The nuclei are built of nucleons which are particles with a substructure. The interaction between them is actually caused by the interaction of the elementary quarks which interact via gluon exchange but is treated as an effective interaction mediated by pion exchange. Their behavior is well described by the Quantum chromodynamics (QCD) at high energies due to a property called asymptotic freedom. The strong force coupling constant becomes small at high energies or, equivalently, at small distances and therefore a description of quark dynamics can be perturbative.

In the opposite limit, i.e. at long distances or at low energies characteristic for nuclear phenomena the QCD becomes non-perturbative and a different approach is needed. A feature that characterizes this regime is the quark confinement which means that quarks have never been observed in isolation

## CHAPTER 1. INTRODUCTION

but in composite particles called hadrons where they exist in groups of three (baryons) or of quark-antiquark pairs (mesons). The baryons and mesons are the relevant degrees of freedom for the nuclear phenomena at low and intermediate energies (up to 1 GeV). This is the basis of the phenomenological models which have been very successful in nuclear physics.

On the other hand, a huge effort is invested to derive hadronic properties from the fundamental QCD Lagrangian on a discretized space-time lattice. This concept is known as the Lattice QCD and requires high computer power. Presently, masses of ground state baryons [2] can be calculated with good precision but dynamical information can not be provided.

The Chiral perturbation theory (ChPT) is another approach in describing the nuclear forces which have been rapidly developed for the last decades. It is based on the spontaneously broken chiral symmetry of the QCD Lagrangian in the regime of low-energy nuclear physics. The effective Lagrangian is expanded in some small parameter (small momentum transfer) respecting all symmetries of the fundamental one. The controlled expansion allows for uncertainty estimates.

In general, any operational consideration to the low- or intermediate-energy nuclear or hadron physics supposes that nucleons and mesons are elementary particles. Usually this is enough to account for the observable phenomena. Their structure might come into play via baryonic resonances or by inclusion of three-body forces.

Inspired by the success of quantum electrodynamics (QED) in 1935 Yukawa [3] proposed an exchange force between nucleons in analogy with the photon exchange between charged particles, but with a particle of non-vanishing mass in order to describe the short-range behavior of the force. A few years later in 1947, the pion was discovered in cosmic rays [4]. The first artificial charged pions were produced and detected in  $\alpha+^{12}\text{C}$  reactions [5]. The first neutral pion was produced in 1950 [6].

Since Yukawa's idea the models for the low-energy nucleon-nucleon interaction have become more and more sophisticated but in all of them the pion exchange remained the basic mechanism for the medium- and the long-range ( $r \geq 1$  fm) part of the force. Moreover, within the ChPT the pions are

## CHAPTER 1. INTRODUCTION

recognized as Goldstone bosons of the broken chiral symmetry.

The pion consists of the lightest up and down quarks and antiquarks. It is a pseudoscalar meson with spin  $S=0$  and negative parity and an isovector particle (with isospin  $I=1$ ) so it can have three isospin projections which correspond to neutral pion  $\pi^0$  and charged pions  $\pi^+$  and  $\pi^-$ . This makes the pion a suitable probe for studying the isospin phenomena (charge symmetry and charge independence tests [7, 8], populating specific nuclear states [9]). The neutral and charged pions differ in their masses (134.98 MeV<sup>1</sup> and 139.57 MeV, respectively) and decays. The neutral pion decays electromagnetically into two photons with branching ratio of 98.8 % and decay time of  $8.4 \cdot 10^{-17}$  s and charged pions decay by weak force into muons and neutrinos with decay time of  $2.6 \cdot 10^{-8}$  s. Consequently the detection techniques must be different. The charged pions are detected like all charged particles by magnetic spectrometers or ionization detectors. The first method gives a good energy resolution but the covered solid angle is small. Also the pion decay imposes a limit on the flight path. The other method covers large solid angle but the energy resolution is reduced. The neutral pions are detected via the photons from the decay that happens still in the target. A huge background of photons originating from the nuclear de-excitations is present, so the two photons are detected in coincidence. The resolution of the  $\pi^0$  energy is influenced by the photon energy resolution and by their angular resolution. Due to the two-photon decay, the detection of a neutral pion with vanishing momentum is possible. In a two-body reaction like pionic fusion the pion energy and angle are related, which can be used for the event selection and kinematical reconstruction. Apart from that in the exclusive pionic-fusion reactions, the detection of the fused nucleus is possible by the recoil in a spectrometer or by the chemical separation of the radionuclide.

---

<sup>1</sup>The natural units ( $c = \hbar = 1$ ) are used in this thesis.

## 1.2 Pion production in nuclear reactions

The pions are present in nuclei at low energies as virtual mediators of the force between nucleons. To learn more about this force a study of the reactions with real pions is necessary [10, 11]. These include elastic and inelastic scattering, production, and absorption. The pions are light compared to the typical hadronic mass (1 GeV) and can be created easily. Therefore, they are unavoidable in all nuclear reactions at intermediate energies.

The most simple pion production reactions involve two nucleons and they serve as a basic building block for more complex systems. The energy and momentum conservation laws forbid the pion production on a single nucleon. In a nucleon-nucleon collision a real pion can be produced if the available center-of-mass energy exceeds the pion mass. The laboratory energy threshold is about 280 MeV (290 MeV) for a neutral (charged) pion and depends on the small mass differences between different nucleons and a small  $Q$ -value if a bound deuteron is produced. At the kinetic energy of 1 GeV this inelastic process amounts a half of the total NN reaction cross section. Therefore, a proper description of the nucleon-nucleon interaction should include inelastic processes. An interesting feature of the pion production reactions is a huge momentum transfer. This implies that such reactions can give an insight to the short-range phenomena between the nucleons where they can overlap. One expects that here even the quark substructure comes into play.

The studies of the reactions very close to the threshold are very helpful since their final states are limited to the lowest partial waves and one can experimentally and theoretically get a cleaner picture of the interaction process. From the viewpoint of theory, this may make calculations somewhat less involved because of the restricted angular momentum space and the fact that higher order interactions involving additional pions in the process will not contribute. Experimentally, the small relative energy between the outgoing particles results in a final state where they remain confined in a narrow forward cone because of conservation of the beam momentum. This small solid angle can usually be covered with smaller detectors. A disadvantage for the measurement of such reactions are small cross sections.



## CHAPTER 1. INTRODUCTION

The pion production in nucleon-nucleon collisions has been studied both experimentally and theoretically (see recent reviews [12–14]). The elementary pion production process comprise several  $NN \rightarrow NN\pi$  reactions ( $pp \rightarrow pp\pi^0$ ,  $pp \rightarrow pn\pi^+$ ,  $pp \rightarrow d\pi^+$ ) which are related by the isospin symmetry. In the 1980s existing measured cross sections were parameterized [15] up to the energy of 1.5 GeV for all independent isospin channels. These cross sections were well described by the theory [10]. A dominant contribution to the interaction comes from the intermediate  $\Delta$ -resonance, the lowest baryon excited state with spin  $S = \frac{3}{2}$  and isospin  $I = \frac{3}{2}$ . The mass and the width of the  $\Delta$ -resonance are 1232 MeV and 120 MeV, respectively. At the energies near threshold, the  $\Delta$  channel is suppressed and  $\pi NN$  p-wave pseudovector coupling and re-scattering s-wave mechanisms come up [16]. Also, the initial- and final-state interactions (ISI and FSI) between nucleons have to be taken into account.

Since 1990 very precise measurements of the reactions  $NN \rightarrow NN\pi$  have been performed at energies very close to the pion production threshold and they showed large discrepancies with the available models at threshold [17–21]. This initiated extensive theoretical work in which new ingredients to the interaction have been introduced (heavy-meson exchange, off-shell contributions). The most advanced Jülich model [22] is able to reproduce the total cross sections, but still cannot account for the angular distributions and the polarization observables from the most recent experiments [23–25].

Besides the "phenomenological" or meson-exchange models, much more theoretical work has been carried out within the chiral perturbation theory [1, 14, 26]. The huge momentum transfer was a challenge since the original chiral perturbation approach is based on expansion in small momenta. In spite of a large progress in the field, in more complex reactions between nuclei the most dominant production mechanisms from the older models are used.

A knowledge of the pion production in nucleon-nucleon interactions is needed for the understanding of the pion production or absorption in more complex nuclear reactions. But even the introduction of only one additional nucleon like in the  $pd \rightarrow \pi X$  reactions makes a study much more challenging [28]. Apart from the elementary production mechanism there is another element for a description of the pion production in nucleus-nucleus reactions

## CHAPTER 1. INTRODUCTION

- the many-body dynamics of the whole system [30–32]. Therefore, the study of the pion production in nucleus-nucleus collisions provides an insight not only into the elementary process but also in the course of the reaction and properties of the nuclear matter.

Since the elementary process of pion production is not well known, the use of the pion as a probe for the properties of nuclear reactions is much more involved compared to e.g. the electromagnetic photon or dilepton probes. Moreover, the pions interact strongly with surrounding nuclear matter which distorts the original information in the moment of pion production. To deal with this problem the microscopic transport models have been developed [31]. They follow the motion of interacting nucleons within the phase space. At lower energies the pion production has a small probability and it does not disturb much the nucleon motion and thus it is treated perturbatively. When it becomes considerable, one has to deal with pions equally as with nucleons. In nucleus-nucleus collisions at energies  $\geq 100A$  MeV pions are unavoidable in the description of the reaction dynamics. This is related to the increased excitation of  $\Delta$ -resonances in the reaction zone which decay to a pion and a nucleon.

In general a pion production reaction looks like

$$A_1 + A_2 \rightarrow \pi + X, \quad (1.1)$$

where  $A_1$  and  $A_2$  are the projectile and the target nuclei, respectively, and  $X$  represents all the (unobserved) products of the reaction apart from the pion. A sketch of the expected pion energy spectrum is shown in the upper part of Fig. 1.1. The lower energy region corresponds to the inclusive part where the available energy is shared among many reaction products and the cross section is continuous and dominated by the available phase space. The final state of this part of the spectrum is schematically shown in the lower left part of the figure. The final state shown in lower right part of the figure is associated to the high-energy discrete part of the spectrum with only two bodies - the pion and the nucleus in its ground or excited state.

In nuclear collisions at the energy per nucleon above the free nucleon-

CHAPTER 1. INTRODUCTION

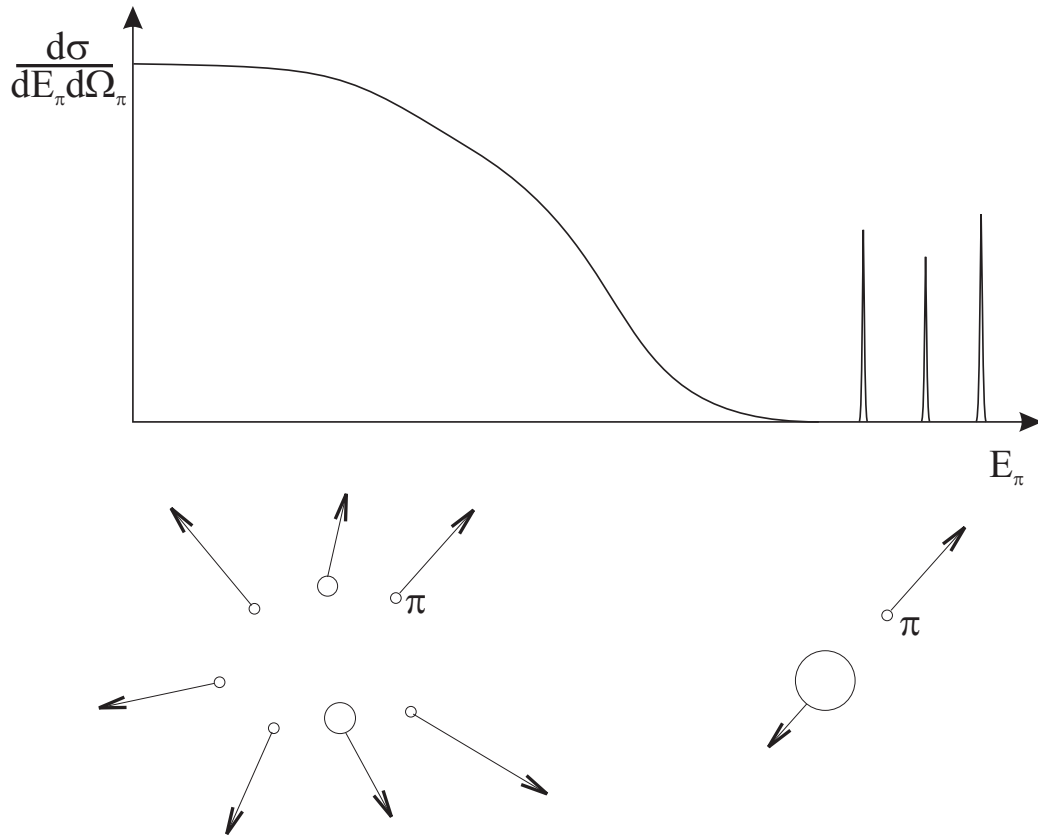


Figure 1.1: Sketch of the expected energy spectrum of a pion produced in nuclear reactions. Note the two different regions, discrete and continuous. The final states of these different regions are schematically shown below.

nucleon pion production threshold, the pions are produced in individual nucleon-nucleon collisions where the dominant mechanism is the  $\Delta$ -resonance excitation (e.g. [33]). Since the produced pions move in the nuclear medium they strongly interact with nucleons and can re-scatter or be reabsorbed. Such phenomena are examined since they can offer the information about the nuclear equation of state, time evolution of the reaction, in-medium properties of mesons and baryons and their interactions.

It was recognized already in the first days of the pion physics that pions can be produced at beam energy per nucleon lower than the free nucleon-nucleon threshold energy [29]. The so-called subthreshold pion production

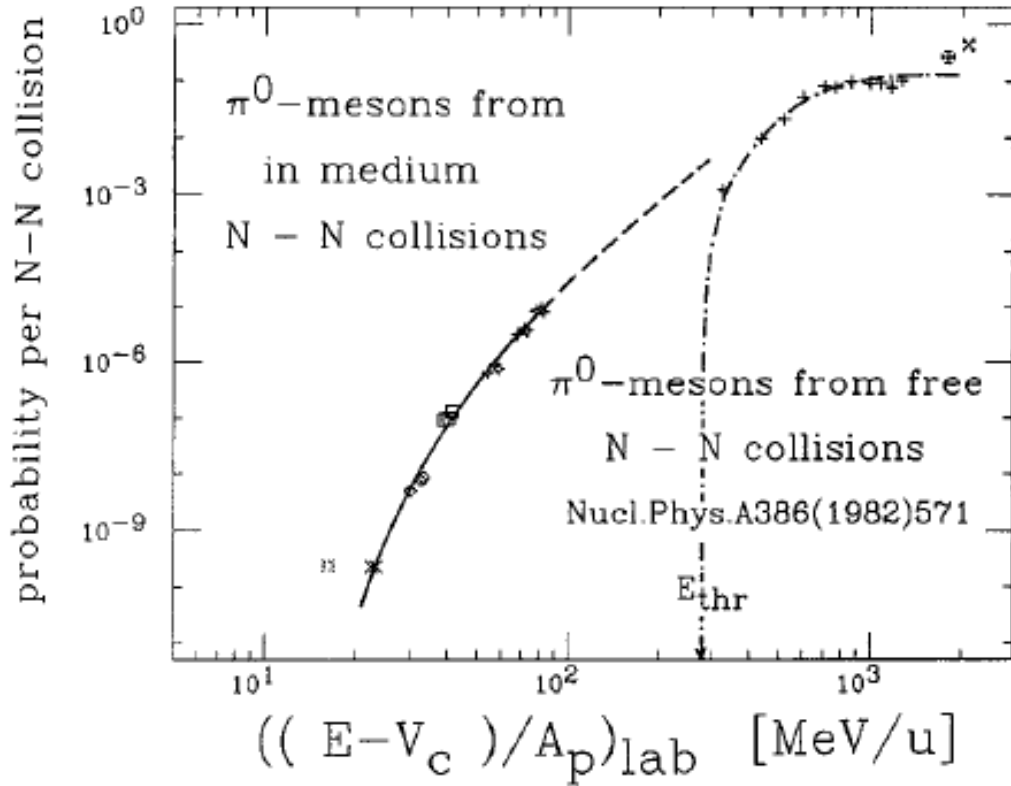


Figure 1.2: Subthreshold pion production probability per participant nucleon pair. Taken from [31].

occurs due to the coupling of the relative motion of the projectile and target nucleons to the Fermi motion within the nuclei. The first machine-made pions were produced at subthreshold laboratory energy of  $95A \text{ MeV}^2$  in  ${}^4\text{He} + {}^{12}\text{C}$  reactions [5].

The experiments show that the pion production probability at the subthreshold energies is the same as a function of the beam energy per nucleon for different projectile-target systems. In Fig. 1.2 the pion multiplicity normalized to the number of participant nucleons in the reactions (see [31] and the references therein). The threshold beam energies per nucleon can drop significantly when the projectile and the target mass number increase as

<sup>2</sup>The beam energy is sometimes also expressed in MeV per nucleon ( $\frac{\text{MeV}}{\text{nucleon}}$ ) or in MeV per atomic mass unit ( $\frac{\text{MeV}}{\text{u}}$ ).

CHAPTER 1. INTRODUCTION

shown in Fig. 1.3. The threshold energies for different projectiles are shown as functions of the target mass number.

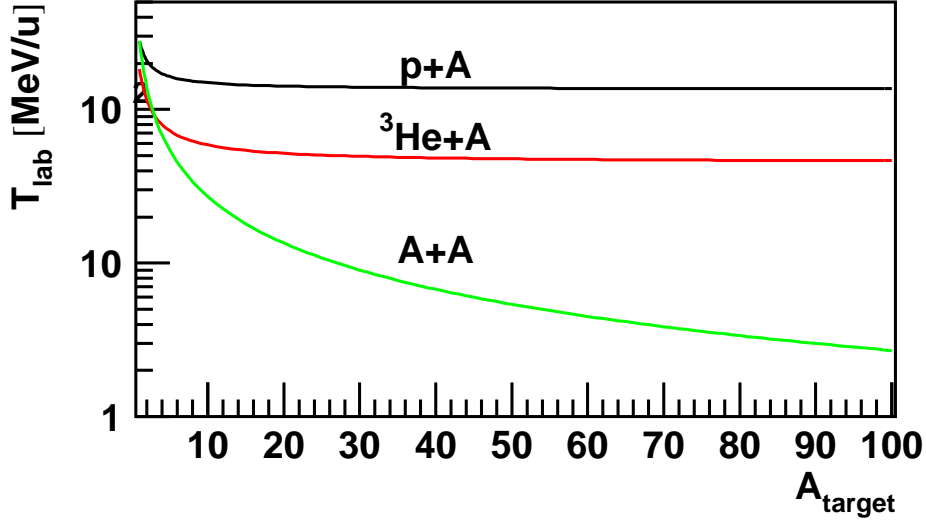


Figure 1.3: The beam energy per nucleon of the absolute pion-production threshold for different projectile-target systems as function of the target mass number.

A detailed calculation of the subthreshold production [34] which takes the Fermi motion and the Pauli blocking into account, underestimates the experimental data severely at the lower beam energies and even sets a cut-off value at  $50A$  MeV. Since the pion production at energies  $25A$  MeV were observed [30], more collective mechanisms had to be introduced to explain the data. The collective mechanisms are the ones in which several nucleons interact coherently transferring all their energy to the pion. For example, several nucleons in the projectile and several in the target can form clusters which interact as two objects and are able to produce a pion since their total energy is sufficient [35].

### 1.3 Pionic fusion

The pionic fusion is an extreme case of the subthreshold pion production where all nucleons have to participate in the reaction. Otherwise there would not be sufficient energy. It can be presented as

$$A_1 + A_2 \rightarrow \pi + B(J, I), \quad (1.2)$$

where  $A_1$  and  $A_2$  are the projectile and the target nuclei and  $B(J, I)$  is the fused nucleus in a specific state of spin  $J$  and isospin  $I$ .

The most simple pionic fusion reaction is the already mentioned reaction  $NN \rightarrow d\pi$ . It is studied as one of the channels in the elementary pion production and can be used as a prototype or a basic element for heavier systems. The reactions with proton beams on a nucleus  $A(p, \pi)A+1$  are the pionic fusion reactions where more than two nucleons contribute. The first pions produced in such exclusive reactions were observed in the beginning of 1970s [36]. Because of their apparent simplicity and a large-momentum transfer they were considered as promising probes for the high-momentum wave functions. However, the basic mechanism turned out to be more complex [37, 38] and, although much experimental and theoretical effort has been invested, a consistent picture is still lacking.

The pionic fusion reactions with complex beams are expected to give further guidelines in understanding the pion production mechanism and the nuclear many-body structure. These reactions are doubly coherent since the energy of the relative motion of the projectile and the target transforms into the pion mass and all involved nucleons form a single bound state. This makes the process very rare comparing to the other reactions at such excitations. Namely, at these beam energies the available energy is usually shared between many nucleons, the highly excited nuclear state is formed and breaks up by emission of nucleons and fragments. Avoiding such a thermalization process and forming a cold nucleus in a low-energy state is highly unlikely.

The pionic fusion data are very scarce comparing to the inclusive pion production or the  $(p, \pi)$  reaction measurements. A historical overview with

## CHAPTER 1. INTRODUCTION

the characteristics of the measured reactions is shown in Table 1.1. The first attempt to detect the pionic fusion reaction with a beam heavier than proton was performed by Eggermann [39]. They irradiated a  $^{181}\text{Ta}$  foil with 173 MeV  $^4\text{He}$  and from the observed energy levels of radiochemically separated  $^{185}\text{Os}$  found the upper limit of the total cross section at 100 nb. The same experimental method was applied later in [40] for the reaction  $^{208}\text{Pb}(^3\text{He},\pi^-)^{211}\text{Ac}$  for the beam energies 158-270 MeV and the total cross section of 1-10 nb was measured. The measured cross section decreases with the increase of the beam energy.

The pions produced in an exclusive reaction were directly observed at CERN in an experiment with the 910 MeV  $^3\text{He}$  beam on a  $^6\text{Li}$  target [41]. The beam energy was well above the absolute threshold, the negative-pion energy spectrum was dominated by the continuous part and the discrete states at the kinematical limit were not clearly separated. The differential cross section for the pion production at  $0^\circ$  integrated over 25 MeV was approximately 10 pb/sr. The same group repeated the experiment with improved precision and with two targets  $^6\text{Li}$  and  $^7\text{Li}$  [42]. The differential cross section at  $0^\circ$  for the discrete final states is measured to be of the order of pb/sr. They also measured deuteron-induced exclusive pion production on  $^6\text{Li}$ ,  $^9\text{Be}$  and  $^{10}\text{B}$  targets with the beam energies of 300 and 600 MeV at Saclay [43]. The measured cross section at  $15^\circ$  for the ground and the first two excited states of  $^8\text{B}$  were of the order of 100 pb/sr to 1.3 nb/sr. For other two targets the discrete nuclear states were not resolved. The data also show the smaller cross section for the higher beam energy.

A series of experiments has been conducted at Orsay and Saclay with  $^3\text{He}$  beams and various targets at energies near the absolute pion production threshold. The pions were detected by using a magnetic spectrometer. Here, the first discrete states with a  $^3\text{He}$  beam at the energies of 268.5 and 280 MeV are observed [44] in the reaction  $^3\text{He}(^3\text{He},\pi^+)^6\text{Li}$  with the cross sections of the order of tens of nb/sr. The cross section of the same reaction but at higher energies between 350 and 600 MeV was measured later [45] and a drop of an order of magnitude was found over this energy range. Furthermore, the  $(^3\text{He},\pi^+)$  reactions with  $^4\text{He}$ ,  $^6\text{Li}$  and  $^{10}\text{B}$  targets and  $^3\text{He}$  energies between

CHAPTER 1. INTRODUCTION

Table 1.1: The results of the measurements of the pionic-fusion reactions performed until now.

Reaction	Ref.	T <sub>beam</sub> [MeV/u]	T <sub>c.m.</sub> [MeV]	Experimental method
$^{181}\text{Ta}(\alpha, \pi^-)^{185}\text{Os}$	[39]	43	27	radiochemical separation
$^{208}\text{Pb}({}^3\text{He}, \pi^-)^{211}\text{At}$	[40]	53-90	21-132	
${}^6\text{Li}({}^3\text{He}, \pi^-)^9\text{C}$	[41]	303	447	magnetic spectrometer
${}^6\text{Li}({}^3\text{He}, \pi^-)^9\text{C}$	[42]	303	447	
${}^7\text{Li}({}^3\text{He}, \pi^-)^{10}\text{C}$		303	491	
${}^6\text{Li}(\text{d}, \pi^-)^8\text{B}$	[43]	150, 300	87, 302	
${}^9\text{Be}(\text{d}, \pi^-)^{11}\text{C}$			117, 354	
${}^{10}\text{B}(\text{d}, \pi^-)^{12}\text{N}$			116, 357	
${}^3\text{He}({}^3\text{He}, \pi^+)^6\text{Li}$	[44]	89.5, 94	8.3, 14.9	
${}^3\text{He}({}^3\text{He}, \pi^+)^6\text{Li}$	[45]	117, 140, 167, 200	48, 82, 120, 168	
${}^4\text{He}({}^3\text{He}, \pi^+)^7\text{Li}$	[46]	88.8, 93.5	12.6, 20.4	
${}^6\text{Li}({}^3\text{He}, \pi^+)^9\text{Be}$	[47]	78, 87, 90, 94	33, 49, 56, 64	
${}^{10}\text{B}({}^3\text{He}, \pi^+)^{13}\text{C}$			63, 82, 90, 99	
${}^7\text{Li}({}^3\text{He}, \pi^+)^{10}\text{Be}$	[48]	78	40	
${}^7\text{Li}({}^3\text{He}, \pi^-)^{10}\text{C}$			38	
${}^{12}\text{C}({}^3\text{He}, \pi^+)^{15}\text{N}$			61	
${}^{12}\text{C}({}^3\text{He}, \pi^-)^{15}\text{F}$			46	
${}^{12}\text{C}({}^3\text{He}, \pi^+)^{15}\text{N}$	[49]	60.5	18.9	recoil
${}^{12}\text{C}({}^3\text{He}, \pi^+)^{15}\text{N}$	[50]	56.7, 78.8	10.0, 62.3	
${}^{12}\text{C}({}^{12}\text{C}, {}^{24}\text{Mg})\pi^0$	[51]	22.85	15.6	
${}^{12}\text{C}({}^{12}\text{C}, {}^{24}\text{Na})\pi^+$			5.0	
$\text{d}(\alpha, {}^6\text{Li}^*)\pi^0$	[52, 53]	104.49, 105.07	1.2, 1.9	
$\alpha(\text{d}, {}^6\text{He})\pi^+$	[9, 54, 55]	108.59, 109.3, 112.25	0.6, 1.2, 5.0	
${}^3\text{He}({}^3\text{He}, {}^6\text{Li}^*)\pi^+$	[56]	87	1.1	

235 and 282 have been studied [46, 47]. The cross section for the two heavier targets dropped approximately by a factor of one thousand. The comparisons between  $\pi^+$  and  $\pi^-$  production with the  ${}^3\text{He}$  beam at 235 MeV were made on  ${}^7\text{Li}$  and  ${}^{12}\text{C}$  [48]. The  $\pi^-$  production cross section is found to be smaller by an order of magnitude relative to that for  $\pi^+$  production.

Instead of a detection of charged pions in magnetic spectrometers, the pionic fusion reaction can be studied by detecting the recoil nucleus. Due



## CHAPTER 1. INTRODUCTION

to the two-body kinematics of the exclusive reaction, such a method allows full kinematical reconstruction based on the kinematical variables of the nucleus. Moreover, the heavy nucleus is emitted into a narrow forward cone in the laboratory system so that a large part of the phase space of the reaction can be covered with a magnetic spectrometer placed at forward polar angles. The detection of the ion requires thin targets and as little as possible material (e.g. windows) between the target and the detector. The first measurement of the recoil nucleus has been done at IUCF in the reaction  ${}^3\text{He}({}^{12}\text{C},\pi^+){}^{15}\text{N}$  at the beam energy of 181.4 MeV [49] and it was followed by the measurements at the beam energies of 170.2 and 236.3 MeV. The measured angle-integrated cross sections summed over the bound states of  ${}^{15}\text{N}$  are  $1.3\pm 0.3$  nb and  $0.8\pm 0.2$  nb for the beam energy of 181.4 and 236.3 MeV, respectively. At the energy of 170.2 MeV, very close to the threshold, drops below 0.03 nb. The first pionic fusion reactions of two heavy ions  ${}^{12}\text{C}({}^{12}\text{C},{}^{24}\text{Mg})\pi^0$  and  ${}^{12}\text{C}({}^{12}\text{C},{}^{24}\text{Na})\pi^+$  at the beam energy of 274.2 MeV have been reported in [51]. For these two reactions cross sections of  $208\pm 38$  pb and  $182\pm 84$  pb, respectively, have been measured.

The recent measurements at Uppsala used the pionic fusion reactions  $d(\alpha,{}^6\text{Li}^*)\pi^0$ ,  $\alpha(d,{}^6\text{He})\pi^+$  and  ${}^3\text{He}({}^3\text{He},{}^6\text{Li}^*)\pi^+$  as probes for the structure of the ground state of the halo nucleus  ${}^6\text{He}$  and its isobar analog excited halo state of  ${}^6\text{Li}$  [9, 52–56]. In measurements at the center-of-mass energy of a few MeV above the threshold reaction cross sections of several tens of nb for  ${}^6\text{Li}^*$  and about 200 nb for  ${}^6\text{He}$  in the final state have been obtained.

The experiment described in this thesis uses the combined approach of the nuclear recoil and the neutral pion detection. Such a method allows almost background-free selection of the pionic fusion events as well as their kinematical reconstruction in a large part of the reaction phase space. With the same setup the reaction  ${}^6\text{Li}({}^4\text{He},\pi^0){}^{10}\text{B}^*$  has been studied at the beam energy of 236 MeV [57, 58]. The angular distribution and the total cross section of  $6.8\pm 0.7$  nb have been measured.

Very few theoretical models have been developed to reproduce some of the measured data. They use different approaches like the  $\Delta$ -isobar excitation [59–62], the semi-empirical use of a simpler reaction [63–66] and the

## CHAPTER 1. INTRODUCTION

interacting cluster model [67]. The theoretical approaches will be presented in Ch. 2.

### 1.4 Outline of this work

The main goal of this thesis is the acquisition and the analysis of the experimental data of the pionic fusion reaction  ${}^4\text{He}({}^3\text{He},\pi^0){}^7\text{Be}$ . Such a task is divided in a few steps. First, the general properties of the reaction from the theoretical point of view have to be learnt. The theoretical background will be presented in the next chapter. That includes a discussion of kinematics and selection rules of the reaction, which emphasizes some interesting properties of the pionic fusion reaction and is necessary in the analysis of the experimental data. The available models of pionic fusion will be outlined.

The experimental setup and methods are described in the third chapter. A special emphasis is put on the newly installed detectors as well as the data acquisition encompassing all detectors.

In the fourth chapter the simulations are introduced. They are necessary for the understanding of the experiment and the analysis of the data. The analysis itself will be presented in detail in the fifth chapter. The results are discussed and conclusion are drawn in the sixth chapter.

## Chapter 2

# Theoretical background

In this chapter some general aspects of the pionic fusion reactions will be outlined. The basics of the elementary processes will be briefly mentioned. Pionic-fusion models that describe the  ${}^4\text{He}({}^3\text{He},\pi^0){}^7\text{Be}$  reaction will be explained in more detail. Since there are only a few theoretical predictions for the pionic fusion process, a simple scaling will be used to compare different models with experimental data.

### 2.1 Kinematics and selection rules of the reaction

The energy and momentum conservation laws impose constraints on the kinematical variables of the reaction. These constraints need to be considered in the design of an experiment as well as in the analysis of experimental data. As it was mentioned in Ch. 1 a pion cannot be produced by a single free nucleon. Simply, the energy needed for pion production is equal to  $m_\pi$ , the mass of the pion, and it must be supplied by the kinetic energy of the nucleon. But then the final momentum cannot be equal to the initial one. At least two nucleons are needed for momentum and energy sharing.

The total energy in the center-of-mass system of two nucleons is

$$E_{tot}^{c.m.} = \sqrt{(E_1 + E_2)^2 - (\mathbf{p}_1 + \mathbf{p}_2)^2}, \quad (2.1)$$

## CHAPTER 2. THEORETICAL BACKGROUND

where  $E_1$  and  $E_2$  are the energies of the projectile and the target, respectively, and  $\mathbf{p}_1$  and  $\mathbf{p}_2 = 0$  are their momenta. In the laboratory system they are

$$E_1 = m_N + T_{beam} \quad (2.2)$$

$$E_2 = m_N \quad (2.3)$$

$$\mathbf{p}_1 = \mathbf{p}_{beam} \quad (2.4)$$

$$\mathbf{p}_2 = 0 \quad (2.5)$$

where  $m_N$  is the nucleon rest mass and  $T_{beam}$  and  $\mathbf{p}_{beam}$  are the kinetic energy and the momentum of the beam.

This gives the total center-of-mass energy expressed in the laboratory kinematical variables

$$E_{tot}^{c.m.} = \sqrt{2m_N^2 + 2m_N(T_{beam} + m_N)}. \quad (2.6)$$

At the production threshold the total energy in the center-of-mass system must be equal to the sum of the rest masses of the final products so that the threshold condition is

$$T_{beam}^{thr} = \frac{(2m_N + m_\pi)^2 - 2m_N^2}{2m_N} - m_N. \quad (2.7)$$

Each nucleon can be either a proton or a neutron and in the final state either a deuteron or two unbound nucleons can emerge. Moreover, the produced pion can be either neutral or charged. With the appropriate masses, the threshold beam energy varies and is approximately equal to 280 MeV (290 MeV) for a neutral (charged) pion.

Additional constraints on the kinematics come from the conservation of total angular momentum and total isospin. The nucleons are particles with a spin  $\frac{1}{2}$  and an isospin  $\frac{1}{2}$  and they are in an initial state of relative motion described by angular momentum  $L_i$ . The total spin of two nucleons can be either 0 (singlet state) or 1 (triplet state) and couples to the angular momentum of the relative motion into the total angular momentum that must

CHAPTER 2. THEORETICAL BACKGROUND

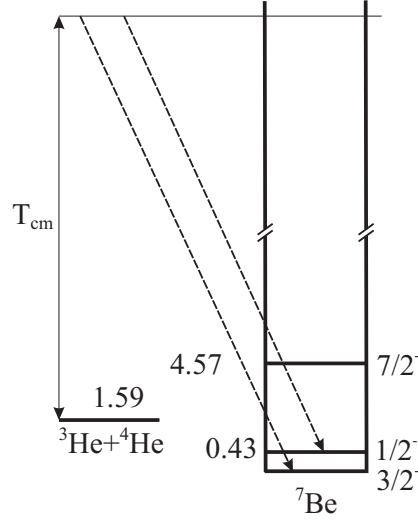


Figure 2.1: Energy level diagram for the pionic fusion reaction  ${}^4\text{He}({}^3\text{He}, \pi^0){}^7\text{Be}$ .

be conserved in the reaction. In the final state there are three particles. The two-nucleon wave function is described by a singlet or triplet wave function coupled to the wave function of the relative motion of a certain angular momentum  $L_f$ . The orbital angular momentum of the pion motion relative to the two-nucleon system is specified by the angular momentum  $l_\pi$  and this couples with the total two-nucleon angular momentum to the total angular momentum of the final state. Close to the threshold the final pion momentum is small and this together with the short-range interaction limits the pion angular momenta to the lowest values.

An analogous scheme applies to the isospin. The nucleons in the initial and the final state are either in isospin singlet or isospin triplet state. In the final state their isospin couples to the pion isospin  $I=1$  to form the total isospin which has to be conserved in the reaction. Apart from the rotational and the isospin symmetry, the reactions must respect the parity symmetry. The internal parity of the pion is negative whereas the parity of the state of the relative motion depends on the angular momentum and equals  $(-1)^L$ .

All these rules must be applied to the more complex reactions. The energy level diagram of the pionic fusion reaction under consideration in this

## CHAPTER 2. THEORETICAL BACKGROUND

thesis is shown in Fig. 2.1 The total energy in the center-of-mass system of the projectile nucleus  $A_1$  with the beam kinetic energy  $T_{beam}$  and the target nucleus  $A_2$  at rest in the laboratory system is

$$E_{tot}^{c.m.} = \sqrt{m_{A_1}^2 + m_{A_2}^2 + 2m_{A_2}(T_{beam} + m_{A_1})}. \quad (2.8)$$

To produce a pion along with the nucleus  $B(J,I)$ , the minimal beam energy is equal to

$$T_{beam}^{thr} = \frac{(m_B + m_\pi)^2 - m_{A_1}^2 - m_{A_2}^2}{2m_{A_2}} - m_{A_1}. \quad (2.9)$$

If one neglects the Q-value and takes roughly  $m_A = Am_N$  the threshold energy per nucleon is given by

$$T_{beam}^{thr} = m_\pi \frac{A_1 + A_2}{A_1 A_2} + \frac{m_\pi^2}{2A_1 A_2 m_N}. \quad (2.10)$$

Therefore the threshold beam energy per nucleon can be much lower than 280 MeV/u. For the studied reaction  ${}^3\text{He}+{}^4\text{He}$  Eq. 2.10 gives  $T_{beam}^{thr} = 79.6$  MeV/u. The exact calculation which takes the Q-value into account (Eq. 2.9) yields 78.8 MeV/u or 236.3 MeV in total.

At the beam energy of 258 MeV the center-of-mass kinetic energy is 145.5 MeV in the initial state and 12.1 MeV in the final state with a  ${}^7\text{Be}$  in the ground state. A distinguishing feature of such reactions is the huge momentum transfer. In the center-of-mass system the initial momentum of particles is  $p_i=687$  MeV ( $3.5 \text{ fm}^{-1}$ ) and the final momentum is  $p_f=58$  MeV ( $0.3 \text{ fm}^{-1}$ ). Usually, the available energy in the reactions are characterized by the quantity  $\eta = \frac{p_{c.m.}^\pi}{m_\pi}$  which is 0.4 in this experiment.

The ground states of the projectile  ${}^3\text{He}$  and the target  ${}^4\text{He}$  have spin-parity assignment  $\frac{1}{2}^+$  and  $0^+$ , respectively. A pion is a pseudoscalar particle, i.e. its spin-parity state is  $0^-$ . The low energy states of the final nucleus are shown in Table 2.1. Because of their negative parity the orbital angular momenta of the projectile-target relative motion and the pion orbital momentum must have the same parity, therefore, their vector sum must be even. This implies the selection rules for the ground state and the first excited

CHAPTER 2. THEORETICAL BACKGROUND

Table 2.1: Low-energy levels of  ${}^7\text{Be}$ . Taken from [69]

$E_x$ (MeV $\pm$ keV)	$J^\pi; T$	$\tau$ or $\Gamma_{\text{c.m.}}$	Decay
g.s.	$\frac{3}{2}^-; \frac{1}{2}$	$\tau_{1/2} = 53.22 \pm 0.06$ d <sup>a</sup>	$\epsilon$ -capture
$0.42908 \pm 0.10$	$\frac{1}{2}^-; \frac{1}{2}$	$\tau_m = 192 \pm 25$ fsec	$\gamma$
$4.57 \pm 50$	$\frac{7}{2}^-; \frac{1}{2}$	$\Gamma = 175 \pm 7$ keV	${}^3\text{He}, \alpha$
$6.73 \pm 100$	$\frac{5}{2}^-; \frac{1}{2}$	1.2 MeV	${}^3\text{He}, \alpha$
$7.21 \pm 60$	$\frac{5}{2}^-; \frac{1}{2}$	$0.40 \pm 0.05$ <sup>a</sup>	p, ${}^3\text{He}, \alpha$
$9.27 \pm 100$	$\frac{7}{2}^-; \frac{1}{2}$		p, ${}^3\text{He}, \alpha$
9.9	$\frac{3}{2}^-; \frac{1}{2}$	$\approx 1.8$ MeV	p, ${}^3\text{He}, \alpha$
$11.01 \pm 30$	$\frac{3}{2}^-; \frac{3}{2}$	$320 \pm 30$ keV	p, ${}^3\text{He}, \alpha$
17 <sup>b</sup>	$\frac{1}{2}^-; \frac{1}{2}$	$\approx 6.5$ MeV	${}^3\text{He}$

state shown in Table 2.2. Only the lowest pion orbital angular momenta are shown since the higher ones are less probable near the threshold. The higher excited states are particle unstable and cannot be detected by the experimental setup.

If one looks at the isospin states in the reaction, there is a pionic fusion reaction  ${}^4\text{He}({}^3\text{He}, \pi^+){}^7\text{Li}$  which has been measured [46] and its final state is related to the  $\pi^0 + {}^7\text{Be}$  final state by isospin rotations. If the small isospin breaking effects are neglected, the cross sections of these two reactions scale with the squares of Clebsch-Gordan coefficients connecting the initial and the final states

$$\frac{\sigma_{\pi^+}}{\sigma_{\pi^0}} = \frac{|\langle \frac{1}{2} \quad -\frac{1}{2} \quad 1 \quad 1 \mid \frac{1}{2} \quad \frac{1}{2} \rangle|^2}{|\langle \frac{1}{2} \quad \frac{1}{2} \quad 1 \quad 0 \mid \frac{1}{2} \quad \frac{1}{2} \rangle|^2} = 2, \quad (2.11)$$

where in both cases the initial state is of isospin  $\frac{1}{2}$  since the ground states of  ${}^3\text{He}$  and  ${}^4\text{He}$  have isospins  $\frac{1}{2}$  and 0, respectively, and the final states differ

## CHAPTER 2. THEORETICAL BACKGROUND

Table 2.2: Selection rules for the studied pionic fusion reaction.  $L_i$  is the orbital angular momentum of the projectile-target relative motion,  $J^\pi$  is the final nuclear state of  ${}^7\text{Be}$  and  $l_\pi$  is the orbital angular momentum of the pion motion in the center-of-mass system.

$L_i$	$J^\pi$	$l_\pi$
d	$\frac{3}{2}^-$	s
p		p
s, d		d
s	$\frac{1}{2}^-$	s
p		p
d		d

in the pion isospin projection which is 1 for the positive pion and 0 for the neutral. This relation allows to use the model calculations performed for the reaction with a positive pion for comparison.

The two-body final state and the ignorance of the polarizations requires only one kinematical variable to specify the kinematics. Usually this is the pion polar angle in the center-of-mass system. In the center-of-mass system the pion kinetic energy is fixed and in the laboratory system there is a unique relationship between the pion polar angle and its kinetic energy. Actually, in the experiment there are three particles since the pion decays into two photons which increases the number of kinematical variables necessary for the determination of the kinematics. An additional constraint is that the invariant mass of the two photons must be equal to the neutral pion mass. More about this issue will be discussed in Ch. 5.



## 2.2 Cross section formalism

The general cross section for a reaction with several final-state particles is given by

$$d\sigma(\mathbf{k}_1, \mathbf{k}_2, \dots, \mathbf{k}_n) = (2\pi)^4 \frac{E_{A_1} E_{A_2}}{E P_i} |T(\mathbf{k}_1, \mathbf{k}_2, \dots, \mathbf{k}_n)|^2 dk_1^3 dk_2^3 \dots dk_n^3 \delta^3\left(\sum_{i=1}^n \mathbf{k}_i\right) \delta\left(E - \sum_{i=1}^n \epsilon_i\right) \quad (2.12)$$

where  $\mathbf{k}_i$  and  $\epsilon_i$  are the momenta and energies of the outgoing particles, respectively,  $E_{A_1}$  and  $E_{A_2}$  are the energies of the projectile and the target, respectively,  $P_{in}$  is the relative momentum of the initial state. All quantities are given in the center-of-mass system.  $T$  is the transition matrix from the initial to the final state and comprises all information about the dynamics of the reaction.

For a two-body final state Eq. 2.12 reduces to the differential cross section

$$\frac{d\sigma}{d\Omega_{c.m.}} = \frac{1}{8\pi^2} \frac{E_{A_1} E_{A_2} E_B k_\pi}{E_{c.m.}^2 P_i} \frac{1}{2s_1 + 1} \frac{1}{2s_2 + 1} \sum_{f,i} |T_{fi}|^2, \quad (2.13)$$

where  $E_B$  is the energy of the fused nucleus B and  $k_\pi$  is the pion momentum. The sum goes over all spin projections in the initial and the final state and the summation is averaged over the initial spin states. It gives a factor of  $\frac{1}{2}$  since the spins of  ${}^4\text{He}$  and  ${}^3\text{He}$  are 0 and  $\frac{1}{2}$ , respectively.

The physics of the process is contained in the T-matrix which is defined as

$$T_{fi} = \langle \mathbf{k}_\pi, B(J, I) | T | A_1 A_2 \mathbf{P}_i \rangle, \quad (2.14)$$

where the interaction mechanism is contained in the transition matrix  $T$ . It is bracketed between the initial and the final state. The initial state contains the internal structure wave functions of the projectile  $A_1$  and the target  $A_2$  and the relative motion characterized by the relative momentum  $\mathbf{k}$ . In the final state there is the fused nucleus B in a state with quantum numbers J and I. Also, the pion is produced and its motion is described by the momentum

$\mathbf{k}_\pi$  in the center-of-mass system.

## 2.3 Pion-nucleon interaction

The pion is introduced as a particle which is exchanged between two nucleons. The one-pion-exchange diagram is shown in Fig.2.2a. The basic vertex in the pion-nucleon interaction is a pseudovector coupling in Fig. 2.2b and its Hamiltonian density is given by

$$\mathcal{H}_{pv} = \frac{f_{\pi NN}}{m_\pi} \bar{\Psi} \gamma^\mu \gamma^5 \boldsymbol{\tau} \Psi \cdot \partial_\mu \boldsymbol{\Phi}, \quad (2.15)$$

where  $\Psi$  and  $\boldsymbol{\Phi}$  are the nucleon and the pion fields, respectively,  $\gamma^\mu$  are the Dirac  $\gamma$ -matrices,  $\gamma^5 = i\gamma^0\gamma^1\gamma^2\gamma^3$  and  $\boldsymbol{\tau}$  is the nucleon isospin operator. The coupling constant  $f_{\pi NN}^2$  equals 0.08. The non-relativistic approximation is often used

$$\mathcal{H}_{pv}^{nonrel} = \frac{f_{\pi NN}}{m_\pi} \boldsymbol{\sigma} \nabla \boldsymbol{\tau} \boldsymbol{\Phi}, \quad (2.16)$$

where  $\boldsymbol{\sigma}$  is the nucleon spin operator. This represents a possible elementary pion production mechanism but because of energy-momentum conservation constraints at least two nucleons must interact. This is the p-wave non-resonant production mechanism and is shown in Fig. 2.2c. Close to the

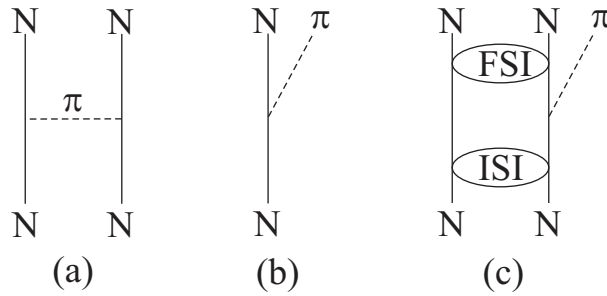


Figure 2.2: The one-pion-exchange in the nucleon-nucleon interaction (left), the basic vertex of the pion-nucleon coupling (middle) and the non-resonant p-wave pion production which has to include the initial- or the final-state interactions (right).

CHAPTER 2. THEORETICAL BACKGROUND

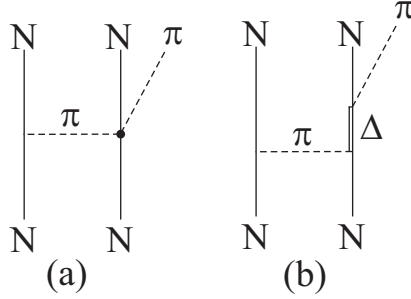


Figure 2.3: S-wave (a) and  $\Delta$ -isobar (b) mechanisms for pion production.

threshold the final-state interactions are very important since the nucleons in the final state have small relative momentum for which the interaction is very strong.

Besides the p-wave non-resonant pion production a pion can be produced in the s-wave and via the  $\Delta$ -isobar intermediate state (Fig. 2.3). The s-wave production is very weak but dominant near the production threshold. The pion is produced on one nucleon and re-scattered on the other. Its re-scattering vertex is given by

$$\mathcal{H}_{s-wave} = 4\pi \frac{\lambda_1}{m_\pi^2} \bar{\Psi} \gamma^\mu \boldsymbol{\tau} \Psi \cdot (\boldsymbol{\Phi} \times \partial_\mu \boldsymbol{\Phi}) + 4\pi \frac{\lambda_0}{m_\pi} \bar{\Psi} \Psi \cdot (\boldsymbol{\Phi} \boldsymbol{\Phi}), \quad (2.17)$$

where the two terms correspond to the nucleons in the isovector and isoscalar state. The parameters  $\lambda_1$  and  $\lambda_0$  are obtained from the  $\pi$ -nucleon scattering.

The most dominant mechanism is the  $\Delta$ -isobar mechanism whose coupling to a pion and a nucleon is given by

$$\mathcal{H}_\Delta = -\frac{f_{\pi N \Delta}}{m_\pi} \bar{\Psi}_\Delta^\mu \boldsymbol{T} \Psi \cdot \partial_\mu \boldsymbol{\Phi} + h.c., \quad (2.18)$$

where  $\Psi_\Delta^\mu$  is the  $\Delta$ -isobar field and  $\boldsymbol{T}$  is the isospin transition operator between  $I=\frac{1}{2}$  and  $I=\frac{3}{2}$  states. The coupling constant  $f_{\pi N \Delta}^2$  is very strong and equals 0.37. Although the mass of the  $\Delta$ -isobar is 1232 MeV it is shown that it must be taken into account even close to the threshold [14, 27]. In the nuclear medium the interaction shifts the effective mass of the resonance to

## CHAPTER 2. THEORETICAL BACKGROUND

lower energies and therefore increases its importance.

All these mechanisms turned out to be insufficient for reproducing the new experimental data [17] near the threshold. Since then progress has been made in the theoretical explanation of the data [14] but these new mechanisms have never been applied to the pionic fusion reactions.

### 2.4 Models for pionic fusion

The first observation of the exclusive pion production with light nuclei in the 1970s and 1980s initiated theoretical work which resulted in several models. There are two important aspects in pionic-fusion reactions: a mechanism that converts almost all free energy into one degree of freedom - a pion field and initial and final nuclear states, i.e. their wave functions, especially a high-momentum component of the final wave function. At the absolute threshold a coherent action of all nucleons is needed, otherwise there is not sufficient energy available for the pion production. This implies that the nuclear structure of the initial nuclei and of the fused nucleus is very important. To describe the pionic fusion it is necessary to build a mechanism which can link the elementary process of pion production with the collective motion of all nucleons.

The need for a collective degree of freedom motivated Huber et al. [60] to use a  $\Delta$ -excitation as a storage of the energy which can then be transferred to the pion field without sharing the energy among many nucleons. Germond and Wilkin [64] tried to avoid uncertainties of a microscopic model by using a mechanism which includes a subprocess that was known from the measurements. Both of the models emphasize the importance of the clustering structure of the final nucleus. A model that explores the clustering with more sophistication was developed by Kajino et al. [67]. It supposes that the elementary process is a simple non-resonant p-wave production but predicts the behavior close to the resonant production model.

### 2.4.1 Intermediate $\Delta$ resonance excitation

The first model that tried to reproduce observed cross sections was proposed by Huber et al. [60]. It is based on a  $\Delta$ -resonance excitation within a nucleus as a temporary storage of the energy and bridge over the thermalization of the system. The  $\Delta$ -resonance naturally decays into a pion and a nucleon. Taking the rough kinematical consideration of the reaction mechanism, the  $\Delta$  should not have impact on the reactions at such low energy, but it is shown that the  $\Delta$ -nucleon interaction lowers the energy of the intermediate state and therefore couples to both the entrance and exit channels. Those intermediate excited states containing the first nucleon resonance are examined with many reactions like elastic and inelastic pion scattering and (pion,gamma) reactions.

The mechanism in the model is presented in the diagram in Fig. 2.4. It proceeds in three steps. The first step is described by the "ignition" operator  $W$  which slows down the incoming nuclei by the interactions between nucle-

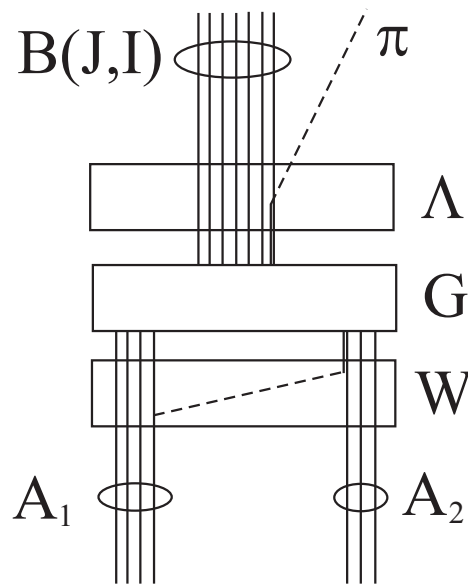


Figure 2.4: Resonant mechanism for pionic fusion proposed by [60]. Three steps include the ignition operator  $W$ , propagation operator  $G$  of the resonant nuclear state and the decay operator  $\Lambda$ .

## CHAPTER 2. THEORETICAL BACKGROUND

ons in the projectile and the target. The many-body operator  $W$  consists of pairwise nucleon-nucleon interactions

$$W = \sum_{i \in A_1} \sum_{i \in A_2} w(i, k) \quad (2.19)$$

Each of the two-nucleon terms can be represented in momentum space

$$w(i, k) = \int d^3q w(q) e^{-i\mathbf{q}\mathbf{r}_{ik}} f_{NN\pi}(i) g_{N\Delta\pi}(k) \quad (2.20)$$

where  $w(q)$  is the pion propagator and the operators  $f_{NN\pi}(i)$  and  $g_{N\Delta\pi}(k)$  represent a pion production on one nucleon (Eq. 2.15) and a pion absorption with a  $\Delta$  excitation on another nucleon (Eq. 2.18), respectively.

Transformation of the relative nucleon coordinates leads to the separation of the internal motion of nucleons and the relative motion of nuclear centers of mass

$$\mathbf{r}_{ik} = \mathbf{r}_i - \mathbf{r}_k = \mathbf{v}_i(\rho) - \mathbf{v}_k(\eta) + \mathbf{R}_{12}, \quad (2.21)$$

where  $\rho$  and  $\eta$  are the internal nucleon coordinates within the target and the projectile and  $\mathbf{R}_{12}$  is the relative coordinate between them.

The operator  $W$  can be written as a product of three operators

$$W = \int d^3q w(q) F_{\mathbf{q}}(\rho) G_{\mathbf{q}}(\eta) H_{\mathbf{q}}(\mathbf{R}_{12}), \quad (2.22)$$

where  $F_{\mathbf{q}}(\rho)$  and  $G_{\mathbf{q}}(\eta)$  act on the projectile and the target nuclei and  $H_{\mathbf{q}}(\mathbf{R}_{12})$  on their relative motion. This shows how the pairwise interaction between nucleons influences the relative collective motion.

The produced  $\Delta$  propagates within a nuclear medium through possible states of energies. The propagator  $G$  contains all contributions of such states

$$G = \sum_{\mu} |\mu\rangle \frac{1}{\omega - E_{\mu}} \langle \mu| \quad (2.23)$$

In order to facilitate the calculation those energies are replaced by one average energy  $\bar{E}$ .

## CHAPTER 2. THEORETICAL BACKGROUND

Finally the excited nuclear state with the  $\Delta$ -resonance decays into a pion and the ground or some low-energy excited state of the final nucleus. The operator responsible for that process is

$$\Lambda = \int d^3k e^{-i\mathbf{k}(\mathbf{r}_N - \mathbf{r}_\pi)} G_{\mathbf{k}}, \quad (2.24)$$

where  $G_{\mathbf{k}}$  is a sum of decay  $\pi N\Delta$  vertices over all nucleons in the final nucleus.

The transition operator shows a preference for the final nuclear states whose cluster structure corresponds to the initial target-projectile fragmentation. The final nucleon wave function is taken to be a cluster wave function since it couples to the initial-state relative motion most effectively. The relative motion of the clusters is described by the harmonic oscillator wave

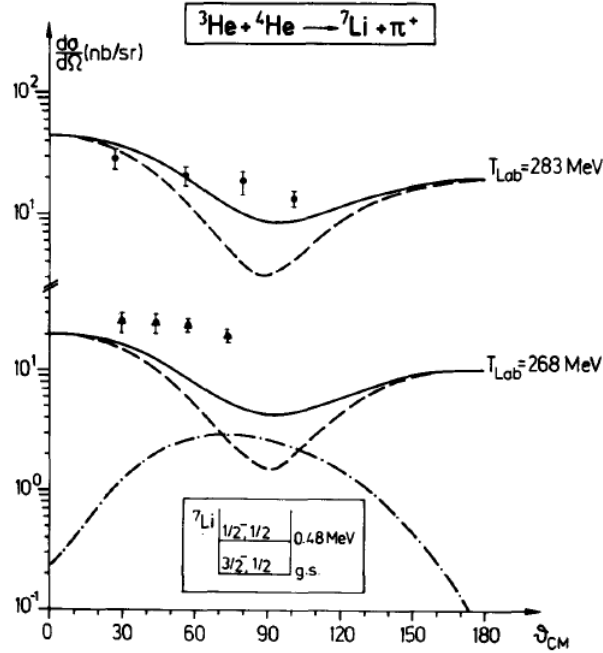


Figure 2.5: The  $\Delta$ -isobar model predictions confronted with the pionic fusion data [46]. The contributions from the ground (the first excited) state are shown separately by the dot-dashed (dashed) line. Taken from [61].

## CHAPTER 2. THEORETICAL BACKGROUND

function.

The differential cross section obtained for the  ${}^3\text{He}+{}^4\text{He}$  pionic-fusion reaction is shown in Fig. 2.5. The experimental data from [46] are shown. The cross section is calculated for the reaction with the positive pion and  ${}^7\text{Li}$  in the ground and the first two excited states. Since our studied reaction is related to this one by isospin symmetry, the results of this model can be used for a comparison with the data obtained in the  ${}^3\text{He}+{}^4\text{He}\rightarrow{}^7\text{Be}+\pi^0$  experiment.

The authors estimate the uncertainty to a factor of two due to the neglecting of the non-resonant pion production mechanism and the closure approximation.

### 2.4.2 Semi-empirical model

To avoid the uncertainties within a microscopic approach, a model of Germond and Wilkin [64] relies on the measured cross sections of simpler reactions which is supposed to be a subprocess of the more complex reaction. That simpler reaction is  $p+{}^3\text{He}\rightarrow{}^4\text{He}+\pi^+$  and there are measurements of

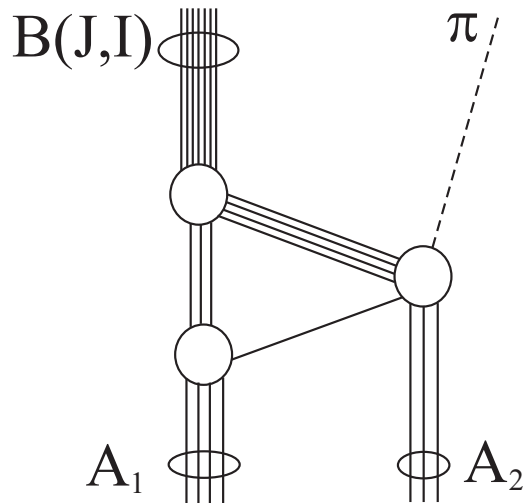


Figure 2.6: Reaction mechanism of the model of Germond and Wilkin [64]. It is based on simpler process  ${}^3\text{He}(p,\pi^+){}^4\text{He}$



## CHAPTER 2. THEORETICAL BACKGROUND

the cross section that can be used to derive the transition amplitude. The amplitude is then used as a part of the total transition amplitude in the calculation of the cross section of the more complex reaction.

The reaction diagram is shown in Fig. 2.6. The ingredients are the transition matrix of  ${}^3\text{He}(p, \pi^+){}^4\text{He}$ , the initial wave function of the target ( ${}^4\text{He}$ ) and the wave function of the final nuclear state. The transition matrix element is

$$\begin{aligned}
 T_{if} = & X_\alpha X_p \int \Phi_B^*(\mathbf{K} - \mathbf{Q}, \boldsymbol{\eta}) \\
 & \langle \mathbf{k}_\pi, \mathbf{K} + \mathbf{p}_B - (1 - m_p/m_A)\mathbf{p}_A | T_{\tau p \rightarrow \pi \alpha} | \mathbf{k}_\tau, \mathbf{K} + m_p/m_A \mathbf{p}_A \rangle \\
 & \Phi_A(\mathbf{K}, \boldsymbol{\eta}) d\mathbf{K} d\boldsymbol{\eta}, \tag{2.25}
 \end{aligned}$$

where the spectroscopic factors  $X_\alpha X_p$  are related to the number of alphas in the created nucleus and the number of protons in the target nucleus,  $\Phi_B$  is the wave function of the final state,  $\Phi_A$  the wave function of the target,  $\mathbf{K}$  is the proton momentum within the target,  $\boldsymbol{\eta}$  represents the internal variables of the intermediate cluster, and  $\mathbf{Q}$  is the momentum transfer and equals

$$\mathbf{Q} = (1 - m_p/m_A)\mathbf{p}_A - (1 - m_\alpha/m_B)\mathbf{p}_B. \tag{2.26}$$

The transition amplitude of the simpler process generally has the following form

$$\langle f | T_{\tau p \rightarrow \pi \alpha} | i \rangle = f_1 \mathbf{S} \mathbf{k}_\tau + f_2 \mathbf{S} \mathbf{k}_\pi, \tag{2.27}$$

where the particles in the entrance channel ( $p$  and  ${}^3\text{He}$ ) must be in the isospin triplet state which couples to the initial and the final momenta. The parameters  $f_1$  and  $f_2$  can be determined in polarization measurements. This transition amplitude is then used as an input in Eq. 2.25. The wave functions of the final state have a cluster structure with  ${}^4\text{He}$  and  ${}^3\text{He}$  clusters. The inter-cluster motion is described by the harmonic oscillator or the Woods-Saxon wave functions.

The results of the model are shown in Fig. 2.7 for the  ${}^7\text{Li} + \pi^+$  final state. By the isospin symmetry transformation these calculations may be applied to the  ${}^7\text{Be} + \pi^0$  final state.

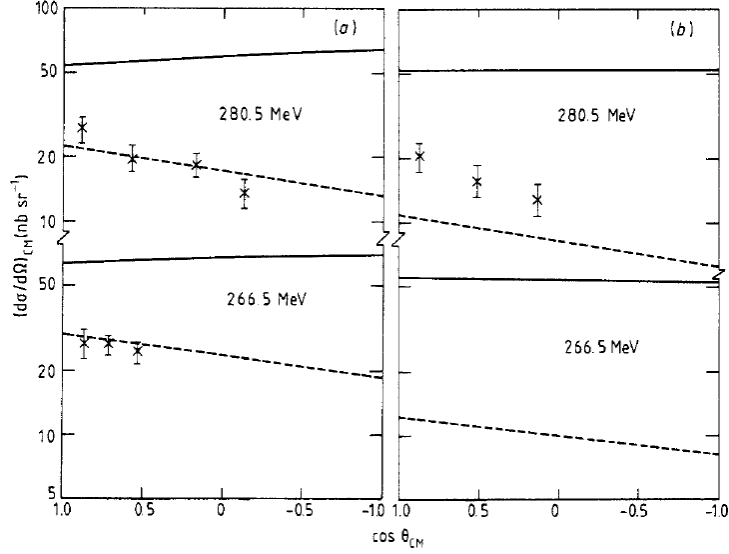


Figure 2.7: The results of the semi-empirical model compared to the data [46]. Different lines are associated to different wave functions of the final nucleus - dashed for a harmonic oscillator wave function and solid for a Woods-Saxon wave function. Taken from [64].

### 2.4.3 Interaction cluster model

Cluster wave functions which reproduce the bulk properties of beryllium and lithium nuclei are a basis of the model of Kajino et al. [67]. The authors showed that the genuine cluster wave function is crucial for the reproduction of the measured data. Unlike the previous two models that also used the cluster structure of the final nucleus, this one takes into account the strong clustering correlations, the distortion of the entrance channel and the Pauli exclusion principle. The calculation is carried out for the two reactions with a neutral and a positive pion in the final state. Those are related by the isospin symmetry and the cross section for the charged pion is two times higher than that for the neutral pion. All the considerations can be analogously applied to both reactions by exchanging a proton with a neutron.

The final nuclear states are described by correlated microscopic cluster

CHAPTER 2. THEORETICAL BACKGROUND

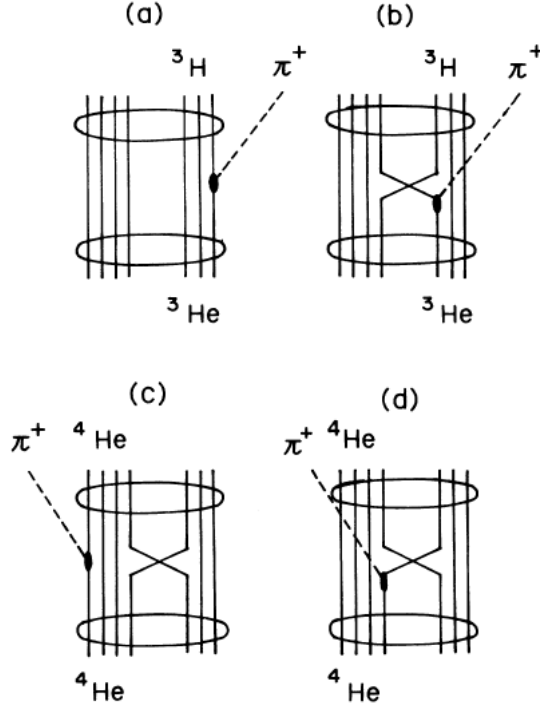


Figure 2.8: Different contribution to the transition amplitude for the cluster model [67].

model wave function

$$\langle \xi_\alpha \xi_\tau \mathbf{r} | J M \rangle = \sqrt{\frac{4!3!}{7!}} A_{\alpha\tau} \left\{ [\phi_\alpha(\xi_\alpha) \phi_\tau^{(1/2)}(\xi_\tau) \otimes i^L Y^{(L)}(\hat{\mathbf{r}})]_M^{(J)} \chi_{JL}(r) \right\}, \quad (2.28)$$

where  $A_{\alpha\tau}$  is the antisymmetrizer of nucleons and  $\phi_\alpha(\xi_\alpha)$  and  $\phi_\tau^{(1/2)}(\xi_\tau)$  are the internal wave functions of  ${}^4\text{He}$  and  ${}^3\text{He}$  (or a triton), respectively.  $\chi_{JL}(\mathbf{r}) = \chi_{JL}(r) i^L Y^{(L)}(\hat{\mathbf{r}}) \chi_{JL}(r)$  is the wave function of the relative inter-cluster motion. It is a solution of the equation of motion obtained by the Resonating Group Method [68]. The initial scattering state is constructed by superposing the cluster wave functions (Eq. 2.28)

$$\langle \xi_\alpha \xi_\tau \mathbf{r} | \frac{1}{2} \nu \rangle = \sum_{L,J} \sqrt{4\pi} \sqrt{2L+1} \langle L 0 \frac{1}{2} \nu | J \nu \rangle \langle \xi_\alpha \xi_\tau \mathbf{r} | J M \rangle. \quad (2.29)$$

## CHAPTER 2. THEORETICAL BACKGROUND

For the production operator they used just the Galilean-invariant pseudovector  $NN\pi$  coupling. The two-body terms like the s-wave coupling and the  $\Delta$ -resonance intermediate state are neglected here. The production operator is

$$H = -\frac{\sqrt{4\pi}f}{m_\pi} \int \sum_{N=1}^7 \delta(\mathbf{r}_\pi - \mathbf{r}_N) \sigma_N \left[ \left(1 + \frac{\omega}{7M_N}\right) \nabla_{\pi C} - \frac{\omega}{M_N} \nabla_{NC} \right] \tau_N \phi(\mathbf{r}) \pi d\mathbf{r}. \quad (2.30)$$

It differs from the ordinary  $\sigma \nabla$  in the transformation of coordinates from the reaction center-of-mass system to the  $\pi$ -nucleon center-of-mass system and the recoil term which assures the Galilean invariance.

It is shown that the initial center-of-mass motion of the projectile and the target strongly couples to the high-momentum part of the inter-cluster nuclear wave function. The comparison is made with the shell model calculation and the difference in the cross section is an order of magnitude. This is due to the increase of the high-momentum part of the cluster wave function with respect to the shell-model wave function. Since in the shell model only

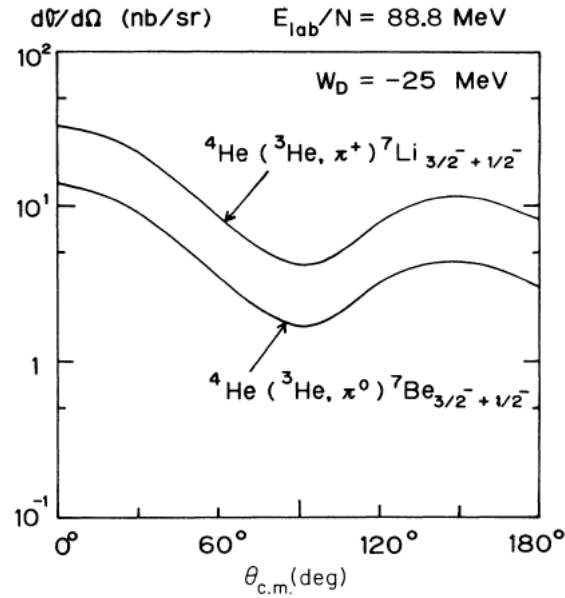


Figure 2.9: The results of the cluster model taken from [67].

## CHAPTER 2. THEORETICAL BACKGROUND

the Fermi motion of the nucleons is present it is consistent with the findings of [34] for inclusive pion production.

Also, the details of the mechanisms involved are examined (see Fig. 2.8). The mechanism (a) is shown to be dominant. The T-matrix for this specific mechanism is factorized in two parts

$$T_{M_f\nu} = \langle \phi_\tau | h_\tau | \phi_{^3He} \rangle \int \chi_f^*(\mathbf{r}) e^{i(\mathbf{k}_i - \frac{4}{7}\mathbf{k}_\pi)\mathbf{r}} d\mathbf{r}. \quad (2.31)$$

The first part describes the pion production on a nucleon within the  $^3\text{He}$  (or the triton) and the second shows the intercluster motion wave function coupled to the momentum transfer in the reaction. It can be seen that the high-momentum components of the intercluster wave function are crucial since the momentum transfer is very high.

The results are shown in Fig. 2.9 and are similar to the results of the  $\Delta$ -excitation model, but without inclusion of the  $\Delta$ -isobar. On the other hand, the  $\Delta$ -excitation model neglects the non-resonant pion production.

## Chapter 3

# Experimental setup

The pionic fusion experiments took place in 2006 at the Kernfysisch Versneller Instituut in Groningen, The Netherlands. The floor plan of the experimental area is sketched in Fig. 3.1 where the accelerator, the beam lines and the available detector systems are shown. The central device is the AGOR (*Accelérateur Groningen Orsay*), an isochronous superconducting cyclotron capable of accelerating light and heavy ions. It is 3.6 m high and has a diameter of 4 m. Particles are accelerated in three sectors. The maximum magnetic field strength is 4 T. The maximum beam energy per nucleon obtained by the accelerator depends on the mass to charge ratio of accelerated particles. The maximum possible energy for protons is 190 MeV and for heavier ions 95A MeV.

There are three ion sources used for producing different ions. For this experiment the  ${}^3\text{He}^{2+}$  ions are made in the ECRIS (*Electron Cyclotron Resonance Ion Source*). Lighter unpolarized ions, i.e. protons and deuterons are produced in the CUSP source, whereas the third ion source POLIS (*Polarized Ion Source*) produces polarized light ions.

The average beam current in this experiment was 0.13 nA. The beam spot at the target location could be observed on a piece of scintillating ZnS, placed in the position of the target. The beam spot had a diameter of 2 mm which is 20% of the target container diameter. The frequency of the accelerator for the  ${}^3\text{He}^{2+}$  beam energy of 258 MeV was 43 MHz.

### CHAPTER 3. EXPERIMENTAL SETUP

VIEW ON THE AGOR CYCLOTRON VAULT AND EXPERIMENTAL AREA

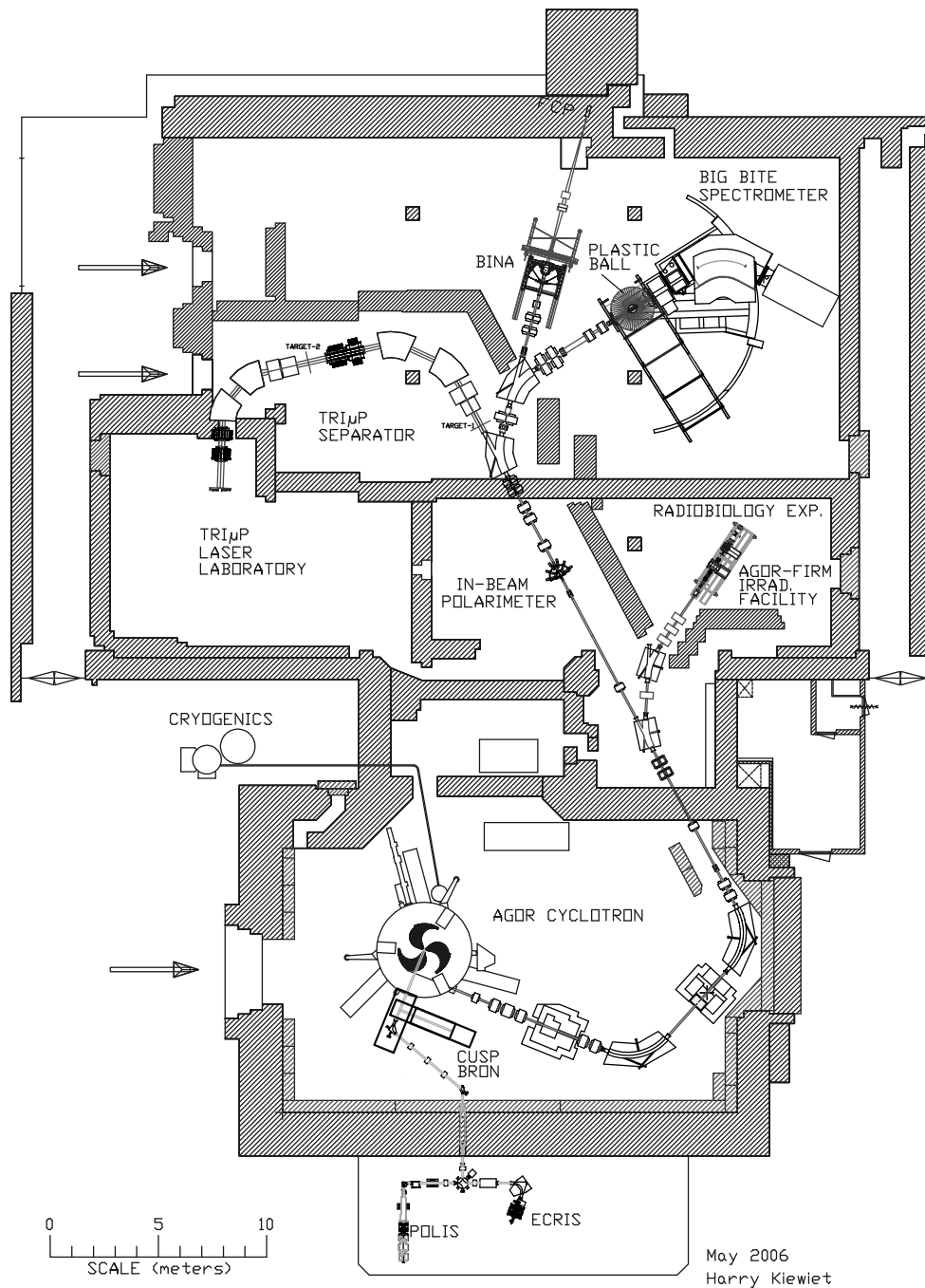


Figure 3.1: The KVI floor plan.

CHAPTER 3. EXPERIMENTAL SETUP

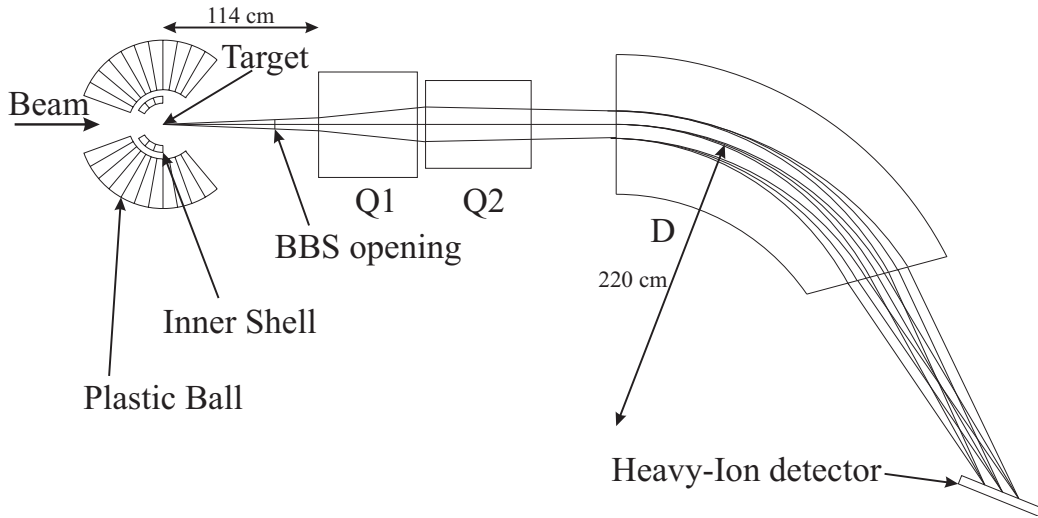


Figure 3.2: The experimental setup used in pionic fusion experiments at KVI. On the left side, serving as photon detectors the Plastic Ball and the Inner Shell are positioned around the target. Rays of different momenta and directions passing through the quadrupoles and the dipole of the BBS are sketched. The Heavy-Ion detector is located at the focal plane.

The experiment took place at the end of the beam line in the upper right part of the KVI floor plan in Fig. 3.1. In the experiment all reaction products were detected in a huge part of the phase space and with a sufficient resolution to reject the background and fully reconstruct an event. The reaction products are particles which are very different in their nature - the fused nucleus is a heavy charged particle, whereas the neutral pion is detected via its decay into two photons. This requires a combination of different detectors and measuring techniques. The experimental setup is shown in Fig. 3.2. It consists of the Plastic Ball (PB) [70] and its Inner Shell (IS) [71] employed as photon detectors. They are positioned around the target. The Big-Bite Spectrometer (BBS) [72], downstream of the beam line, together with the Heavy-Ion detector (HI) [73] in the focal plane detects the nuclear fragments.



### 3.1 The liquid helium target

In order to obtain a sufficiently high luminosity a liquid helium target was used. The liquid helium target for this experiment has been developed in a collaboration of Vacuum Specials Co. and the KVI target group [74].

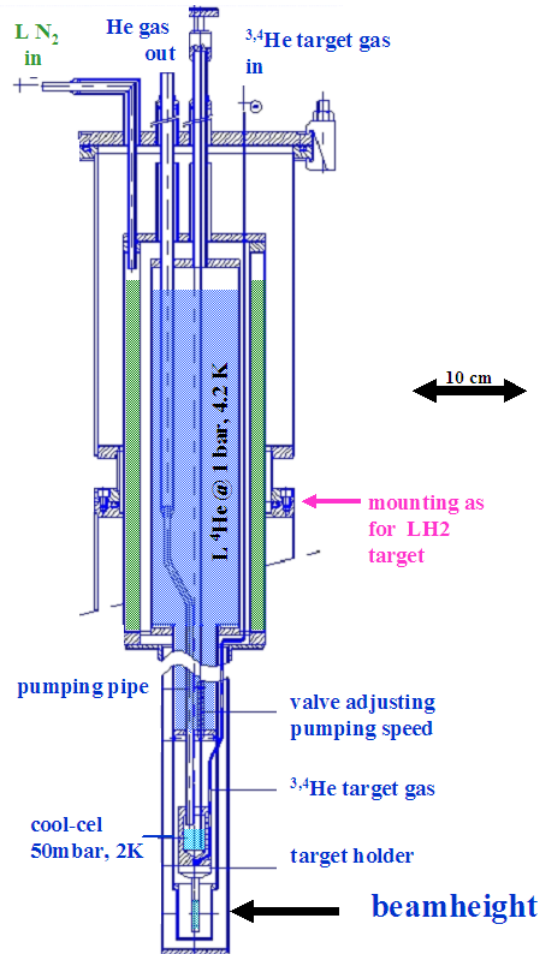


Figure 3.3: The liquid helium target assembly.

A layout of the target assembly is shown in Fig. 3.3. The main part is a 2 liter cylindrical container filled with liquid helium at a temperature of approximately 4.2 K and at atmospheric pressure. It is kept inside a 2.2-liter liquid nitrogen cylindrical shell which decreases the loss of heat. The two-step cooling saves energy and gas (liquid nitrogen evaporation energy is

### CHAPTER 3. EXPERIMENTAL SETUP

much lower than the helium one). The liquid helium level was monitored and kept at a constant value by adjusting the helium flow through the container. Liquid helium is pumped out through a needle valve by a roots pump obtaining a temperature of 2 K in the so-called 1K pot. The target itself is produced by bringing the liquid helium from a high-pressure vessel via a 100 mbar buffer, passing the cold helium container and the 1 K pot and dripping into a cylindrical aluminum container closed with mylar 4  $\mu\text{m}$  foils. The vapor pressure of the liquid helium inside the target container was limited to values below 200 mbar in order to prevent a mylar foil burst. To achieve that, the temperature of the target cell had to be at approximately 2 K.

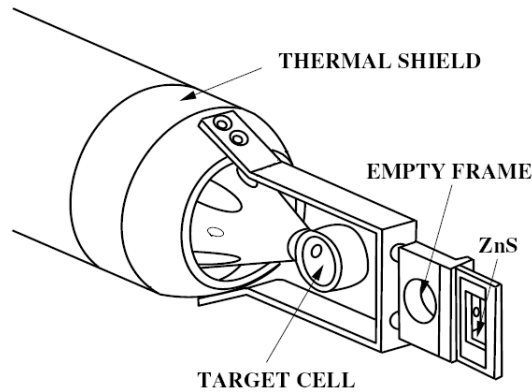


Figure 3.4: The target container, the empty target ring and the ZnS target were mounted vertically above each other.

During the experiment the system was continuously monitored and being adjusted to keep the temperature and therefore the pressure in a stable range.

The temperature of the LHe target was in the range of 2.13 - 2.14 K and the nominal target cell thickness is 1 cm which corresponds to a target thickness of  $135 \pm 5 \text{ mg/cm}^2$ . In such a thick target, particles (especially heavier and more charged), loose a considerable amount of energy or even get stopped. This is a serious drawback of the experiment and requires special attention in the data analysis. On the other hand the background reactions on the thick target increase the count rate and consequently the dead time of the system.

## CHAPTER 3. EXPERIMENTAL SETUP

Apart from the target container, an empty frame and a ZnS target were mounted on the target assembly (see Fig. 3.4). The whole assembly could move along slides so the different targets could be set into the beam line. The empty frame helps in determining the background coming from the interaction of the beam particles with the target container walls. With the ZnS scintillator target the beam spot could be observed and focused at the target position.

### 3.2 The Big-Bite Spectrometer

The BBS is a QQD-type magnetic spectrometer which was positioned near  $0^\circ$  scattering angle to deflect and momentum-analyze fusion products produced at small scattering angles. The spectrometer has a bending limit, called the K-value, of 430 MeV, a solid angle up to 13 msr and a momentum acceptance up to 25% (particles with a magnetic rigidity deviating less than  $\pm 12.5\%$  from the central rigidity are accepted in the spectrometer). There are three operational modes which differ in the positions of the quadrupole doublet with respect to the scattering chamber. The closer the doublet is placed to the scattering chamber, the larger the solid angle and the smaller the momentum acceptance. For the pionic fusion experiments, the spectrometer was used in the mode called "B" which has the momentum acceptance of 19% and a maximum horizontal (vertical) opening angle of  $3.80^\circ$  ( $8.03^\circ$ ). All characteristics of the mode "B" are shown in Table 3.1. The region between the target and the exit window right behind the focal plane of the BBS is kept in vacuum. The beam was collected in an internal Faraday cup inside the BBS vacuum. This way the total charge of incoming beam particles could be determined and the reaction products at small laboratory angles could be separated from the intense beam.

A few tests with well-known reactions were carried out to check the performance of the spectrometer together with a new heavy-ion detector positioned in front of the focal plane. These results will be outlined in Ch. 5.

A charged particle in a magnetic field with a velocity perpendicular to

### CHAPTER 3. EXPERIMENTAL SETUP

Table 3.1: The BBS design parameters for the operational mode "B".

Maximum solid angle	9.2 msr
Maximum horizontal opening angle	66 mrad
Maximum vertical opening angle	140 mrad
Momentum bite $\Delta p/p_0$	19%
Dispersion D	2.54 cm/%
Horizontal magnification $M_x$	-0.45
Vertical magnification $M_y$	-10.1
Bending limit K	430 MeV
Optimum resolution $\Delta E/E$	$4 \times 10^{-4}$
Radius of curvature	220 cm
Maximum dipole field	1.4 T
Distance target-entrance aperture	81.7 cm
Distance target-entrance Q1	114 cm

the field moves along a circular orbit of radius  $\rho$  which is given by

$$B\rho = \frac{p}{q}, \quad (3.1)$$

where  $B$  is the magnetic field strength,  $p$  the momentum of the particle and  $q$  its charge. The  $B\rho$  value is called rigidity. Usually the relative deviation from the central ray rigidity needs to be considered:

$$\delta = \frac{B\rho - B\rho_0}{B\rho_0}. \quad (3.2)$$

The dipole magnet creates the field which bends the particle trajectory whereas the quadrupoles are used for the focussing. By means of complex focal plane detectors like multi-wire chambers the measurement of not only rigidity but also the angles of incidence on the focal plane is possible. The ray-tracing method uses the magneto-optics to determine from the measured track parameters at the focal plane the kinematical observables at the target position. In our experiment only the rigidity of a particle could be measured. The ray-tracing simulations were used to determine the acceptance of the focal-plane detector.

### 3.3 The Heavy-Ion detector

The Heavy-Ion detector (HI) is placed in the vacuum chamber in front of the focal plane of the BBS (Fig. 3.2). A photograph of the detector is shown in Fig. 3.5.



Figure 3.5: The HI detector array seen from the exit of the dipole magnet. CsI(Tl) crystals are wrapped by aluminum foils. The PMTs and bases are in the red housing. Above the detectors there are vacuum-tight connectors for a signal readout and a high voltage supply.

The HI detector array consists of 60 CsI(Tl)/plastic phoswich modules in a segmented layer. Each of the phoswich modules has a cuboid geometry consisting of a CsI(Tl) crystal with a size of  $4\text{ cm} \times 1.3\text{ cm} \times 1.3\text{ cm}$  and a  $80\text{ }\mu\text{m}$  thin plastic scintillator covering one  $4\text{ cm} \times 1.3\text{ cm}$  face of the CsI(Tl) crystal (Fig. 3.6). The scintillators are optically coupled so that the light signals from both scintillators are collected on a common photomultiplier tube (PMT). The high voltage is supplied to the PMTs using a CAEN SY 1572 high-voltage mainframe providing positive high voltages ( $\sim 500\text{ V}$ ). Since they operate in a

### CHAPTER 3. EXPERIMENTAL SETUP

strong magnetic field the individual detector are magnetically shielded. The

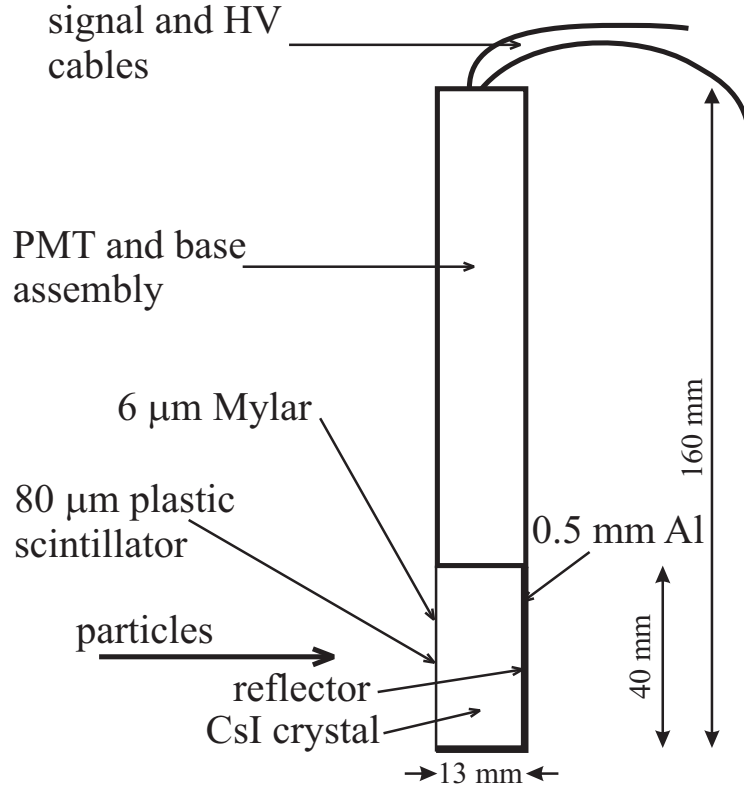


Figure 3.6: A single HI detector module contains scintillators, ADIT L13B03B180 PMT and integrated voltage divider. It is made by the Scionix Holland B.V. company [75].

scintillators are arranged in two parallel rows, 30 of them are positioned in the upper row with their PMTs pointing upward and 30 of them are positioned in the lower row with their PMTs pointing downward. Looking from the target in the beam direction, every module is oriented vertically such that the area facing impinging particles is  $1.3 \text{ cm} \times 4 \text{ cm}$ . The modules are positioned such that the angle of incidence of the particles is nearly perpendicular to the front face of the modules. The vertical orientation of the PMTs was chosen to keep the complete array as close as possible to the focal plane of the BBS. The distance between the front face of the module and the focal plane is nearly identical for all modules. A thickness of the CsI(Tl) crystal of 1.3 cm is

## CHAPTER 3. EXPERIMENTAL SETUP

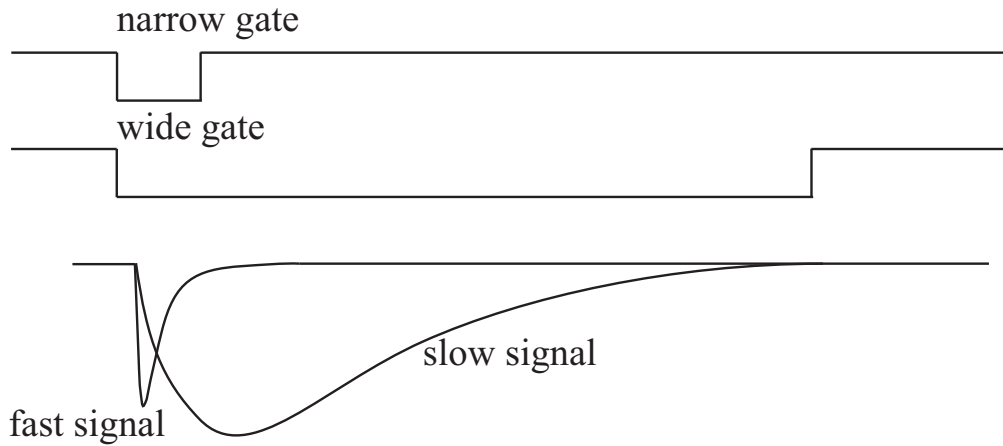


Figure 3.7: The scintillator signals for a phoswich detector and the integration gates. Different particles deposit relatively different amounts of energy in the two scintillators.

sufficient to stop all particles produced in the pionic fusion experiments so that the energy deposited in the scintillators is equal to the kinetic energy of the detected particles. Out of 60 installed detector modules, 58 operated satisfactorily and were successfully used in the pionic fusion experiments.

A difference in decay time constants of the slow CsI(Tl) ( $\sim 1\mu\text{s}$ ) and the fast plastic scintillator ( $\sim 3\text{ ns}$ ) enables a particle identification by a pulse-shape analysis (Sec. 5.1.1). The principle of the pulse-shape discrimination technique is shown in Fig. 3.7.

### 3.3.1 Readout electronics

The HI detector readout (see scheme in Fig. 3.8) was performed by standard CAMAC and NIM electronics. The CAMAC modules were controlled by CCA2-type controllers that were daisy-chained together with the electronics of other detectors. The chain was accessed by a CAMAC branch driver (CSE CBD 8210), a VME module connected to an Alpha VME processor and CORBO RCB 8047 trigger module.

The photomultiplier signals are pre-amplified by Phillips 776 amplifiers and split by an active analog splitter (Univ. Giessen). The first copy is

CHAPTER 3. EXPERIMENTAL SETUP

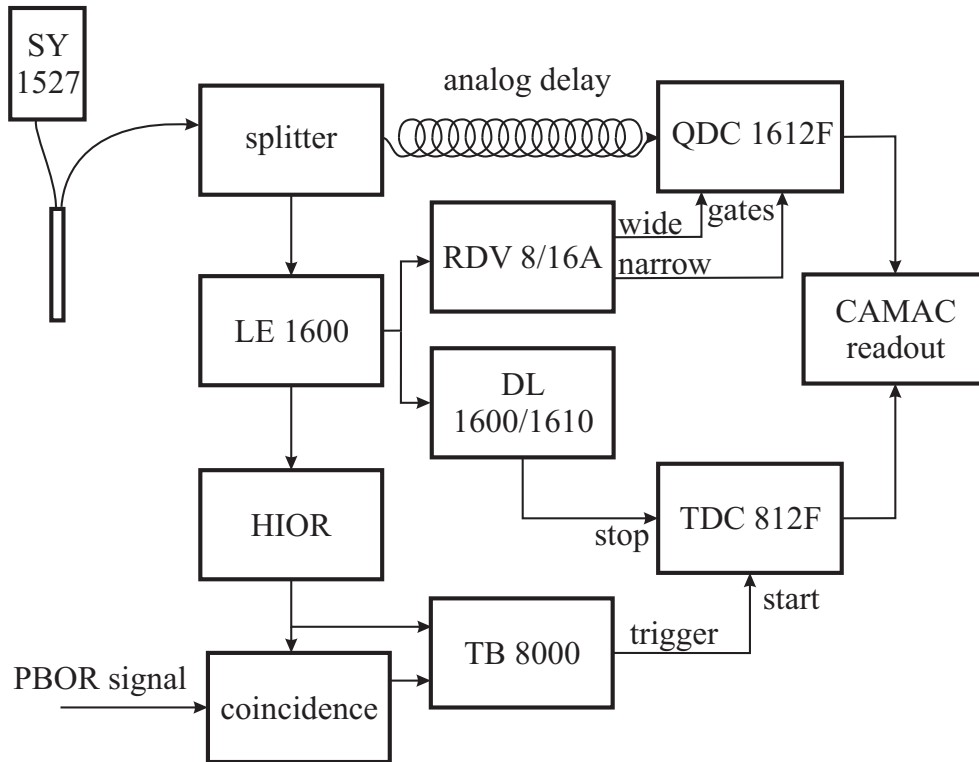


Figure 3.8: The HI detector electronic readout scheme. The unit labeled HIOR produces a logic OR signal of all output signals from the discriminators.

discriminated by 8-channel leading-edge GSI discriminators LE 1600. The digital signals are used for TDC stop signals and for QDC gate generation. The logic OR of all output discriminator signals (HIOR) is used for the trigger generation.

Another copy of the photomultiplier signal is delayed by  $\sim 375$  ns and sent to GAN'ELEC  $2 \times 8$ -channel charge-to-digital converters QDC 1612F. The signal is split at the input of a QDC in a nominal ratio 1:5. These two copies were integrated with a wide (1100 ns) and a narrow gate (110 ns), respectively, produced by GAN'ELEC gate and delay generators RDV 8/16A. The gates were derived individually, i.e. each channel produced gates in leading-edge discriminators triggered by the signal itself. The QDC data is used for a measurement of the energy deposition in the phoswich detectors



### CHAPTER 3. EXPERIMENTAL SETUP

and pulse-shape discrimination between different ion species.

8-channel time-to-digital converters GAN'ELEC TDC 812F worked in a common start mode where a trigger signal starts the time conversion. The conversion is stopped by individual detector signals delayed by GSI logic delay units DL 1600/1610 following a discriminator unit. The trigger signal is produced in a GSI TB 8000 trigger box and consists of signals from separate detectors as well as a coincidence between them with certain down-scaling factors. The PBOR signal is derived from the logic OR of the backward Plastic Ball detector modules with signals above a pre-defined threshold.

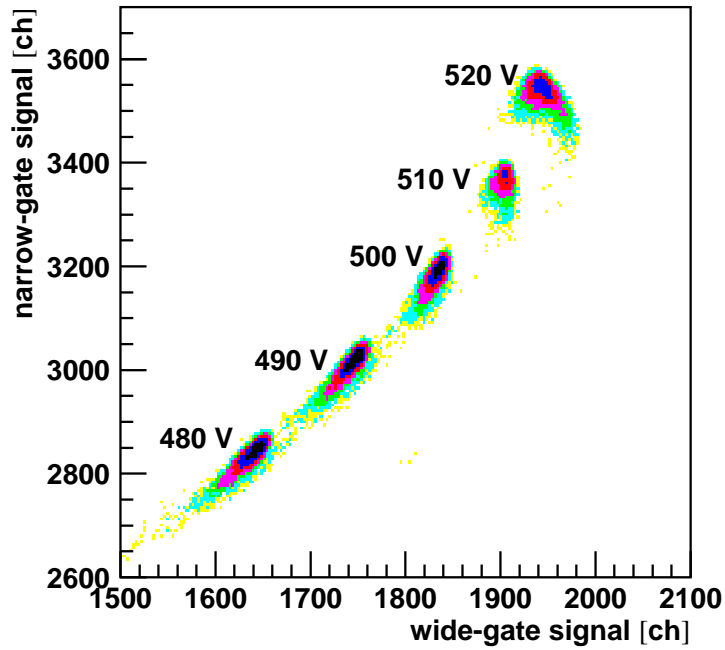


Figure 3.9: The narrow-gate QDC signal vs. the wide-gate signal for elastically scattered  $^{20}\text{Ne}$  on a gold target for five different high-voltage settings in one particular HI module.

### 3.3.2 High-voltage dependence and tube saturation

The dependence of the PMT gain on the applied high voltage has been investigated in order to find the appropriate HV settings and avoid possible signal distortions.

A single HI module covers a narrow rigidity range in the focal plane and therefore all particles coming from the target and hitting the detector will have approximately the same kinetic energy. This leads to peak structures in wide- and narrow-gate QDC spectra. The wide-gate signal refers to the total light output from both scintillator components whereas the narrow-gate integrates only the early part of the signal and thus it contains the complete contribution of the fast plastic component and a partial one of the slow CsI(Tl) scintillator light output.

In Fig. 3.9 a two-dimensional spectrum of the wide- versus narrow-gate QDC integration is shown for 5 different HV values. The data are taken from an elastic scattering  $^{20}\text{Ne}(^{197}\text{Au}, ^{197}\text{Au})^{20}\text{Ne}$  experiment at a beam energy of 14.3 AMeV with the BBS opening window at  $14^\circ$ . The kinetic energy of a  $^{20}\text{Ne}$  impinging on the detector and corrected for the energy loss in the target and the BBS window is equal to 283 MeV.

With the increase of the HV, a non-linear increase of the wide-gate signal compared to the narrow-gate signal is observed. This indicates a signal distortion due to a PMT saturation. In the data taking runs with pionic-fusion reactions the high voltage for each detector is kept in the linear region for kinematically allowed particle energies.

## 3.4 Photon detection system

The Plastic Ball has been used previously for photon detection [76, 77] although its primary purpose was the light-ion detection in relativistic heavy-ion reactions [70]. Its main advantage is the high granularity and the large solid angle coverage (Fig. 3.10). However, it was shown that it has a poor efficiency and resolution for photons, so in this setup an active photon converter was introduced. The Inner Shell covers only part of the solid angle of

CHAPTER 3. EXPERIMENTAL SETUP

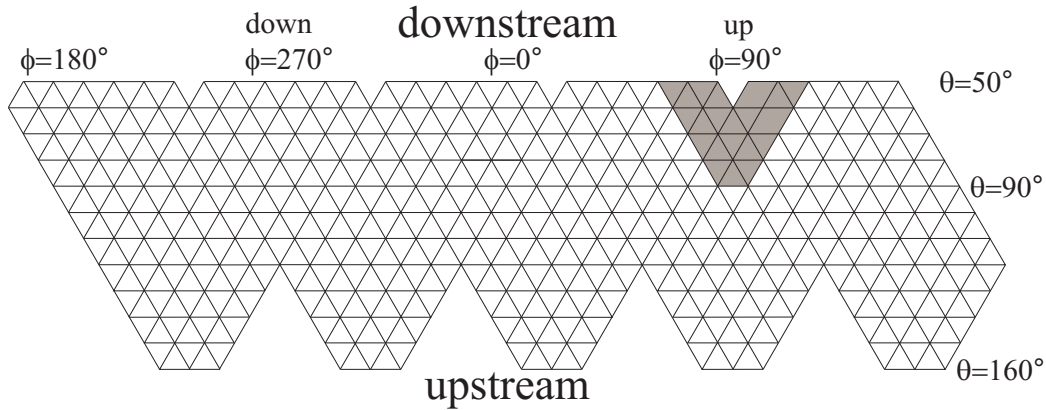


Figure 3.10: Mercator projection of the geometrical arrangement of the Plastic Ball phoswich modules. The grey area is kept clear for the target equipment.

the Plastic Ball so that one of the two back-to-back emitted photons may go directly to the PB.

In Fig. 3.11 a PB module is shown. It is a phoswich detector that consists of a thick 34 cm plastic BC-408 scintillator and a thin 4 mm  $\text{CaF}_2$  crystal glued onto the plastic. On the other side of the plastic scintillator a photomultiplier tube is attached with a base for the HV supply and signal readout. The shape of an individual module is a tapered prism. A ball structure is configured out of those modules. Each module has an opening of roughly  $10^\circ$ , and the total assembly covers laboratory polar angles from  $50^\circ$  to  $160^\circ$  in the full azimuth except for an opening for the target system. The detectors were powered by a Lecroy 1440 high-voltage system managed by a software on a PC accessible via network connection.

In order to increase the weak efficiency of the Plastic Ball detectors for gamma detection, the Inner Shell detector is inserted into the cavity inside the Plastic Ball. It consists of 64 modules like one shown in Fig. 3.12 (upper left).

Each module contains a 5 cm thick  $\text{CsI(Tl)}$  scintillating crystal. Since there is not much room left between IS modules and the PB, very small photomultiplier tubes (Hamamatsu R7400) were used for the signal readout.

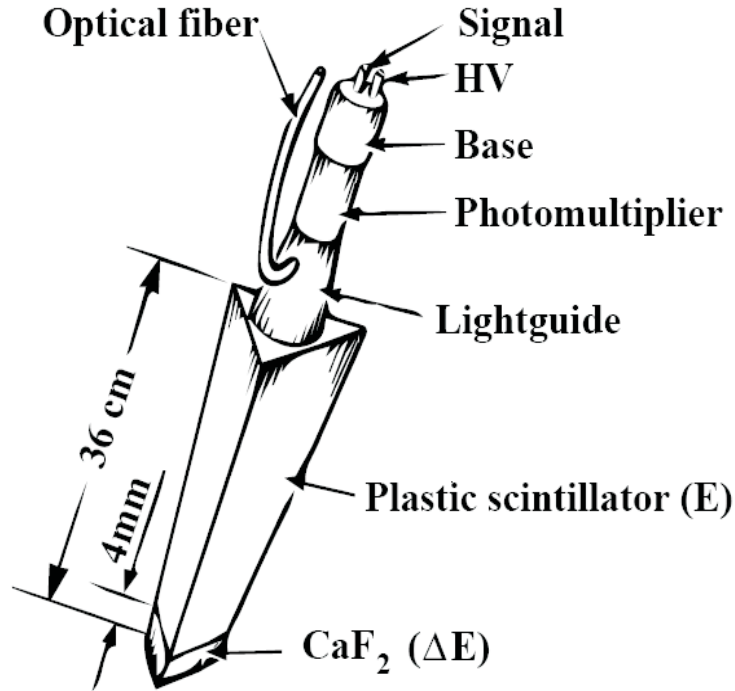


Figure 3.11: Drawing of a Plastic Ball phoswich module.

They were powered by the Lecroy 1440 supply like the PB detectors. The CsI(Tl) crystals come in 4 different shapes of pentagonal or hexagonal cross section and are fit together like in Fig 3.12 (top right) to form a shell that covers polar angles from  $90^\circ$  to  $150^\circ$ . Each of the IS modules is placed in front of several PB modules (seen from the target position, Fig. 3.12 bottom left). Therefore, there is an angular correlation between the signals in the IS and PB detectors for a particle passing through both detectors.

A determination of the angles of emitted photons is crucial for the reconstruction of the reaction kinematics. From GEANT3 [78] simulation the resolution of determining the polar and azimuthal angle can be obtained (Fig. 3.13). The resolution is the FWHM of the distribution of the difference between thrown and reconstructed angles and equals  $6^\circ$  and  $9^\circ$ , respectively. The simulated data are analyzed with the same analysis tools as used for the measured data.

### CHAPTER 3. EXPERIMENTAL SETUP

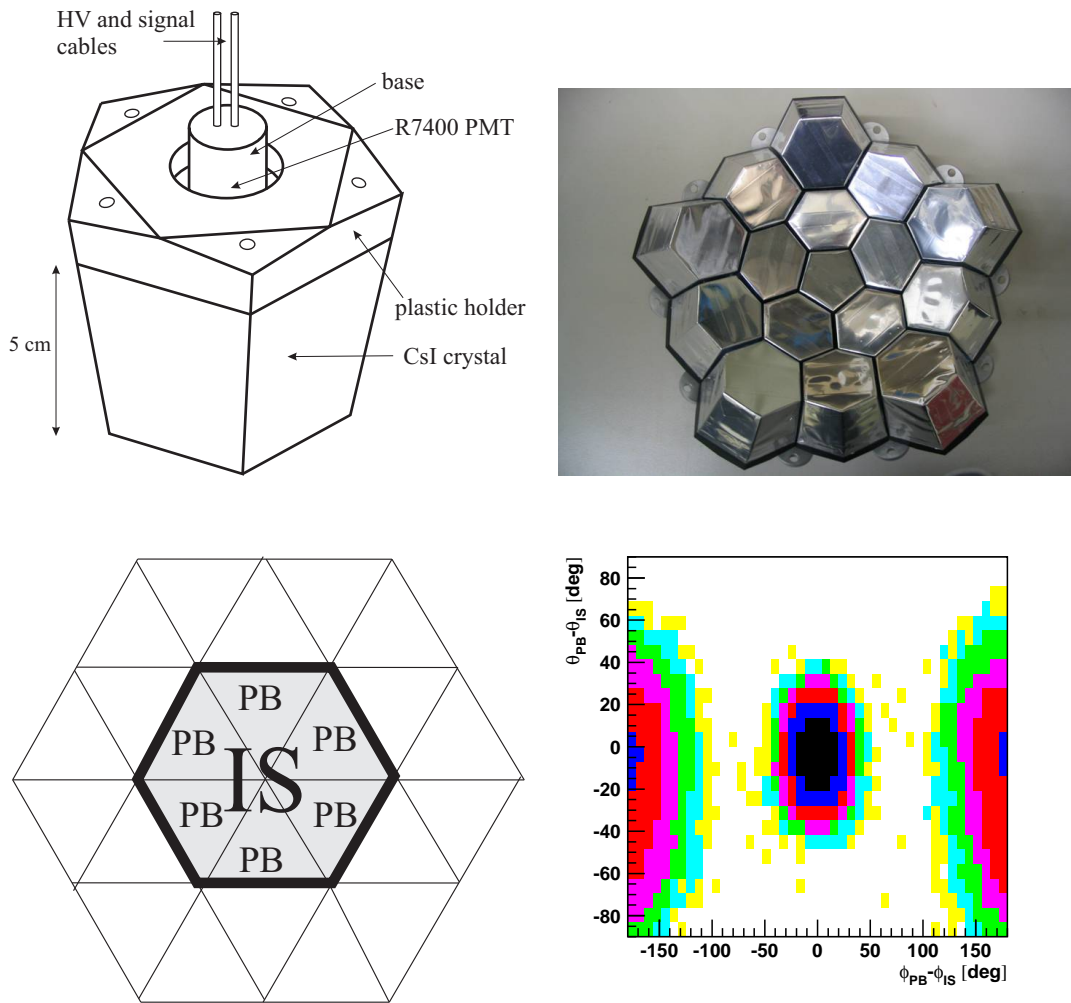


Figure 3.12: A drawing of an Inner Shell detector module is shown in the top left. Four different types of modules are arranged in a spherical shell (top right). One IS module shadows several PB modules as shown in the lower left panel. Particles that pass through the IS and PB detectors produce signals in detectors at approximately the same angles as shown in the lower right panel for signals obtained with cosmic muons.

In Fig. 3.14 an increase of the efficiency and an improvement in the photon energy measurements is seen for a setup which uses both detectors. As previously mentioned, the Plastic Ball was originally used for the detection and identification of light charged particles. Several years ago it has been used in the KVI bremsstrahlung project as a photon and lepton detector. In

### CHAPTER 3. EXPERIMENTAL SETUP

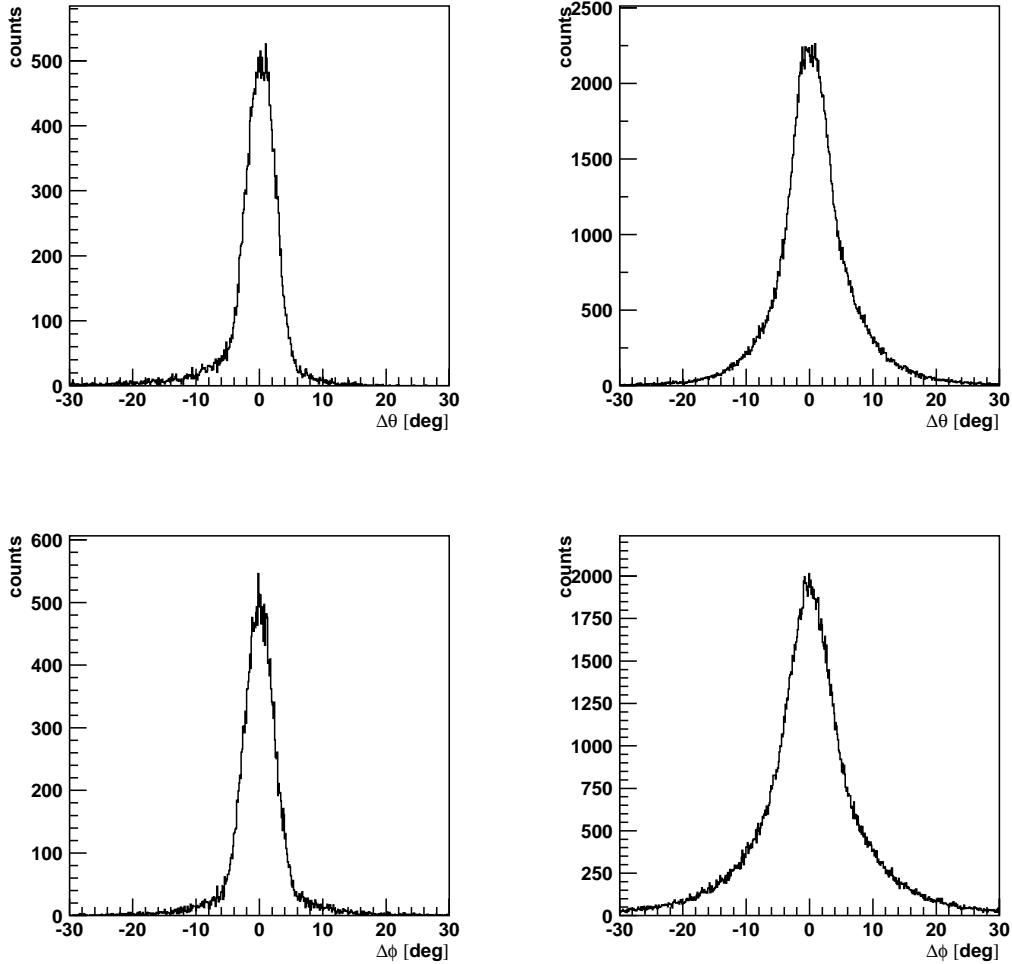


Figure 3.13: The distributions of the differences between thrown and reconstructed photon angles obtained from GEANT simulations. In the forward direction the polar and azimuthal angles (upper and lower left, respectively) are better determined (FWHM=6°) than in the backward direction (upper and lower right) where showers are produced in the IS detector (FWHM=9°).

order to improve the efficiency for photon detection a passive lead converter shell was used in some experiments. On the other hand, the shell worsened the energy resolution. Therefore, a new more sophisticated solution was needed to improve the photon-detection performance of the Plastic Ball. A new active inner shell converter has been developed. The efficiency increased

### CHAPTER 3. EXPERIMENTAL SETUP

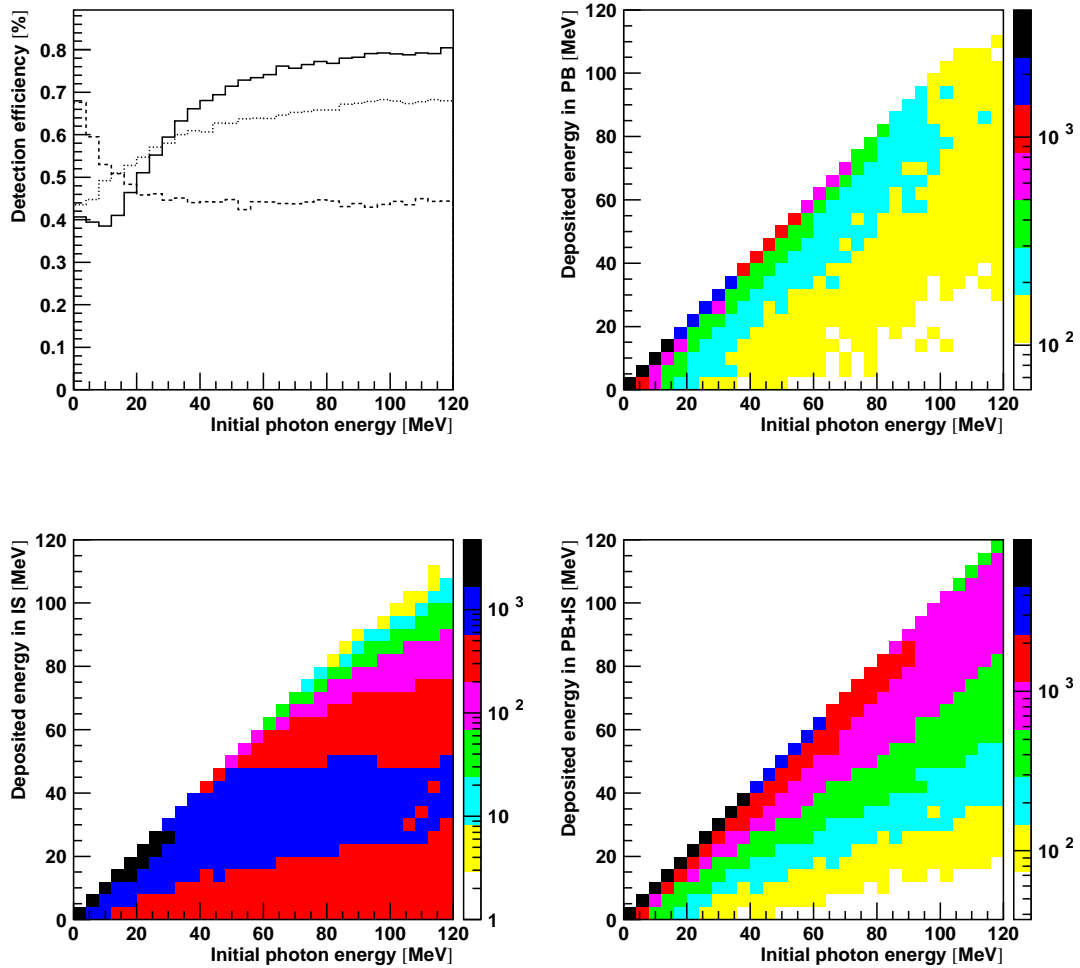


Figure 3.14: Plastic Ball and Inner Shell detection efficiencies for photons as a function of the photon energy (upper left). The solid histogram represents the efficiency of the full setup of both detectors, the dashed line is for the PB alone and the dotted line is for the IS alone. The other plots show the photon energy deposition in the PB alone (upper right), the IS alone (lower left) and in both detectors (lower right) versus the initial energy of the photon.

from roughly 45% to 70%.

### 3.4.1 Plastic Ball and Inner Shell electronics

The Plastic Ball and the Inner Shell detector signals were processed by identical electronics modules in almost the same fashion. The only difference was that delayed IS analog signals were not digitized with different gate

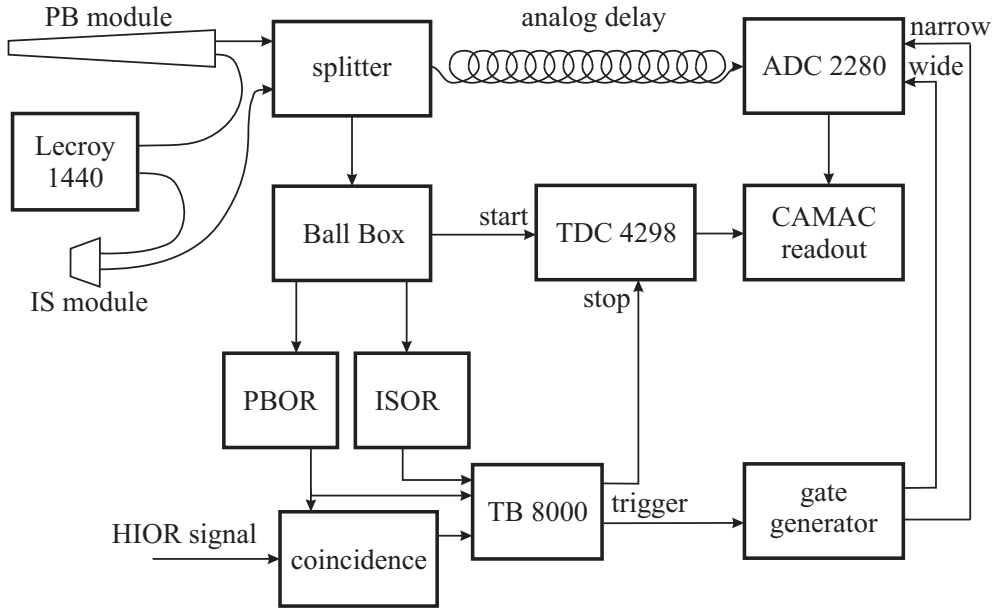


Figure 3.15: The PB and IS detector electronic readout scheme. Analogously to the HIOR and PBOR signals, the ISOR signal is derived from logic OR of all output discriminator signals of the IS detectors.

widths. A detector signal from a PMT is split by a passive splitter that sends one copy into a discriminator and another through delay lines to an ADC module. The 8-channel discriminator modules are packed in crates, so-called Ball Boxes. Each of the Ball Boxes houses 18 discriminator modules. One discriminator module produces one logic multiplicity output signal for triggering purposes and individual logic signals for the TDC start. The multiplicity output signals from the Ball Boxes are ORed and used as a single trigger or together with HI signals as a coincidence trigger. The PB analog signals are split once more before the digitization in ADCs using a short and a long integration gate. The 48-channel Lecroy 2282 ADC modules were arranged in two CAMAC crates with a Lecroy 2280 ADC controller each. The



## CHAPTER 3. EXPERIMENTAL SETUP

ADC controller reads all ADCs in the crate via an auxiliary bus, subtracts PEDESTALS, compresses the data and delivers it to a CAMAC CC A2 controller. The wide and narrow gates produced by gate generators are fed into separate ADC controllers. For the time measurement one separate CAMAC crate was used. It contains a TDC controller (Lecroy 4298) together with 22 32-channel Lecroy 4291 TDC modules in a separate CAMAC crate. The TDC controller was interfaced via a Lecroy DATABUS 4299 module to the CAMAC controller.

### 3.5 The data acquisition

All detectors were read out by CAMAC electronics controlled by a VME-based computer.

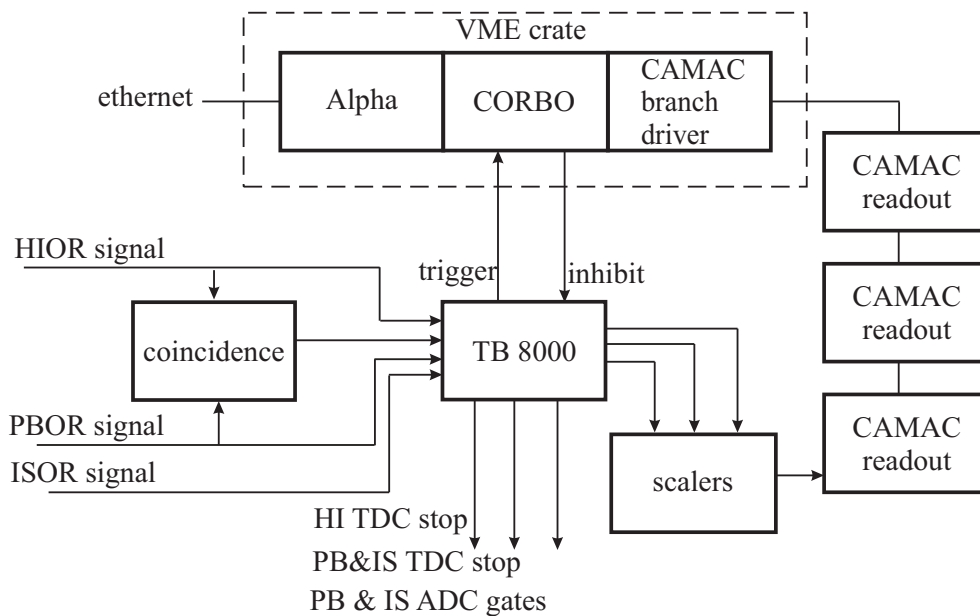


Figure 3.16: The schematic layout of the DAQ system.

The data acquisition in this experiment was based on a VME system, encompassing a computer accessible via ethernet, a trigger module CORBO RCB 8047 and a CAMAC CBD 8210 branch driver communicating with

## CHAPTER 3. EXPERIMENTAL SETUP

four chained CAMAC controllers. The basic software used for running the acquisition was developed at the KVI by Zwarts [79].

### 3.5.1 The trigger

A few signals are used to trigger the data acquisition. The most important one is produced by a coincidence of the OR signal from the backward PB detectors (PBOR) and the OR signal from all HI detectors (HIOR). Apart from the coincidence signal, down-scaled singles trigger signals from each detector (PBOR, HIOR and ISOR) are used for monitoring and diagnostic purposes.

The timeline of producing a coincidence between the two OR signals is shown in Fig. 3.17. The PB signal is made narrow and falls within the wider signal from the HI detector. Therefore, the PB signal always determines the trigger timing and thus the HI TDC time is measured relative to the PB time.

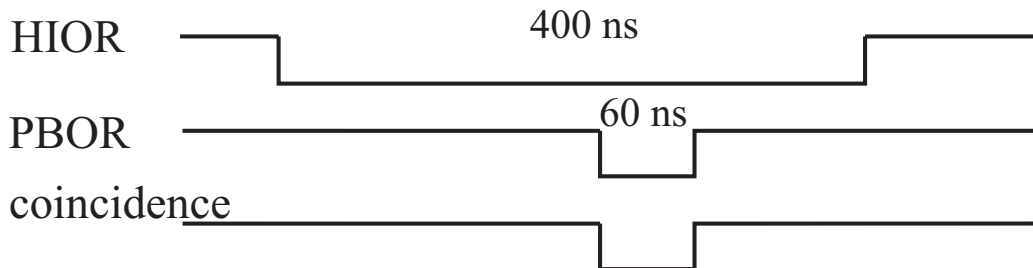


Figure 3.17: The timing scheme of the coincidence trigger.

Some possible time relations are shown in Fig. 3.18. The relative timing is shown for the case, when a HI signal is produced later than the PB signal, which is the usual situation for particles from a true reaction in the target (the ion needs some time to reach the focal plane). In this special case the HI signal defines the trigger. It produces a self-triggering peak in the HI TDC spectrum. Also the case is shown in which a HI signal is made before the PB signal. This situation is caused by particles from a previous reaction.

The forward PB detectors are flooded by particles not stopped in the

## CHAPTER 3. EXPERIMENTAL SETUP

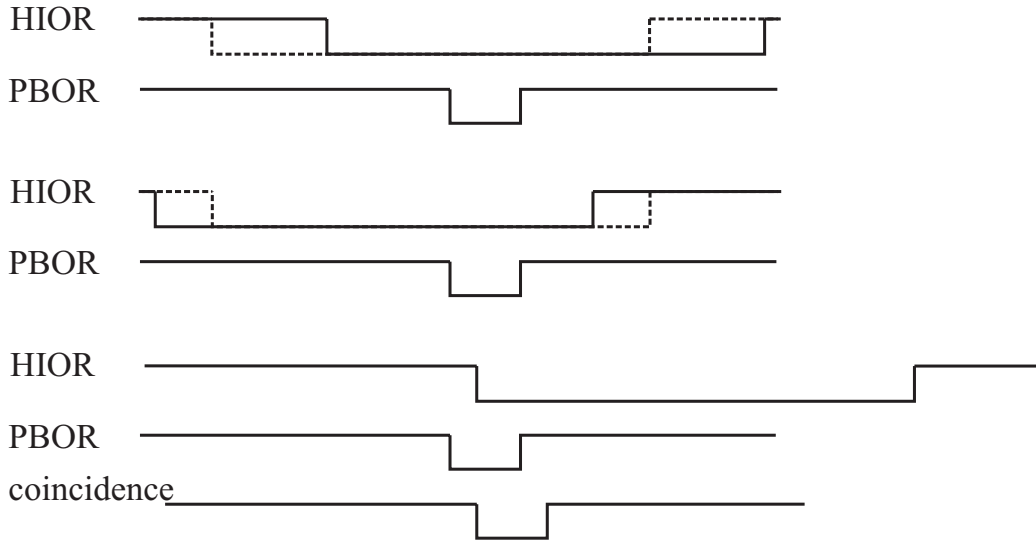


Figure 3.18: Several different relative timings of HI and PB signal. The upper and middle time lines show HI signals from an earlier and a later time, respectively. The lower time line shows a special case, when a very late HI signal defines the reference time. It produces a sharp self-triggering peak in the HI TDC spectra.

Inner Shell with high counting rate exhausting the DAQ system capability. By excluding them from the main trigger the trigger rate drops to acceptable 10000 Hz.

### 3.5.2 The scalers

Approximately every second a scaler event is written together with the trigger events. The scaler data is read from a CAMAC scaler module. The module counted the number of different trigger signals before and after dead time and also after down-scaling. It gives information about the count rates of the detector signals and therefore about the dead time of the DAQ system. In addition, one channel has been used for the beam current measurement after digitization of the amount of charge collected in the Faraday cup. Also, the scaler output has been monitored during the data taking.

The beam current is measured by counting the digitized charge in a time

CHAPTER 3. EXPERIMENTAL SETUP

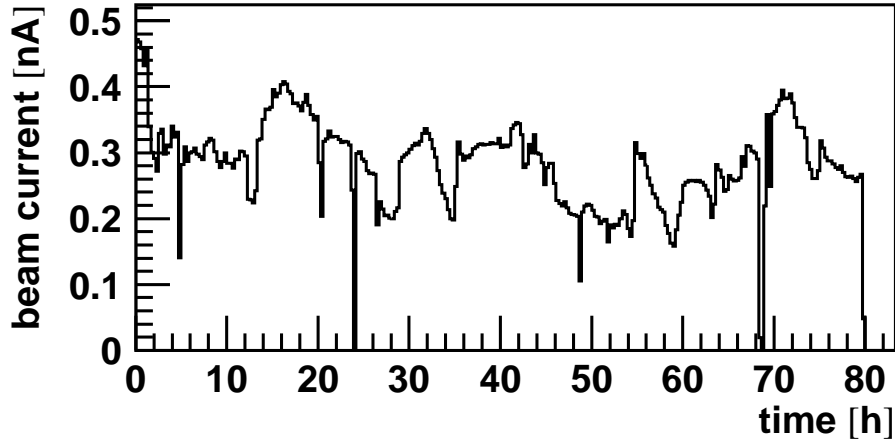


Figure 3.19: The time dependence of the beam current during the whole experiment, averaged in 1000 s time intervals.

window of one second. The digitizer was calibrated so that the obtained values were in units of 0.1 nA. Since the readout introduced value jumps up to 30%, the current values were averaged over a longer time (1000 s) and are shown in Fig. 3.19. The variations in the beam current are a consequence of the bad resolution of the beam monitor, which does not allow to fine-tune the actual beam current during the experiment.

Table 3.2: Count rates of signals in the experiment.

signal	raw	inhibited	reduction factor	accepted
HI OR	23 kHz	3 kHz	$2^7$	23 Hz
PB OR	200 kHz	26 kHz	$2^{15}$	1 Hz
IS OR	100 kHz	13 kHz	$2^{10}$	13 Hz
$M_{PB} \geq 2$	900 kHz	120 kHz	$2^{13}$	15 Hz
COINC	1.8 kHz	230 Hz	$2^0$	230 Hz

The dead-time of the data-acquisition system needed to process an accepted event was equal to  $3 \mu\text{s}$  per event. With the average load of the system only 13 % of detected events were accepted. Most of the coincidence

### *CHAPTER 3. EXPERIMENTAL SETUP*

trigger events were random coincidences of the HI and PB signals within the coincidence window. Because of a huge count rate in the forward part of the PB detector ( $\approx 2$  MHz) the coincidence trigger only included the signals from the backward PB detectors. The backward detectors are placed behind the IS detector which prevents charged particles to hit the PB detector.

## Chapter 4

# Simulation of the pionic-fusion reaction

A proper experimental study of nuclear reactions with a complex detector system is almost impossible without simulations. They are necessary in all phases of the work from the construction of detectors and building of an experimental setup, over the calibration and the data analysis to the interpretation of the observables in terms of the underlying physics mechanisms. In Fig. 4.1 a diagram of all simulation steps is shown.

The event generator GENBOD [80] is employed to calculate the kinematics of the final state of the reaction. The total energy in the center-of-mass frame and the masses of outgoing particles are needed as input. GENBOD produces particle momenta consistent with the energy and momentum conservation laws and the phase-space weight factor. The weight factor for the two-body final state is trivial since all directions in the center-of-mass system are equally probable. The result is an isotropic phase-space distribution in the center-of-mass system. The particles are then boosted to the laboratory system. This can be used for studying the constraints imposed by the conservation laws or pure kinematics.

Realistic distributions of the generated events which reflect the properties of the underlying physical processes are obtained by adding a weight to each event depending on its kinematics. The weight is given by the transition

## CHAPTER 4. SIMULATION OF THE PIONIC-FUSION REACTION

probability or the cross section predicted by a certain physical model. This can be easily done since the kinematics is determined by only one kinematical variable and therefore the cross section depends on one variable only.

The response of the detectors is simulated by the detector simulation package GEANT3 [78]. The response is examined both individually for a single detector and a single particle track as well as for complete events and the entire detection system.

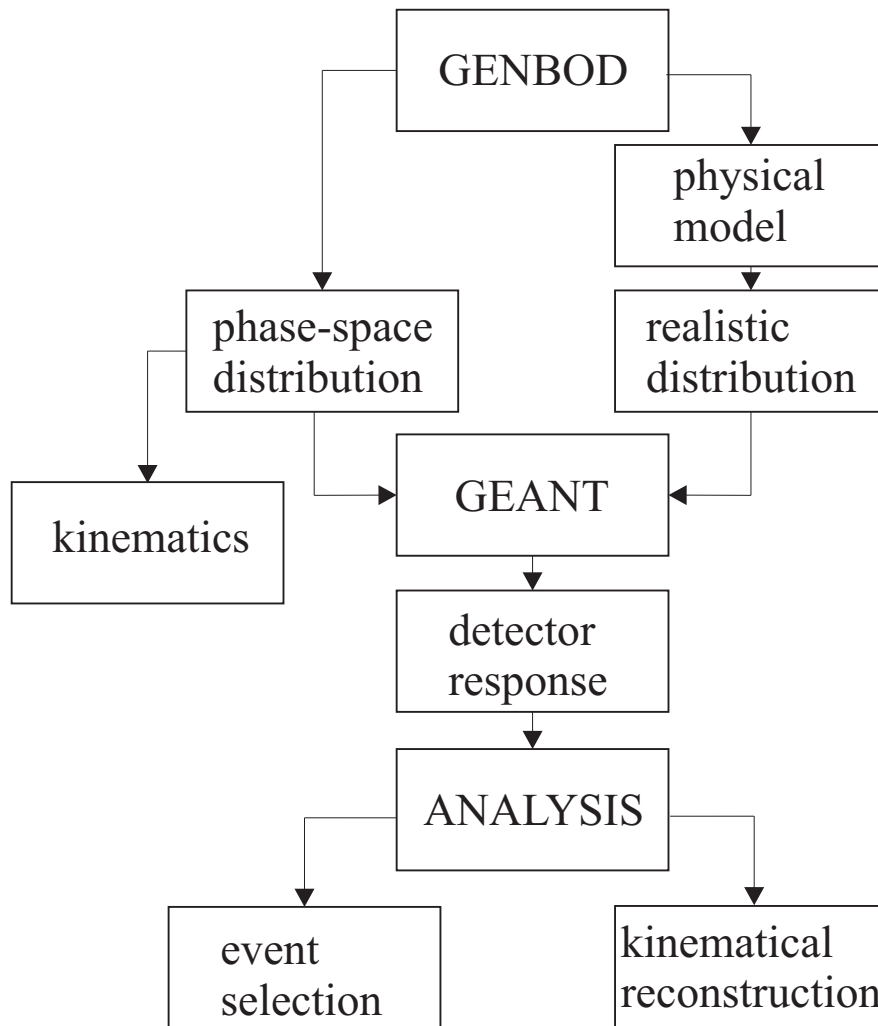


Figure 4.1: The flow diagram of the simulation procedure used in the analysis of pionic-fusion reactions.

CHAPTER 4. SIMULATION OF THE PIONIC-FUSION REACTION

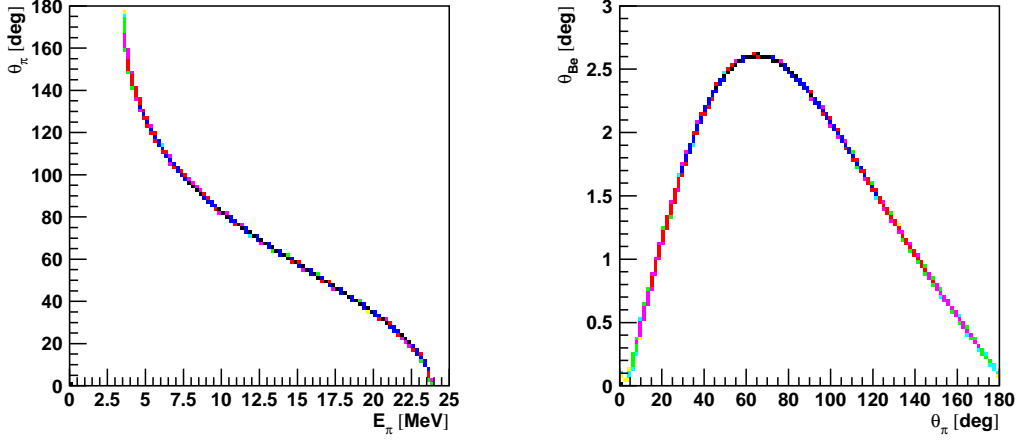


Figure 4.2: Left: Kinematics of the pion in the laboratory frame. Right: The polar angle of  ${}^7\text{Be}$  as a function of the polar angle of the pion.

The energy of the emitted neutral pion versus the pion angle is shown in Fig. 4.2 in the laboratory system for the reaction  ${}^4\text{He}({}^3\text{He},\pi^0){}^7\text{Be}$  at 258 MeV  ${}^3\text{He}$  beam energy. In the center-of-mass system the pion has fixed kinetic energy for any emission angle whereas its kinetic energy in the laboratory system depends on the emission angle. This is a one-to-one correspondence unlike the correspondence for  ${}^7\text{Be}$  where two different kinematic solutions are possible for the same polar angle (Fig. 4.3).

The photon acceptance of the PB detector is shown in Fig. 4.4. All generated events cover the full solid angle range and are shown in the upper plot. Some photons are emitted in the PB and can be detected. Their angular distribution is shown in the middle plot. For a complete event selection and reconstruction, detection of both photons is needed. This condition reduces the amount of photons and their distribution is shown in the lower plot.

The photons are emitted back-to-back in the pion center-of-mass system. The simulation provides the opening angle distribution shown in Fig. 4.5. Since the pion is slow in the laboratory frame, the opening angle between the photons will be large. That will be an important signature of the pionic-fusion events in the analysis.

One of the largest deficiencies of the experiment was the thick liquid-



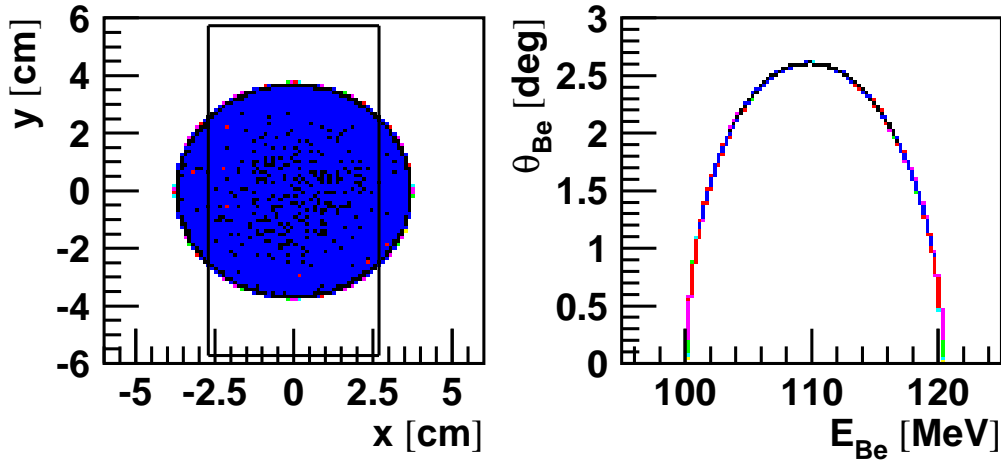


Figure 4.3: Kinematics of the  ${}^7\text{Be}$  fusion product. Left: Hit positions of particles at the BBS entrance window. The rectangle represents the BBS window. Right: The polar angle as function of the kinetic energy of  ${}^7\text{Be}$  fusion products.

helium target. The energy loss of the  ${}^7\text{Be}$  was huge and the information about the kinetic energy is lost. So it could not be used in the kinematical reconstruction of events. On the other hand, the acceptance of the setup for  ${}^7\text{Be}$  is lowered and has to be estimated in order to obtain the cross section.

Because of that the target material is introduced in the GEANT simulation and it is supposed that the reaction takes place along the beam line at different positions within the liquid helium. Depending on the path length of beryllium ions through the target their energy will vary and the position at the focal plane of the BBS will consequently change. If the energy is too low to be accepted by the detector, the event will not be recorded. In Fig. 4.6 it is shown that particles produced in the second half (downstream 0.5 cm) of the target can reach the HI detector. In the left panel of Fig. 4.6 the upper edge of the band corresponds to a high-energy  ${}^7\text{Be}$  (120 MeV) and the lower edge to a low-energy  ${}^7\text{Be}$  (100 MeV). In the right panel at the upper edge there are particles produced at the end of the target, and particles produced in the middle of the target (at 0.5 cm) are associated to the lowest output

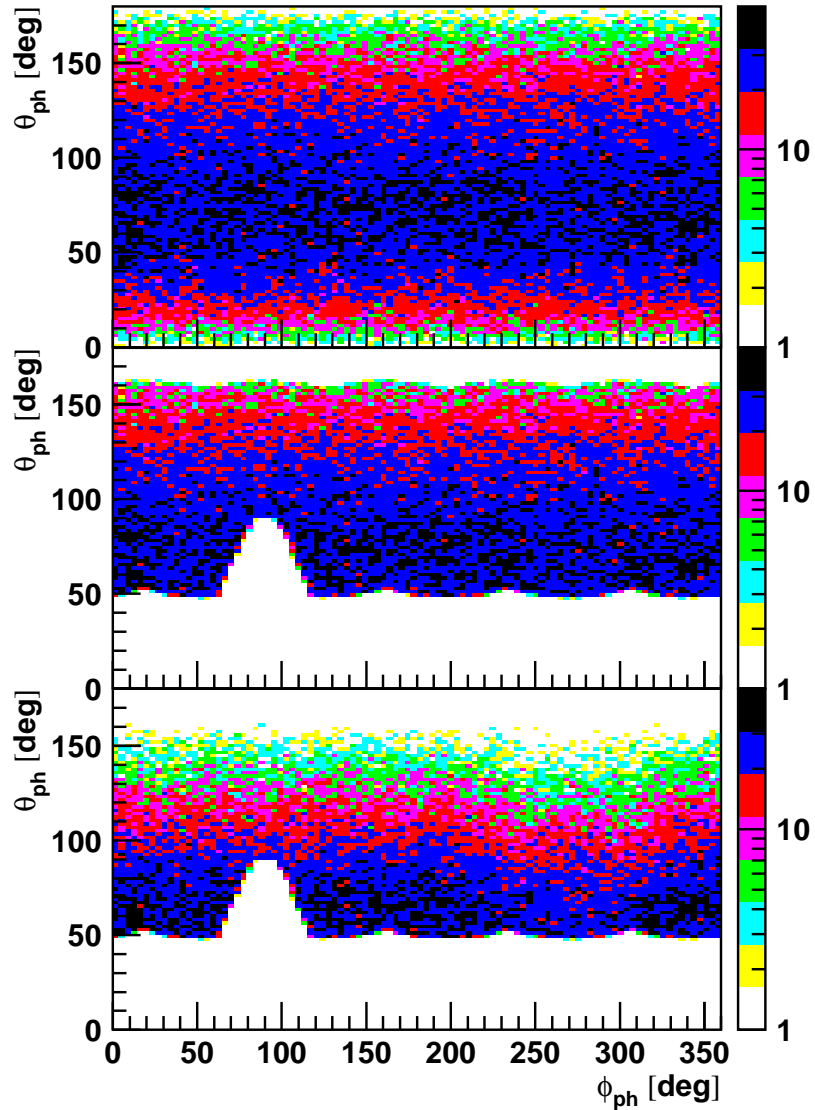


Figure 4.4: The geometrical acceptance for photons is shown as a function of the laboratory polar and azimuthal angle under different conditions. Top: The original photon spatial distribution. Middle: Photons emitted into the geometry of the PB. Bottom: Filled with photons only when both photons in an event are emitted into the geometry of the PB.

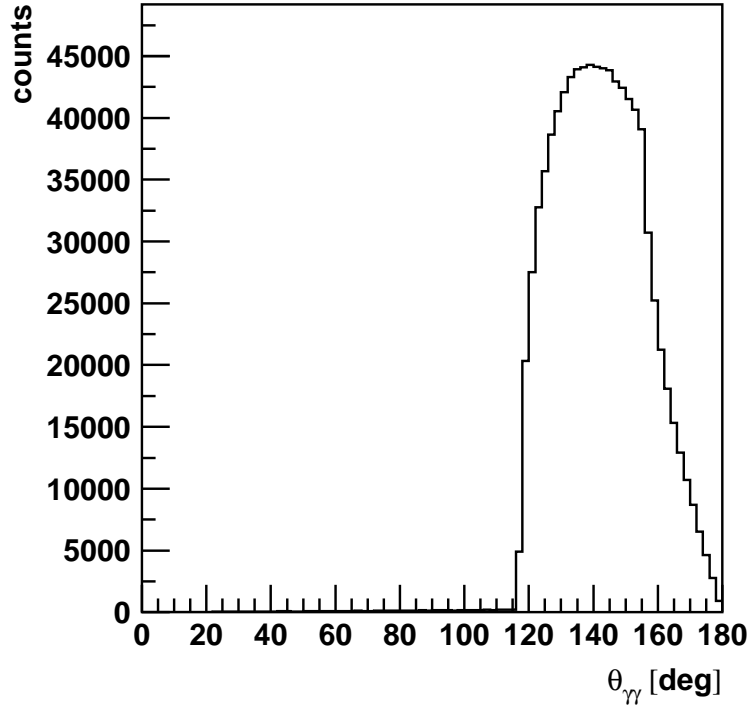


Figure 4.5: The photon opening angle distribution.

energies.

When a photon passes through the Plastic Ball detector an electromagnetic shower is produced and the signal appears in several neighboring detectors. All those signals are summed and considered as they originate from a single photon. In this way two-photon events with a small opening angle (less than  $15^\circ$ ) between photons are misidentified as one-photon events with the photon of higher energy. This is not a problem since photons coming from a pion decay have a much larger opening angle. Fig. 4.7 shows the appearance of correlated photon tracks at small opening angle. This is due to the discontinuous electromagnetic showers and a signal of one photon only is interpreted as a two-track signal. One of these two tracks has a very small energy deposition as can be seen from the dashed line corresponding

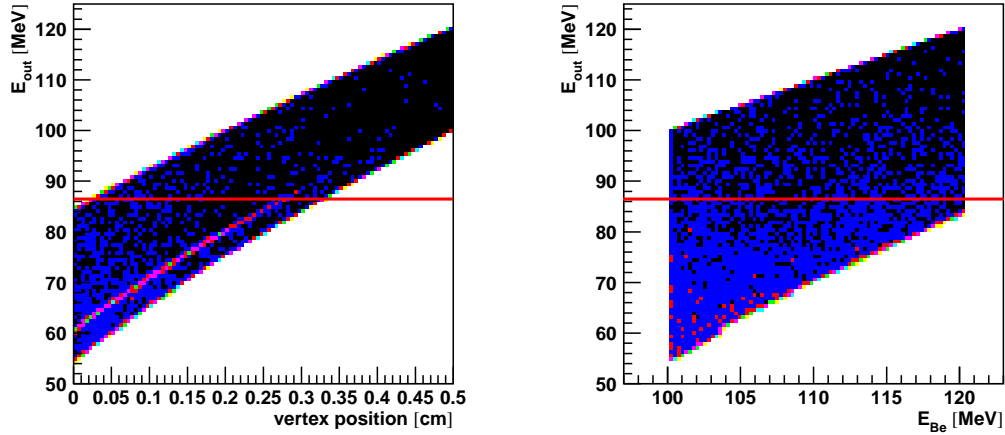


Figure 4.6: The energy of  ${}^7\text{Be}$  leaving the target and entering the BBS versus the original energy of the  ${}^7\text{Be}$  in the moment of creation (left). Red line shows the limit of the acceptance (86.5 MeV) of the HI detector after the BBS magnets.

to tracks with energy deposition above 5 MeV. Therefore, the signals from further neighboring detectors need to be clustered together into one photon track. Apart from decreasing the false two-photon events, this procedure improves the energy measurement.

## 4.1 Implementation of the theoretical predictions

A physical-model distribution is obtained by accepting the events generated by GENBOD according to the predicted cross section. Because of the two-body kinematics, the distribution depends only on one variable so the generation of the model distribution is trivial.

The GENBOD event generator produces events distributed according to the phase space. This means that for every direction in space an equal number of events is produced in an equal solid angle range. The polar-angle distribution has a sine shape. The model distribution is obtained by rejecting

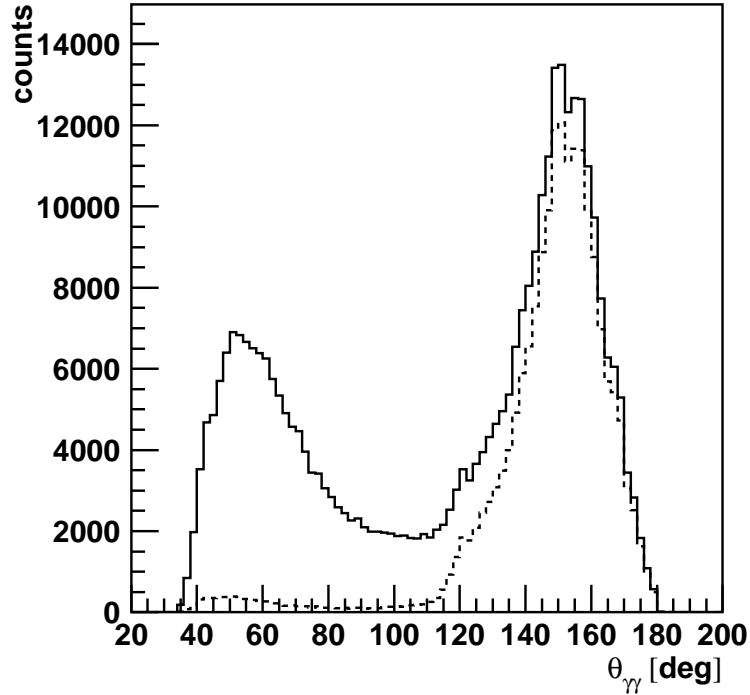


Figure 4.7: The photon opening angle distribution after tracking and clustering (solid line). The dashed line shows the distribution for photons with an energy deposition greater than 5 MeV.

more or less events produced by GENBOD depending on the predicted cross section. The predicted cross section is obtained by a digitization of the plot from the theoretical papers.

The generator produces momenta of particles in the final state satisfying energy and momentum conservation. The phase space weight is also calculated but in our particular case of a two-body final state it is trivially equal to 1. The phase-space distribution is shown in Fig. 4.8 on the left. The model distribution [67] is shown on the right.

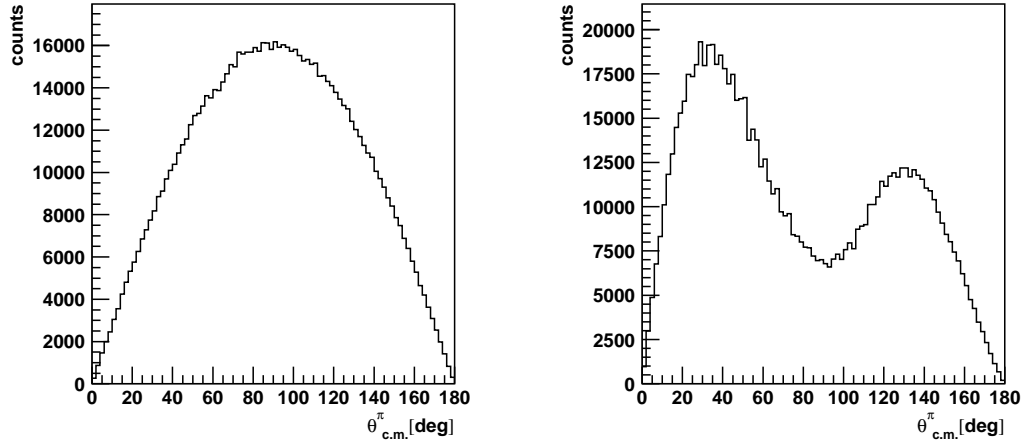


Figure 4.8: The event distribution as a function of pion polar angle in the center-of-mass system. The event is fully determined by the pion polar angle. Left: The phase-space distribution. Right: The model distribution calculated by Kajino et al. [67].

## 4.2 Detector acceptance

In a three-body final state five kinematical variables are needed to reconstruct an event. The four photon angles  $\theta_1$ ,  $\phi_1$ ,  $\theta_2$  and  $\phi_2$  are measured in this experiment with a resolution of  $3^\circ$  for forward PB detectors and  $5^\circ$  for backward PB and IS detectors. These values are obtained from a GEANT simulation.

There are several constraints which limit the acceptance of the detector setup. First, there is a limited geometry of both HI detector and photon detectors. As can be seen from Fig. 4.3 the opening of the BBS limits a part of the azimuthal angle of  $^7\text{Be}$  ions emitted at highest polar angles. The geometry of the PB and IS detectors lowers the acceptance of photon pairs as shown in Fig. 4.9. As a consequence, the pions emitted at the forward polar angles are not detected.

## CHAPTER 4. SIMULATION OF THE PIONIC-FUSION REACTION

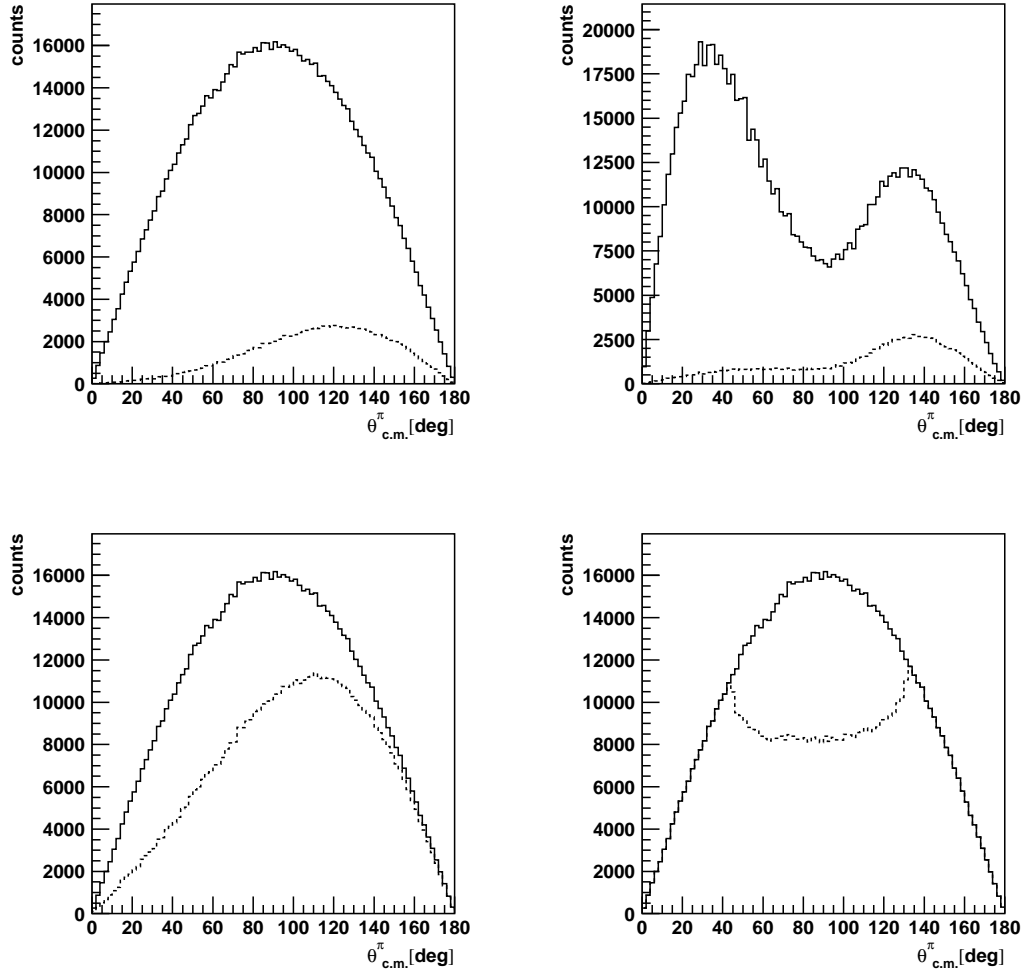


Figure 4.9: Influence of different experimental constraints on the original distributions. Top row: Comparison of the phase-space (left) and the model (right) distributions without (solid line) any selection and with (dotted line) the selection of the events in which the energy deposition for each of the two photons is higher than 5 MeV. Bottom row: Similar phase-space distributions for  ${}^7\text{Be}$  ions which, after passing through the target, either have sufficient energy to be detected at the focal plane (left dotted line) or are passing the BBS opening (right dotted line).

### 4.3 Kinematical reconstruction

The last problem which is addressed with the simulations is the kinematical reconstruction of the event from the measured variables. Since the measured

## CHAPTER 4. SIMULATION OF THE PIONIC-FUSION REACTION

variables contain a certain error due to the detector resolution, the determined kinematics, i.e. the pion center-of-mass angle in this case, will have errors, too. Therefore, the obtained distribution will be different from the real one and simulations help in relating these two distributions. In Fig. 4.10

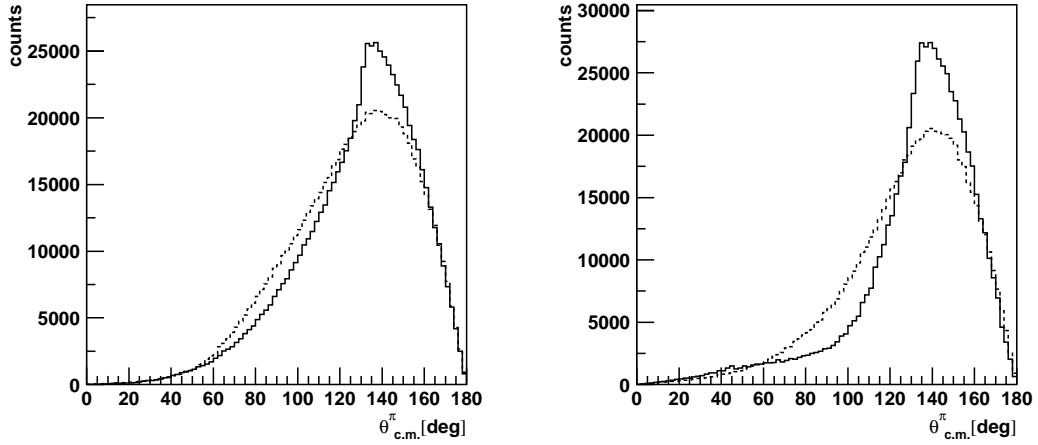


Figure 4.10: Polar angle phase-space (left) and model [67] (right) distributions for neutral pions in the center-of-mass system: the original distributions with experimental constraints (solid line) and the ones obtained by applying the data analysis procedure to the simulated data (dotted line).

the difference between the original distribution and the reconstructed one is shown. The kinematics of events that passed all cuts imposed by the experimental setup and the data analysis, has to be determined. The details will be given in Ch. 5.



## Chapter 5

### Data analysis

A multi-detector experimental setup such as that described in Ch. 3 enables measurements of reactions with very low cross sections. This is achieved during the data acquisition by taking events with coincident signals in different detectors but also in the offline analysis which reduces background almost completely. A coincidence of the HI detector and the backward PB hemisphere is necessary because the forward part is flooded by charged particles (mostly protons) and the count rate of such random and unwanted coincidences is too big. In this experiment the reconstruction of events relied on the measured angles and less on the measured energies. The reason for that lies in the poor resolution of the large-acceptance photon detection system and the thick target in which a huge amount of heavy-ion energy is lost. Therefore, for the reconstruction of events simulations and assumptions were applied.

#### 5.1 Calibration

##### 5.1.1 Heavy-Ion detector

The Heavy-Ion detector is primarily used for the identification of charged particles emerging from the target. Although the energy and momentum of these particles can be measured, it does not help in the kinematical reconstruction of the event because of the huge energy loss in the thick liquid

## CHAPTER 5. DATA ANALYSIS

helium target. The measured energy and momentum of a detected particle are not equal to energy and momentum at production time. Therefore, they cannot be used together with photon kinematical variables to reconstruct the full kinematics of the reaction.

A few test experiments were conducted with beams of certain particles at well defined energies. A detector response to the elastically scattered beam of  $^{19}\text{F}$  at 190 MeV, and  $^4\text{He}$ ,  $^{12}\text{C}$ ,  $^{16}\text{O}$  and  $^{20}\text{Ne}$  at 14.3 AMeV on 1 mg/cm<sup>2</sup> gold and carbon targets were studied.

### Momentum calibration

Elastically scattered particles emitted in a narrow angular range (66 mrad horizontal, 140 mrad vertical) have a well defined kinetic energy and this fact is used for the momentum calibration. The elastic scattering of different ions ( $^4\text{He}$ ,  $^{12}\text{C}$ ,  $^{16}\text{O}$ ,  $^{19}\text{F}$  and  $^{20}\text{Ne}$ ) with a kinetic energy of  $\sim 10$  AMeV on a heavy  $^{197}\text{Au}$  target is a dominant process. Consequently, the measured hit distribution in the HI detector with the BBS positioned at a scattering angle of  $14^\circ$  shows two main peaks at a rigidity associated with the elastically scattered particles in a narrow energy span in the upper and lower HI array (Fig. 5.1). The identical patterns in both upper and lower HI arrays can be seen. Analogous momentum distributions have been measured for several BBS magnetic-field settings. A correlation of the BBS central-ray rigidity deviation from the nominal one (associated with the elastic peak) with the mean peak positions is shown in Fig. 5.2. A good linearity with a slope of 0.646%/det (momentum deviation change per one detector width) is observed. From the width of the peaks in Fig. 5.1, an average momentum resolution of 1.1% FWHM is derived. The resolution is mainly due to the displacement of the HI detector relative to the focal-plane position. The effects of kinematical broadening and energy straggling in the target are in the order of 0.1%.

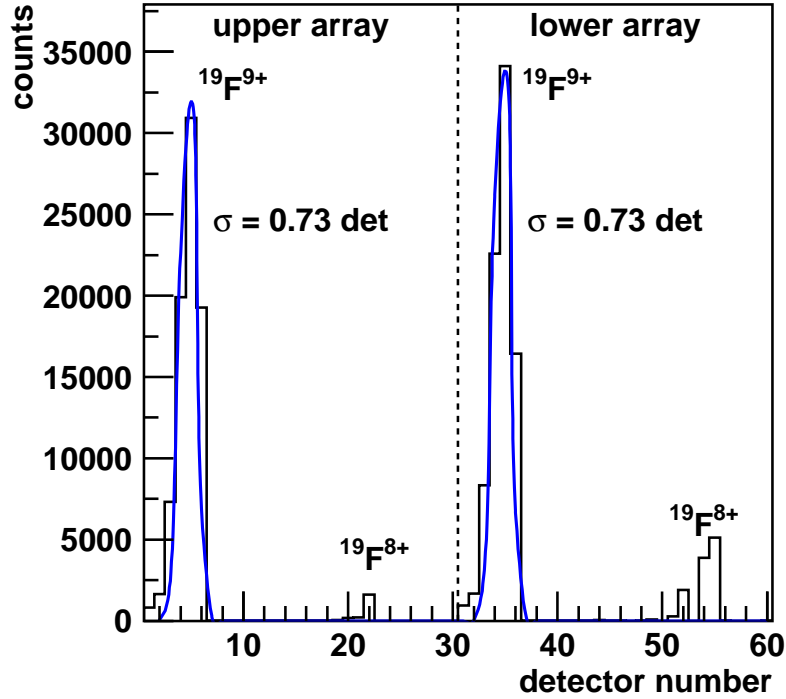


Figure 5.1: The hit distribution of 10 MeV  $^{19}\text{F}$  ions scattered on a gold target at  $\theta=14^\circ$  for -4% BBS central-ray momentum deviation from the elastic  $^{19}\text{F}$  rigidity. The two dominant peaks at the lower rigidity are fully stripped fluorine ions whereas the small peaks correspond to the 8+ charge state and therefore have a higher rigidity. In these peaks several channels are missing since a simpler DAQ system with only one CAMAC crate was used in the commissioning experiment.

### QDC calibration

A typical raw wide-gate QDC spectrum for the  $^3\text{He}+^4\text{He}$  reaction is shown in Fig. 5.3. The pedestals are measured and subtracted. The peaks that appear in the spectra are related to different ions with the energy in a narrow region corresponding to the narrow rigidity bin defined by the width of an individual HI detector module in the focal plane. The widths of the peaks are about

CHAPTER 5. DATA ANALYSIS

2 % FWHM.

The kinetic energies of the particles produced in the  ${}^3\text{He}+{}^4\text{He}$  collisions at the beam energy of 258 MeV and accepted by the BBS are not sufficient to punch through the detector. Therefore the energy deposition of an ion in the HI detector is equal to its kinetic energy. However, the QDC-spectra show distributions of integrated light signals (or a fraction of the signals for the narrow-gate integration) produced by the energy deposition in the scintillators. The relation between the light output and the energy deposition

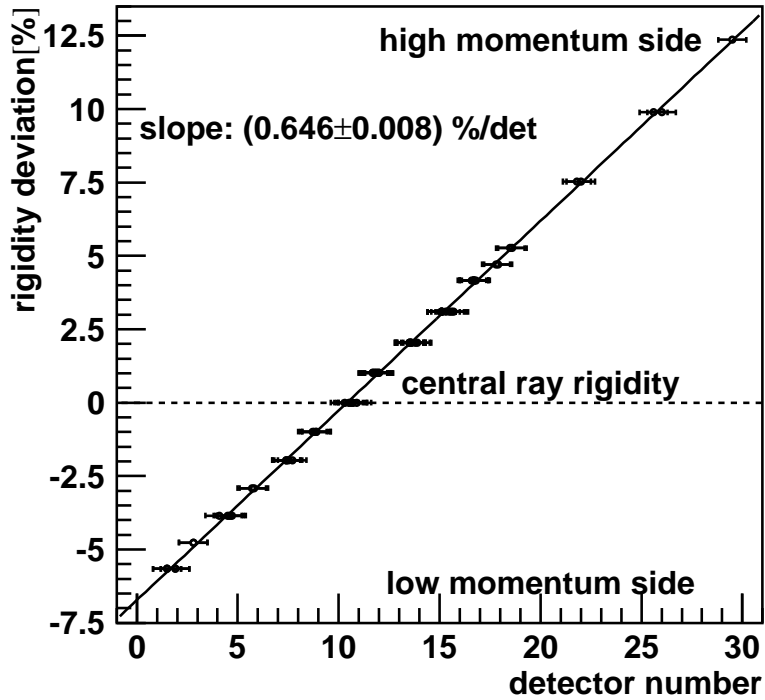


Figure 5.2: Measured elastic scattering peak position along the HI detector array as a function of the corresponding relative rigidity shift with respect to the central-ray rigidity. The average central-ray rigidity position is 10.4 detector units, i.e. near the high-momentum edge of the detector #10 and #40 in the upper and lower array, respectively.

## CHAPTER 5. DATA ANALYSIS

is not linear and depends on the particle type. This will be discussed in the following subsection. To obtain the kinetic energy of the particle from the measured signals would require a more involved analysis and more comprehensive commissioning measurements than the ones that could be done. However, this would not improve the analysis because of the large energy loss of the particles in the target. Namely, the kinetic energy of the particle at the detector is much less than the energy just after the reaction took place.

Instabilities in the energy gain have been observed for some detectors (see Fig. 5.4). It is known that the performance of the CsI(Tl) crystals

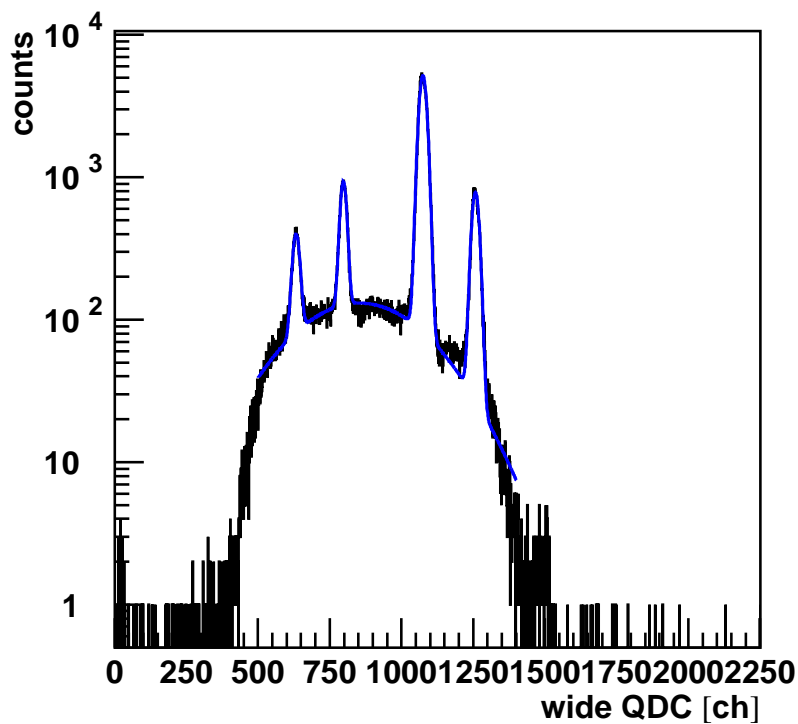


Figure 5.3: A typical wide-gate QDC spectrum. The resolution of the energy deposition measurement is about 2 % FWHM. Because of the saturation only qualitative information can be taken from this spectrum.

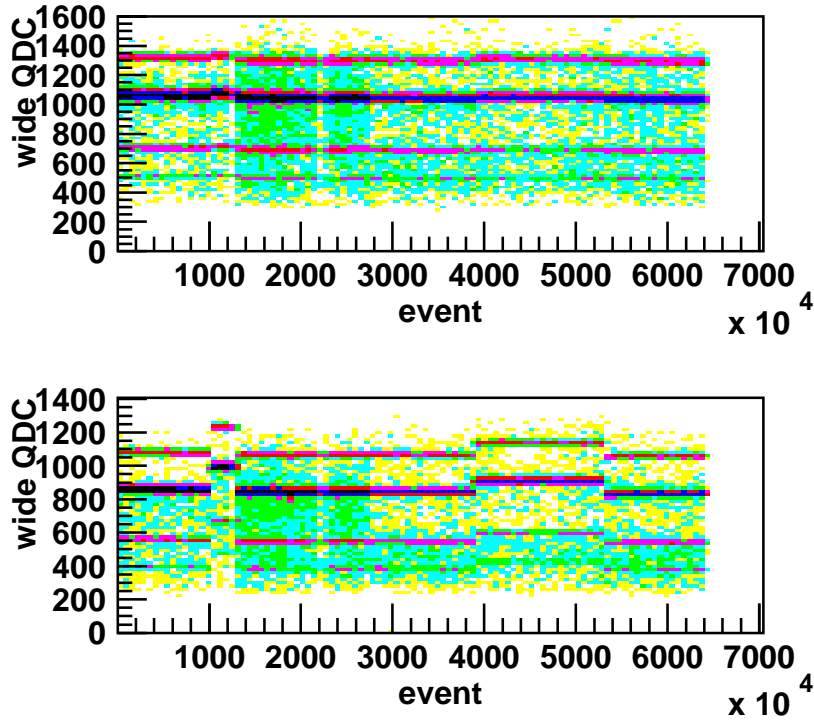


Figure 5.4: A run-wise calibration of QDC signals was needed because of instabilities of gains in certain detectors. Detector #14 was stable (top), but detector #45 was not (bottom). The changes occurred during the longer beam breaks and might be due to the temperature variation at certain detectors.

depends on the temperature [81]. The usual experimental hall temperature was about  $25^\circ\text{C}$  with a variation of  $\pm 5^\circ\text{C}$ . The detector was placed in the vacuum chamber which acts as a thermal insulator decreasing environmental temperature variations even more. The jumps in the gains happened after the longer beam breaks (e.g. when a liquid helium dewar got replaced) and this effect can be assigned to the possible local temperature changes around certain detectors. In order to compensate for that effect, a run-wise calibration of the QDC spectra has been done.

## CHAPTER 5. DATA ANALYSIS

A calibration procedure of the QDC spectra adjusts the peaks (which correspond to the light hydrogen and helium ions) to the same positions. This step is not an absolute calibration because the energies and energy losses in different detectors are different. However, such a relative calibration helps to collect higher statistics in narrower peaks of rare particles and allows to define common selections for all detectors.

### Light output dependence

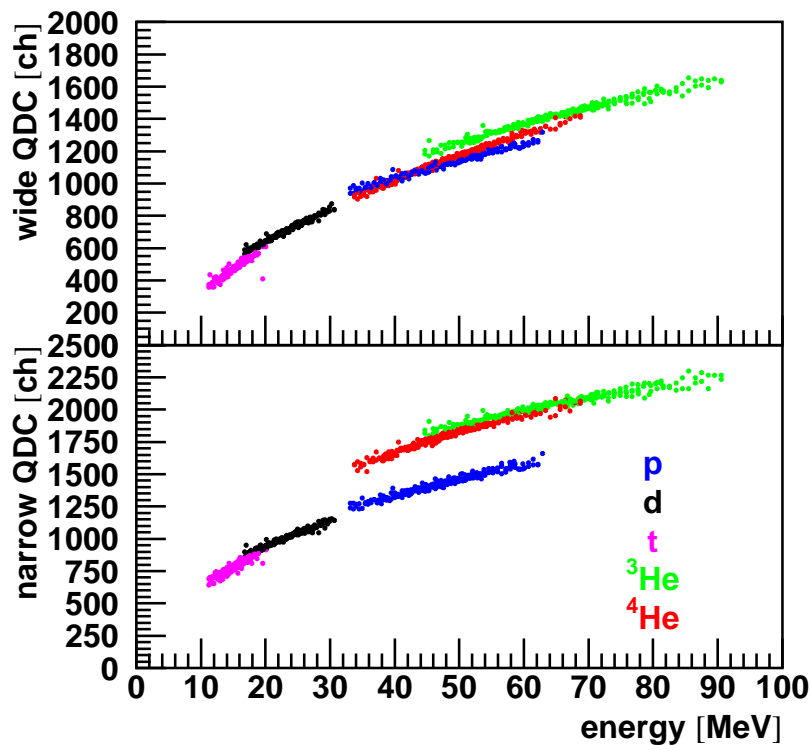


Figure 5.5: Gain-matched light outputs as a function of the particle energy for the wide (top) and narrow (bottom) QDC integration. Only the particles with sufficient statistics and coverage of the focal plane are used for the gain matching.

The momentum calibration parameters have been used to determine the kinetic energy of a particle knowing its mass and charge (for the particle

## CHAPTER 5. DATA ANALYSIS

identification see the following subsection). Hereby the peak position in the QDC spectrum as a function of the energy of the particle is obtained. By changing the BBS rigidity settings, a particle of a certain kinetic energy can hit different modules along the focal plane. A comparison of the peak positions in different detectors for particles of equal energies provides a gain matching of the QDC spectra.

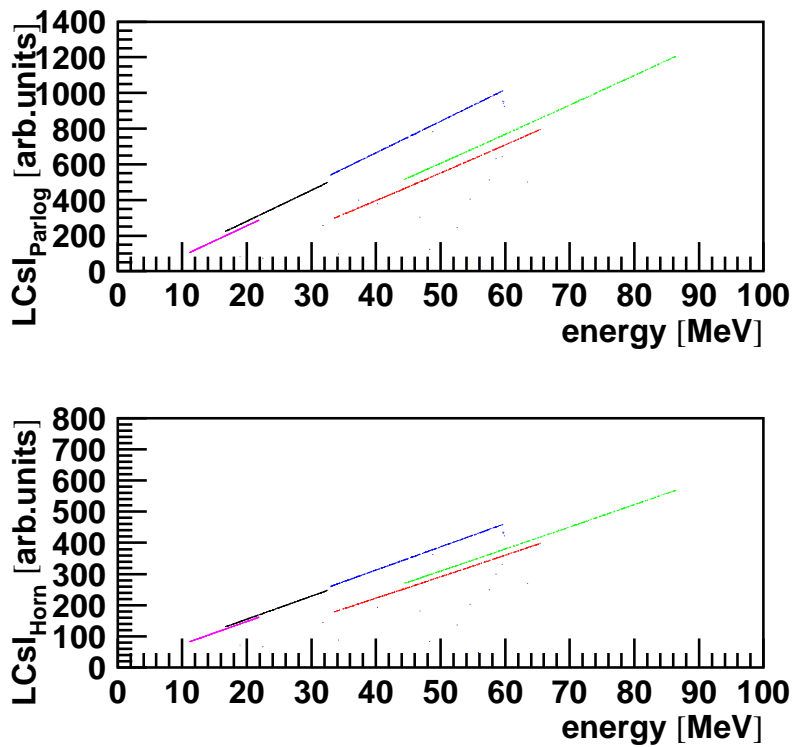


Figure 5.6: The light output obtained from fit formulas in [82] (top) and [83, 84] (bottom) for the quenching of light yield in a CsI(Tl) crystal.

Unlike the elastic scattering used in the momentum calibration, light fragments produced in the  ${}^3\text{He}+{}^4\text{He}$  reaction exhibit a continuous energy spectrum and cover a wide momentum range. Apart from the main measurement in the  ${}^3\text{He}+{}^4\text{He}$  experiment done at the nominal BBS rigidity



## CHAPTER 5. DATA ANALYSIS

( $\delta p/p_{central}=0\%$ , where  $p_{central}$  corresponds to a  ${}^7\text{Be}$  with an energy of 98.5 MeV), a small amount of data was taken at a central-ray momentum deviation of -12%, -6% and +6% from the nominal one. This covers a momentum range of 18% in one detector module and, since the full momentum acceptance equals 19%, there is a large overlap of the momenta that can be used for the QDC gain matching.

When the gain matching is done, the calibrated light outputs for different particles and kinetic energies in all detectors show a smooth behavior (Fig. 5.5). The wide-gate spectrum represents the light output mainly from the CsI(Tl) scintillator since the contribution from the plastic scintillator foil is small, especially for the lightest particles. A non-linear dependence of the light output on the energy deposited by a particle is observed. The data show a saturation not consistent with [82–84] (see Fig. 5.6). This might come from a PMT saturation although the HV is set to avoid the relative saturation of the wide QDC signal to the narrow one (see Sec. 3.3.2). Moreover, in the data a difference between hydrogen and helium ions because of quenching<sup>1</sup> is not observed. However, the light collection on the photocathode may differ from that in the mentioned references. In addition, although the PMTs are magnetically shielded, the high magnetic fields from the spectrometer still may cause problems.

The narrow-gate spectrum shows a nice separation between the hydrogen and the helium line since the small light-output contribution of the fast plastics was noticeable at the rising edge of the signal integrated with the narrow gate.

Because of the observed non-linear saturation-like behavior for the lightest ions, the particle kinetic energy could not be determined from the QDC data but rather from the momentum measurements discussed in the previous subsection. The wide- and narrow-gate signals will be used qualitatively for the particle identification.

---

<sup>1</sup>The reduction of the light yield in a scintillator with regard to the linear dependence on the deposited energy. It depends on the type of the particle.

## Pulse-shape analysis

The combination of phoswich detectors and magnetic spectrometer offers a powerful tool for the identification of charged particles. Each particle has a well defined kinetic energy and, therefore, a well defined energy loss in both scintillators within a phoswich detector.

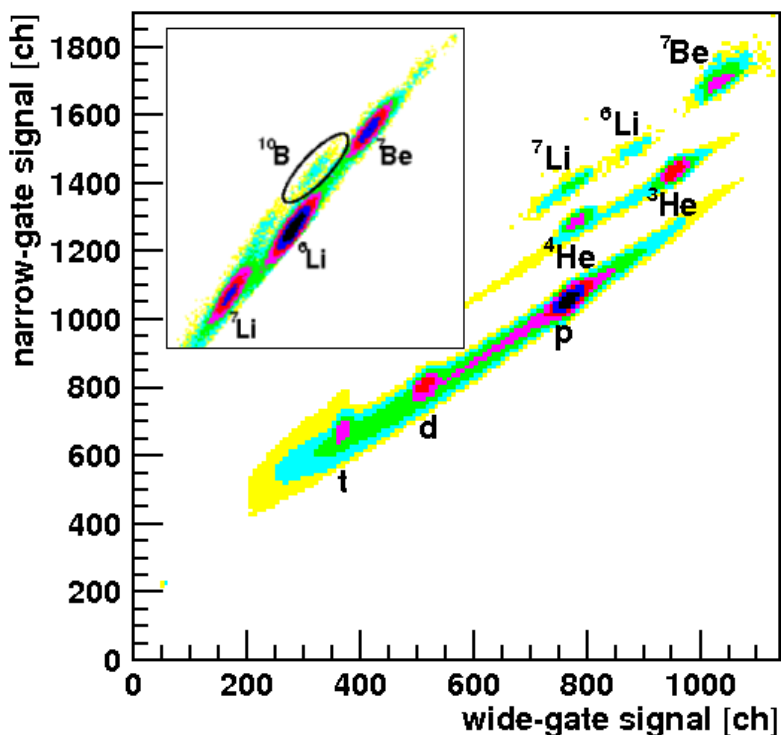


Figure 5.7: The pulse-shape diagram in a HI phoswich detector from the  ${}^3\text{He}+{}^4\text{He}$  (main plot) and  ${}^4\text{He}+{}^6\text{Li}$  data (insert). Amounts of the lithium and beryllium ions in the first data are magnified 100 times. The insert shows only heavier particles with a calibration specific for those particles.

A typical pulse-shape plot from the  ${}^3\text{He}+{}^4\text{He}$  experiment is shown in Fig. 5.7. In the graph different peaks correspond to different ions. The background bands between the peaks originate from the particles re-scattered from the Faraday cup. (This background does not shift along the focal plane when the central-ray rigidity is changed.) In the insert a detailed plot of the  ${}^4\text{He}+{}^6\text{Li}$  data [57] around the  ${}^{10}\text{B}$  region is presented. The qualitative

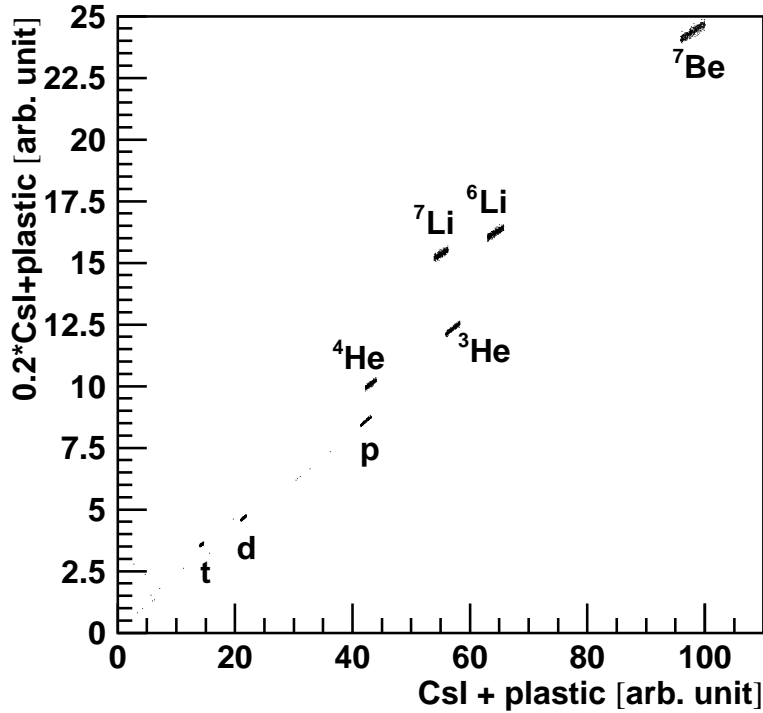


Figure 5.8: Pulse shape plot obtained from GEANT simulation.

agreement with the simulated data leads to the particle identification for each of the observed peaks.

Particles with higher charge number deposit a larger fraction of energy in the plastic scintillator contributing to the narrow-gate signal more significantly than to the wide-gate signal. Hence the heavier particles are found on the lines farther from the diagonal which is associated with neutral particles that do not deposit any energy in the thin plastics.

One can observe that lines of heavier particles are closer to each other although their energy differences and the corresponding differences of the energy losses should increase. That can be qualitatively explained by a considerable light quenching and/or the wide- and narrow-gate signal saturation observed for the lightest ions (Fig. 5.5).

## CHAPTER 5. DATA ANALYSIS

The analysis which takes into account the light quenching in both scintillators showed a qualitative agreement (Fig. 5.9). For the narrow rigidity range the light contributions from the scintillators are disentangled from the wide signal which contains both contributions and the narrow signal which contains the whole fast contribution and only partially the slow one. The wide- and narrow-gate signals can be expressed in terms of the light output from the CsI(Tl) and the plastic scintillators as

$$W = L_{CsI} + L_{plas} \quad (5.1)$$

$$N = G(\alpha L_{CsI} + L_{plas}), \quad (5.2)$$

where  $W$  and  $N$  are the wide- and narrow-gate QDC signals, respectively,  $L_{CsI}$  and  $L_{plas}$  are the contributions of the light outputs of the CsI and the plastic scintillators, respectively,  $G$  is a gain factor due to the unequal splitting of the signal at the input of the QDCs and  $\alpha$  is the fraction of the slow CsI signal which is integrated by the narrow gate. The reference signals were the measured signals from the photons which do not deposit the energy in the plastics and the fast pulser signals which are completely within the narrow gate. The photon signals contain the contribution from the slow component only ( $L_{CsI}$ ) and the ratio  $\frac{N}{W} = G\alpha$  can be determined from the measurements. The fast pulser signals simulate the fast signals from the plastic scintillator ( $L_{plas}$  only) and the corresponding ratio  $\frac{N}{W}$  is equal to the gain factor  $G$ . The measured values  $G = 9$  and  $\alpha = 0.15$  are used to invert Eq. 5.1 and 5.2 and the obtained light outputs for different ions are shown in Fig. 5.9(left). The simulated light outputs are obtained from the empirical formulas [82, 85] for the energy losses obtained from the GEANT simulation for a certain rigidity bin.

Since the production of heavier particles is very much suppressed, the calibration is fine-tuned in the region of the ion of interest (e.g.  $^{10}\text{B}$  in Fig. 5.7). All identified particles are confirmed by a TOF measurement. In addition, the heavy ions  $^7\text{Be}$  and  $^{10}\text{B}$  have been found to be in coincidence with two photons at a large relative angle which is a signature of a low-energy neutral pion.

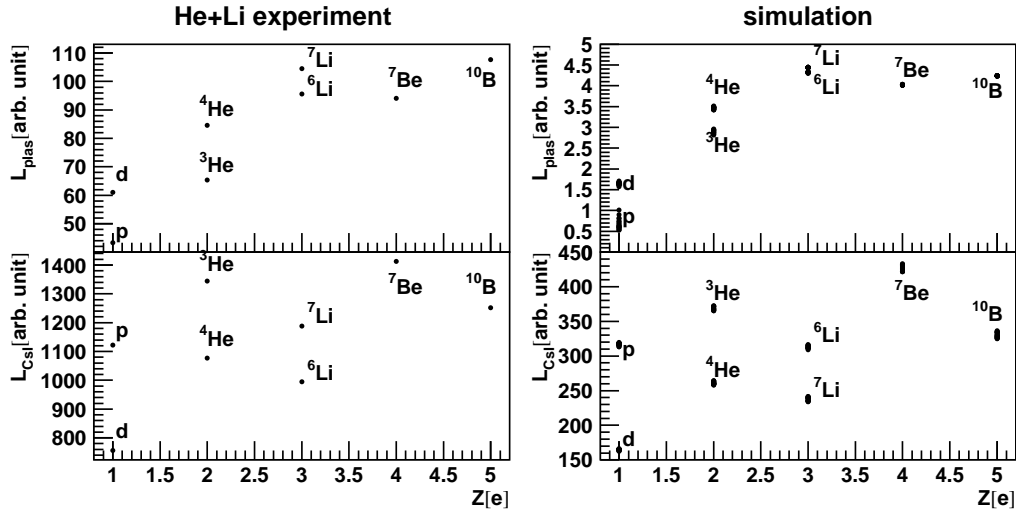


Figure 5.9: Comparison of the light outputs in the plastic and CsI scintillators obtained from the data [57] (left) and from the simulation using the formulas from [82] and [85] (right), as function of the charge-number  $Z$  of the ions.

### Time-of-flight measurements

In the pionic-fusion experiments the photon detectors in a coincidence with the HI detector can be used for a TOF measurement and serve as an additional means for the particle identification. All ions produced in the target are in a coincidence with photons accompanying the ion production. The coincidence trigger signal (see Fig. 3.8) is generated by the narrow PBOR signal which falls within the wide HIOR signal. Therefore, the timing is defined by the PB signal and serves as a start for the HI TDC. The TDC is stopped by a signal from each individual HI detector module. The obtained TDC spectrum represents a TOF distribution of particles in the particular module.

A well defined energy of a certain particle in a single HI detector implies a well defined TOF since the particle trajectory is approximately fixed. Consequently, in the TDC spectra there are also peaks associated with different ions together with a background of random coincidences.

The TDC gains have been calibrated by two narrow self-triggering peaks

## CHAPTER 5. DATA ANALYSIS

separated by the fixed delay. They are consistent with the nominal TDC range of 500 ns initialized in CAMAC (Fig. 5.10). The time offsets have been obtained from a relation of the TOF to the mass-to-charge ratio of the particles (protons, alphas and  $^3\text{He}$ ) identified with the pulse-shape analysis

$$TOF[\text{ns}] = T_{TDC} - T_0 = \frac{L}{v} = 10.364 \frac{L[\text{m}]}{B[\text{T}]\rho[\text{m}]} \cdot \frac{m[\text{u}]}{q[\text{e}]} \quad (5.3)$$

with  $L$  being the path length from the target to a particular HI module,  $m$  the particle mass,  $v$  the particle velocity,  $q$  its charge,  $B$  the magnetic field and  $\rho$  the radius of the trajectory in the dipole magnetic field. By knowing the rigidity associated with each detector module, the fit parameters of the expression in Eq. 5.3 give the path length of the particle trajectories from the target to the module (Fig. 5.11). It gives the real detector position used in the ray-trace simulation.

The TOF systematically changes along the focal plane as a consequence of different momenta and path lengths. Their interplay makes the TOF shorter for higher momentum particles. The above relation can be used to measure the mass-to-charge ratio which, unlike the TOF, must have constant values

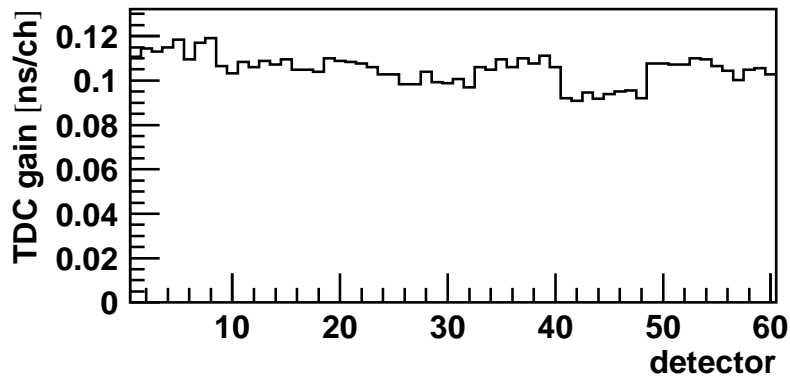


Figure 5.10: Calibrated TDC gains for all detectors of the HI detector array.

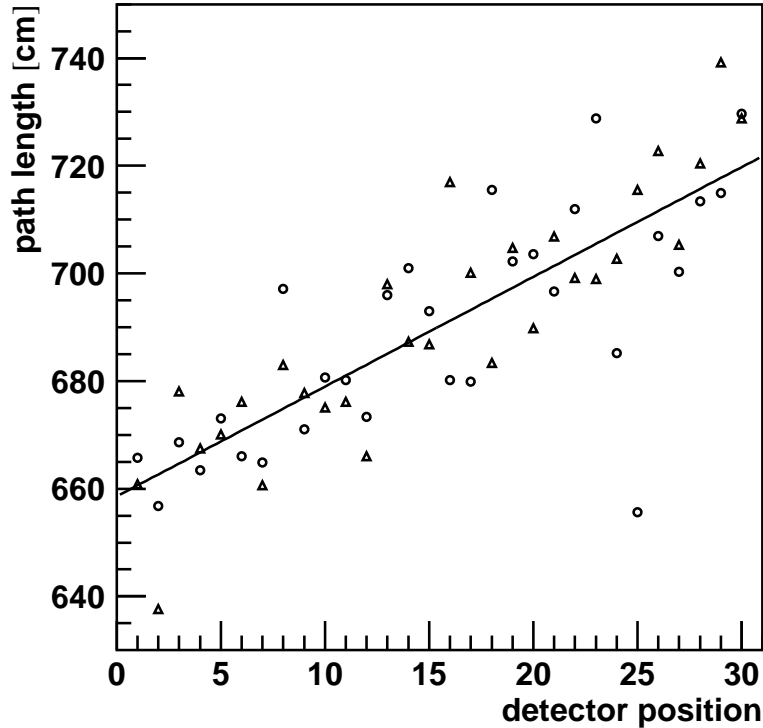


Figure 5.11: The path length of the particle as function of the position of the detector hit by that particle. Circles are for the upper detectors, triangles for the lower ones.

over the entire HI detector. The mass-to-charge distributions of the whole HI detector are shown in Fig. 5.12. The time resolution  $\sigma=7.5$  ns transforms to a  $m/q$  resolution of 0.2 u/e FWHM. The distributions are obtained for several ions which were selected by their pulse shape and normalized to the same peak height. In each distribution there is a peak above a random background in the coincidence time window and a structure on the right edge due to the self-triggering peaks. From the  ${}^7\text{Be}$  spectrum the background contamination can be estimated to 8%.

Combining the wide- and narrow-gate QDC data with the TDC data, a successful background rejection can be done in an analysis of the pionic-fusion

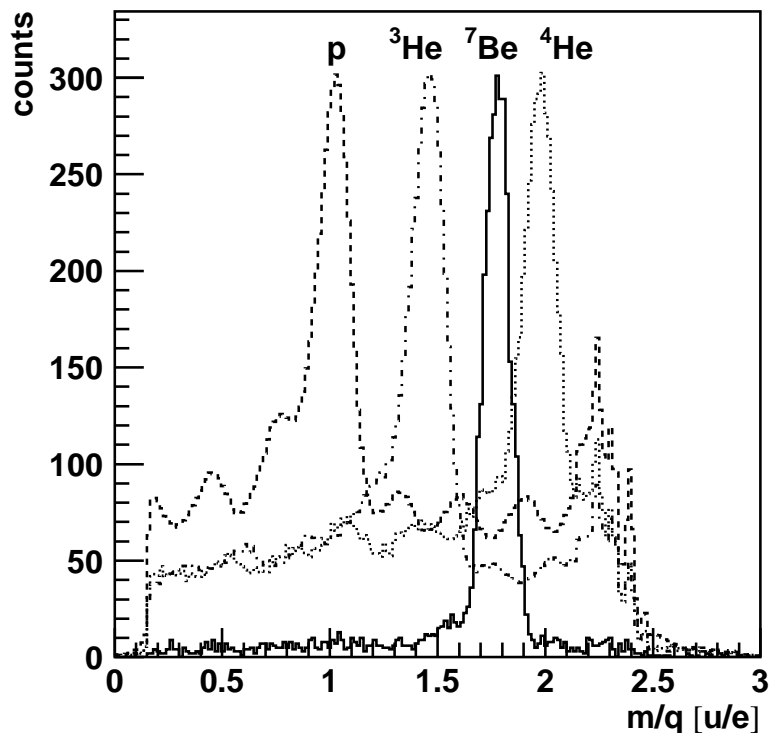


Figure 5.12: Mass-to-charge distribution derived from the time-of-flight measurement. Different ions are selected by using the pulse-shape diagram. Each histogram is normalized to the same peak height. The deviations from the nominal  $m/q$  are due to a slight walk effect in the leading-edge discriminators.

data. For a further rejection of the background and a complete determination of the kinematics of the reaction, the information about photons is necessary.

### 5.1.2 Photon detectors

In the photon detectors, first of all, photons have to be identified. Since the PB modules are phoswich detectors, they provide a particle identification by means of the pulse-shape discrimination technique. This is analogous to the HI detectors except the slow scintillator is thin and the fast one is thick. The



## CHAPTER 5. DATA ANALYSIS

other difference is that the particles are not momentum analyzed before they reach the detectors. A pulse-shape diagram for a PB detector is shown in Fig. 5.13. Here the experimental data of the  ${}^3\text{He}+{}^4\text{He}$  reaction together with the cosmic rays are compared to the simulated response of the PB detector. The energy depositions in the simulated data are combined to reproduce the narrow and wide integrated signals. Photons do not deposit a significant amount of energy in the thin  $\text{CaF}_2$  crystal and, therefore, are found on the diagonal of the pulse-shape plot. Whereas the forward PB detectors are flooded by charged particles and the pulse-shape discrimination is necessary, the backward PB detectors are shadowed by the IS detectors and for the reaction energies of interest only photons can punch through and produce a signal in the PB detector. Consequently, every signal in a backward PB module is produced by a photon that had gone through a IS module and a spatial correlation between these signals must exist (Fig. 5.14). Imposing the conditions on the timing of the signals (middle plot) and on the energy deposition (lower plot) the huge amount of uncorrelated background signals

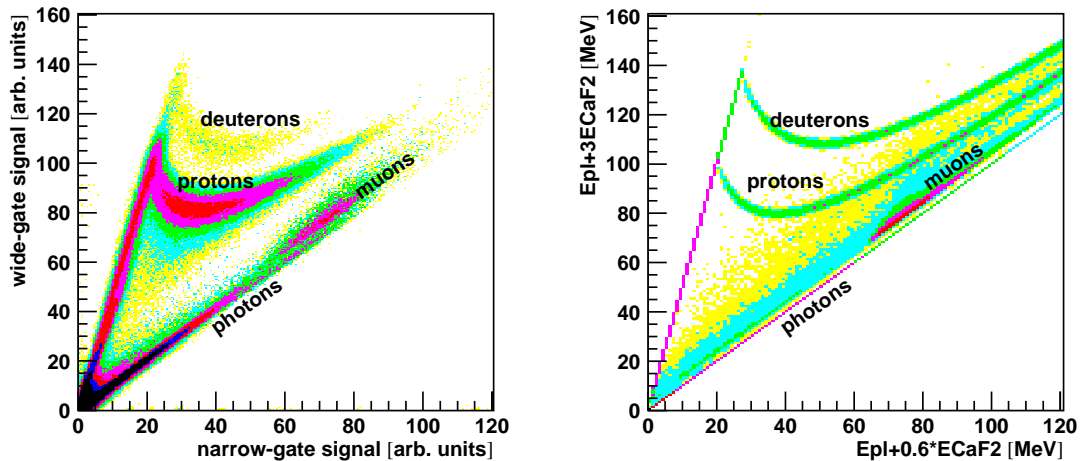


Figure 5.13: Pulse-shape diagram for a PB detector module for the experimental data (left) and simulated pulse-shape diagram with energy depositions adjusted to reproduce the experimental data (right).

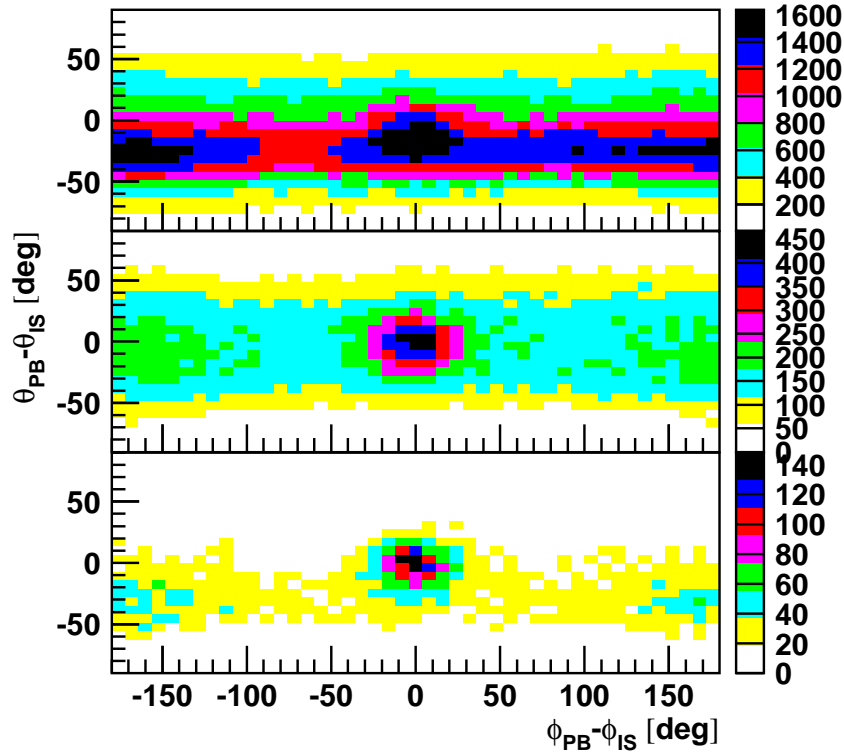


Figure 5.14: Angular correlation between the PB and IS detectors expressed by the differences in polar angle as function of the differences in azimuth. Top: correlation without any condition on hits, middle plot shows coincident hits; Middle: Coincident hits; Bottom: Excluding low energy PB hits which predominantly come from the uncorrelated background.

is rejected.

The particles in the photon detectors produce electromagnetic showers which can spread over several modules. In order to collect the total deposited energy the contribution of neighboring detectors are summed. Since also discontinuous showers may occur, not only the first but also the second and the third neighbors are included in the cluster if they fired in coincidence. The angular position of the hit is determined by the average position of all detectors in the cluster weighted by the energy deposition in each detector. The time of the hit is taken from the time signal of the detector with the

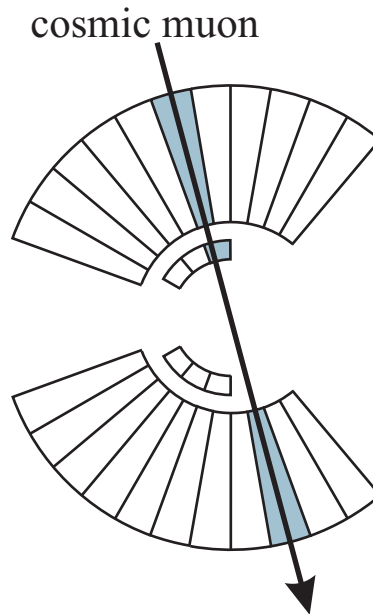


Figure 5.15: Tracking of a cosmic muon in PB and IS detectors.

highest energy deposition. Moreover, the energy loss in the IS detector in coincidence with a PB cluster in a cone of  $\pm 25^\circ$  is added. The angular resolution is obtained from the GEANT simulation and is equal to 6% and 9% for forward and backward detectors, respectively (Fig. 3.13).

The time calibration was trivial since the time spectra have a pronounced self-triggering peak which is associated to the reference signal. The PB and IS TDCs worked in a common stop mode so that the signals at higher TDC channels come from particles arriving earlier at the detector. The TDC gain was equal to 1 ns/ch.

The ADC calibration was based on the measurements of high-energy cosmic muons. The cosmic data have been taken for a total period of several weeks before and after the data-taking experiment and during the breaks of the experiment. The high-energy cosmic rays are approximately 2 GeV muons and they deposit a well known average amount of energy in the detector. The most important task here was to identify the high-energy muons which passed along the detector. The PB and IS combination allowed us to select such muon tracks by choosing the events with hits in PB detectors on

CHAPTER 5. DATA ANALYSIS

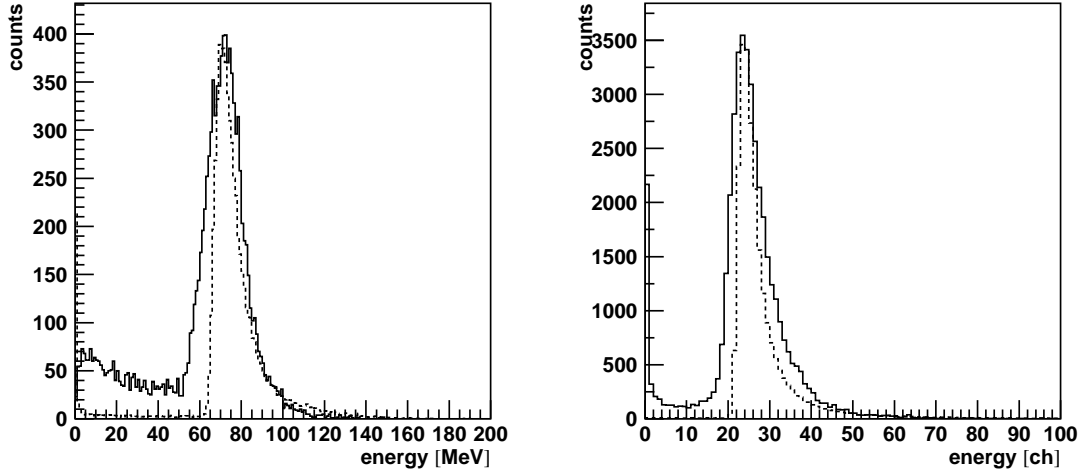


Figure 5.16: Energy deposition peak of cosmic muons in a PB (left) and a IS detector module (right). The solid and the dashed lines show the measured and the simulated data, respectively.

the opposite sides of the whole detector and the IS detector between them (Fig. 5.15). By taking the hits under a condition that neighboring detectors did not fire, a particle which travels along the detector is selected. The measured energy is compared to the simulated energy loss and thus the absolute

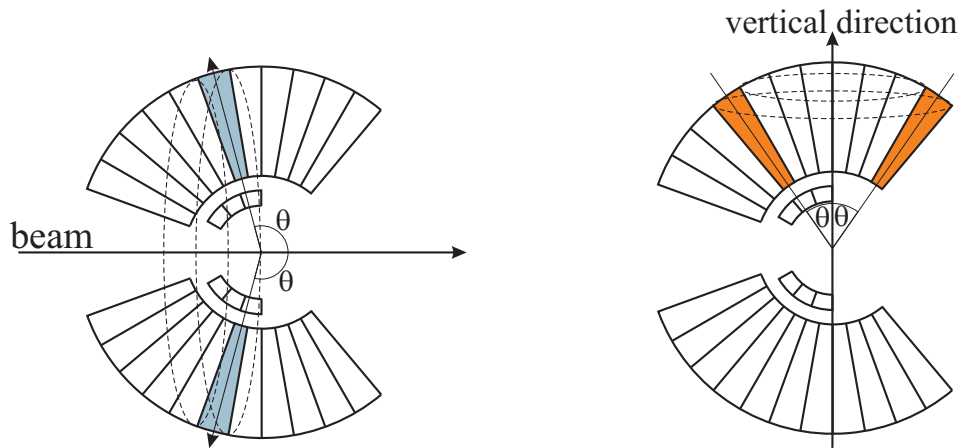


Figure 5.17: Azimuthal symmetry of detector positions around the beam (left) and the vertical direction (right).

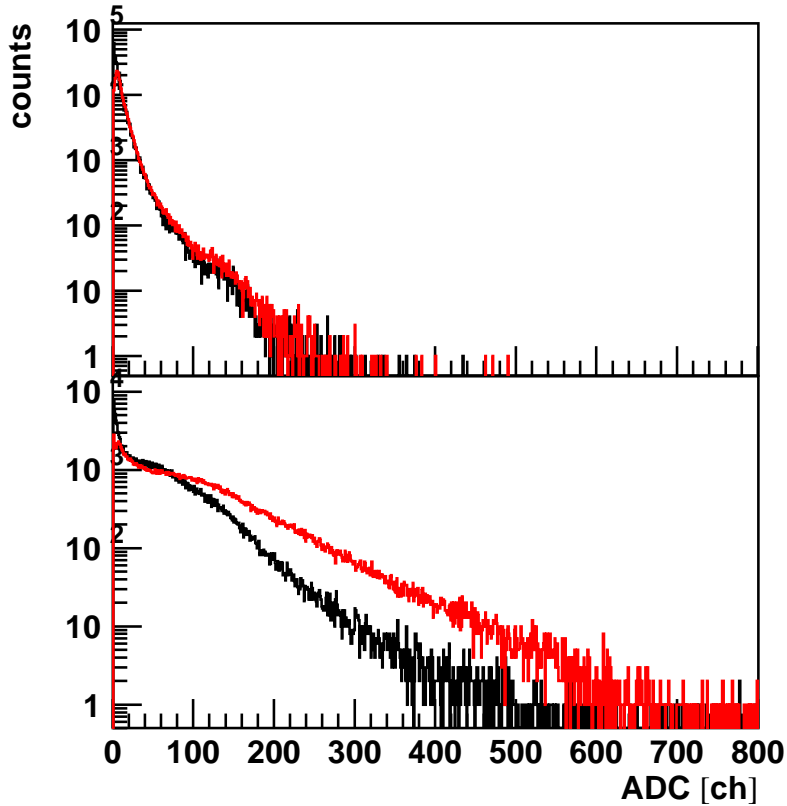


Figure 5.18: Raw ADC spectra for two PB detector modules at two different positions and orientations. The black histogram represents a detector at  $\theta=105^\circ$  and  $\phi=0^\circ$  and the red one a detector at  $\theta=105^\circ$   $\phi=90^\circ$ . They have equal ADC gains. Top:  ${}^3\text{He}+{}^4\text{He}$  data; Bottom: Cosmic-ray data.

calibration is obtained (Fig. 5.16). The pedestals were subtracted so that channel zero can be assumed to correspond to zero energy deposition.

However, because of the angular distribution of the cosmic rays, detector modules at more horizontal positions do not collect high statistics of cosmic rays passing along the full length of the detector. On the other hand, those detector modules do not have peers on the opposite side. That makes the calibration of such detector modules more difficult. In order to perform the calibration, data taken during the production experiment are used to adjust the gains of detector modules within one ring, i.e. detectors at approximately

identical polar angle (Fig. 5.17 left). Due to the axial symmetry of the reaction, the energy spectra of particles at different azimuthal angles but at the same polar angle, are expected to have the same shape (upper plot of Fig. 5.18).

Moreover, due to the symmetry of the cosmic ray angular distribution with respect to the vertical direction (Fig. 5.17 right), the detectors with an equal orientation relative to the vertical direction should have the same energy deposition spectra. The detectors in the rings at small relative angle to the horizontal direction and, therefore, small amount of cosmic-ray tracks passing the whole length of the module, can be compared to the cross-calibrated detectors at the same angle to the vertical direction. They have smaller energy deposition of the cosmic muons than the more vertically oriented detectors (Fig. 5.18 bottom).

## 5.2 Event selection

Among a plentiful of data passing the fast trigger conditions and being collected to the disk storage, there is only a very small amount of the wanted pionic-fusion events. Therefore, the proper events should be selected and the rest (background) must be rejected. In the previous sections the particle selection is explained. The beryllium ions are identified in the phoswich detectors by the pulse-shape analysis and the time-of-flight measurement. It is shown that these conditions are well correlated (Fig. 5.12) and reduce the background considerably.

Also, the photon identification is explained in both the forward and the backward PB detectors. In order to select the proper events and reconstruct the full kinematics of the reaction, both photons from the pion decay must be identified. These photon signals must be in coincidence, i.e. their time signals must be around the self-triggering peak ( $\pm 20$  ns). Uncertainties arise at low deposition energy since the photons cannot be distinguished from the low-energy protons stopped in the  $\text{CaF}_2$  scintillator of the forward PB detectors (Fig. 5.13). Nevertheless, the low-energy signals come mostly from the de-excitations of nuclear fragments and are not correlated with other signals

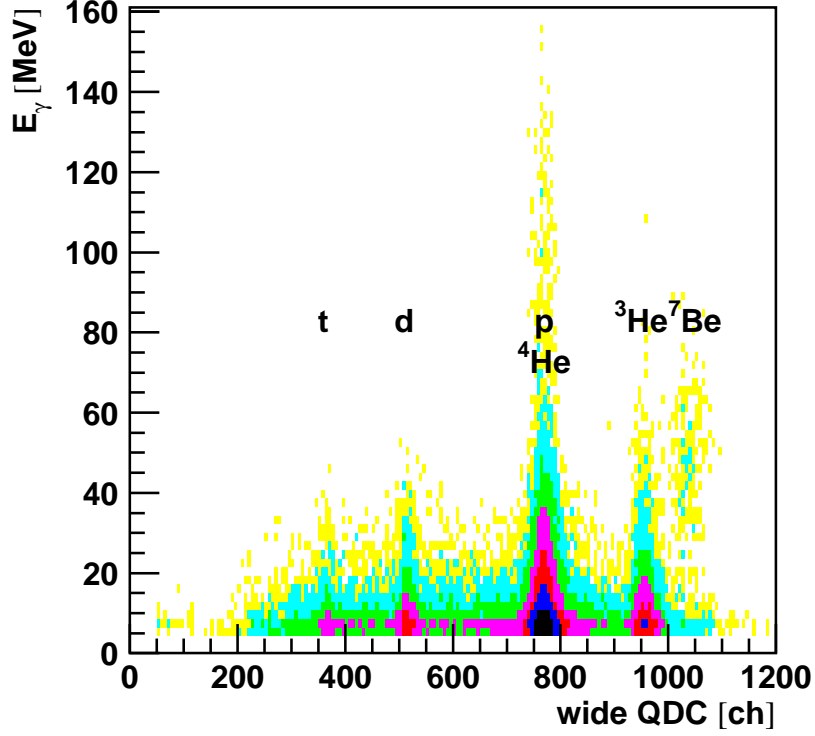


Figure 5.19: PB energy deposition as function of the wide-gate QDC energy in the HI detector, showing the correlation between high-energy photons and the fused  ${}^7\text{Be}$  ions.

expected in the pionic-fusion reaction. In Fig. 5.19 a plot of the energy deposition in the PB and the IS detector as function of the wide QDC signal in the HI detector is shown. The events with a  ${}^7\text{Be}$  are correlated with the ones with the high-energy photons from a pion decay.

When at least two photon energy deposition are identified, the opening angle between them is determined. The opening angle between two photons can be calculated from their measured angles  $\theta_1$ ,  $\phi_1$  and  $\theta_2$ ,  $\phi_2$ :

$$\theta_{\gamma\gamma} = \arccos(\sin \theta_1 \sin \theta_2 \cos(\phi_1 - \phi_2) + \cos \theta_1 \cos \theta_2). \quad (5.4)$$

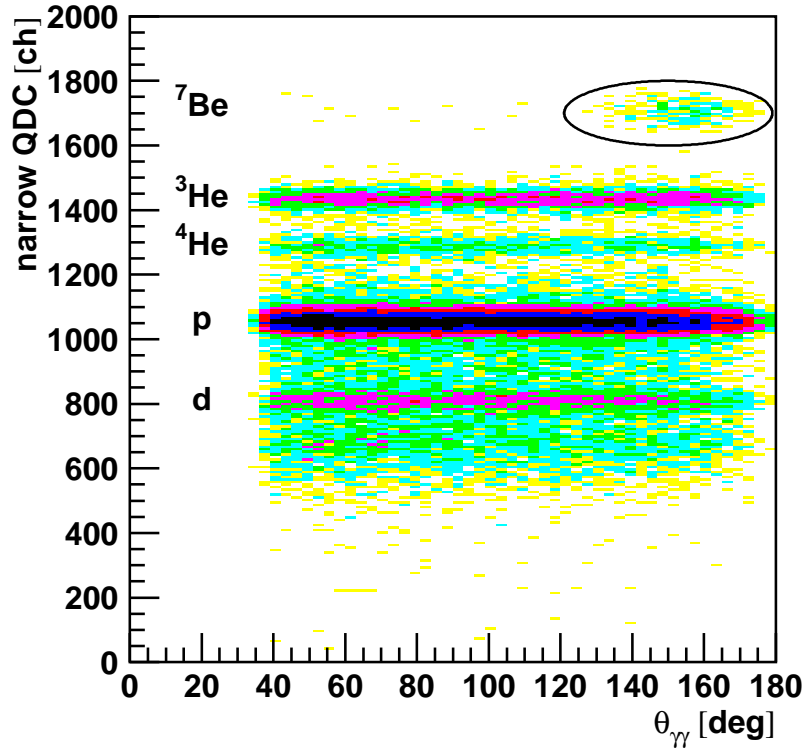


Figure 5.20: Narrow-gate energy deposition in the HI detector array as function of the two-photon opening angle, showing that  ${}^7\text{Be}$  events are associated with large opening angles between the photons.

The HI narrow-gate QDC signal as function of the opening angle distribution is shown in Fig. 5.20. The distribution for most of the ions shows a spread over all angles. However, for the beryllium ions the distribution is concentrated at large opening angles. The opening angle distribution for the events with identified  ${}^7\text{Be}$  is shown in Fig. 5.21. This shows that detected  ${}^7\text{Be}$  comes in coincidence with two photon tracks at large opening angles, which is a signature of a decay of a slow neutral pion.

Approximately 500 events have been successfully selected with a negligible background ( $\sim 1\%$ ).



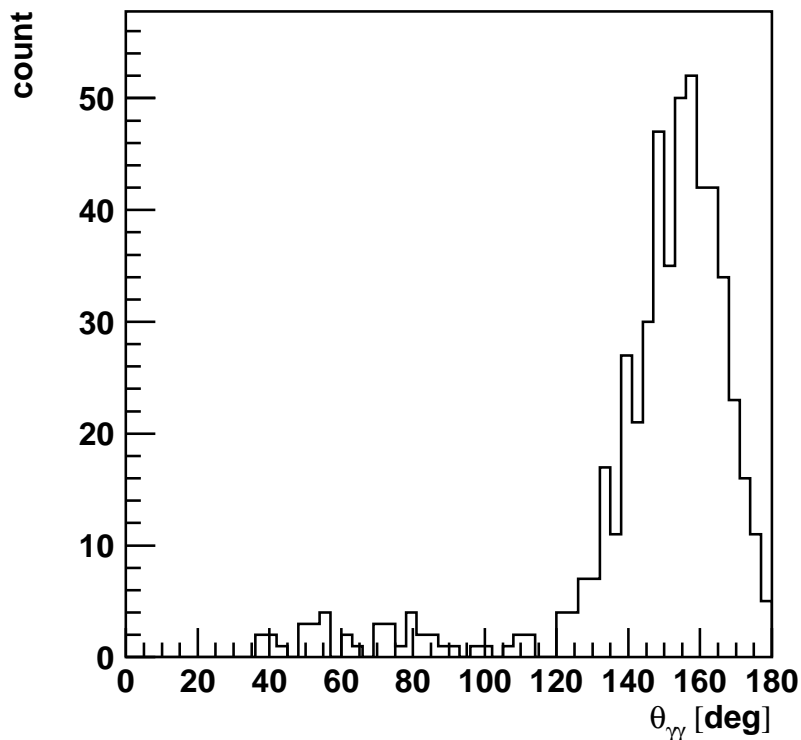


Figure 5.21: The two-photon opening angle distribution with the  ${}^7\text{Be}$  selection imposed.

### 5.3 Kinematical reconstruction

The next step in the analysis procedure is to verify the kinematics of the selected pionic-fusion events. This is necessary for a determination of the cross section that can be compared with the theoretical predictions. However, a precise evaluation of the kinematics has the following drawbacks:

- the unknown direction of the fused nucleus,
- the completely destroyed information about the kinetic energy of  ${}^7\text{Be}$  ions at the production time because of the energy loss in the thick liquid helium target,
- a finite resolution in the measurements of angles and energies.

## CHAPTER 5. DATA ANALYSIS

Since the pionic-fusion final state is a two-body state, the physics of the process with averaged polarizations is determined by one kinematical variable only (usually the pion polar angle). For each detected pionic-fusion event one has to determine that kinematical variable from the measured ones. But, since the pion decays into two photons, in the final state there are three particles whose energies and momenta obey the conservation laws and the invariant mass of the two photons is equal to the neutral pion mass.

The energy conservation law in the laboratory system gives

$$E_{tot} = E_{\gamma 1} + E_{\gamma 2} + E_{\tau_{Be}}, \quad (5.5)$$

where the total energy is obtained from the beam kinetic energy and the masses of the particles in the initial state

$$E_{tot} = M_{3He} + M_{4He} + T_{beam}. \quad (5.6)$$

The constraints on particle momenta are

$$0 = p_{x1} + p_{x2} + p_{x3} \quad (5.7)$$

$$0 = p_{y1} + p_{y2} + p_{y3} \quad (5.8)$$

$$p_{beam} = p_{z1} + p_{z2} + p_{z3} \quad (5.9)$$

which can be expressed by the photon angles:

$$0 = E_{\gamma 1} \sin \theta_1 \cos \phi_1 + E_{\gamma 2} \sin \theta_2 \cos \phi_2 + p_{x3} \quad (5.10)$$

$$0 = E_{\gamma 1} \sin \theta_1 \sin \phi_1 + E_{\gamma 2} \sin \theta_2 \sin \phi_2 + p_{y3} \quad (5.11)$$

$$p_{beam} = E_{\gamma 1} \cos \theta_1 + E_{\gamma 2} \cos \theta_2 + p_{z3}. \quad (5.12)$$

For the full reconstruction of the kinematics of an event one needs five independent kinematical variables. Four of them are the photon angles measured with a good resolution (Fig. 3.13) and the fifth can be the photon energy deposition. The energy resolution of the photon detectors is modest (Fig. 3.14). A majority of photons entering the detector does not deposit

## CHAPTER 5. DATA ANALYSIS

any energy at all, and even detected particles punch through the detector and do not deposit their whole kinetic energy. The situation is better in the backward hemisphere where the IS detector improves the efficiency and the energy resolution. Nevertheless, because of the reaction kinematics where the two photons are emitted at large opening angles in the laboratory system, in most cases one photon is detected in the forward hemisphere with the PB detector only. Therefore the best event determination is realized by selecting the photon with the higher energy deposition and use its energy as the fifth kinematical variable necessary for the reconstruction.

The energy of the other photon can be derived from the conservation laws and equals

$$E_{\gamma 2} = \frac{p_{beam}^2 + m_{\gamma Be}^2 - E_{tot}^2 - 2E_{\gamma 1}(p_{beam} \cos \theta_1 - E_{tot})}{2(p_{beam} \cos \theta_2 - E_{tot}) + 2E_{\gamma 1}(1 - \cos \theta_{\gamma\gamma})}. \quad (5.13)$$

When the energy of the second photon is known the invariant mass can be calculated according to

$$m_{\gamma\gamma} = \sqrt{2E_{\gamma 1}E_{\gamma 2}(1 - \cos \theta_{\gamma\gamma})}. \quad (5.14)$$

The two-photon invariant-mass distribution of the selected events shows clearly a peak centering at the pion mass value  $m_{\pi^0}=135$  MeV and with 10 MeV FWHM (Fig. 5.22). This confirms the good event selection and that the kinematical reconstruction with the chosen kinematical variables gives correct results. The same analysis has been done with the simulated data obtained by GEANT and the final distribution lies on the top of the experimental one (dashed line in Fig. 5.22).

The pion angle with respect to the beam direction in the laboratory system is

$$\theta_{lab}^{\pi} = \arccos \left( \frac{E_{\gamma 1} \cos \theta_1 + E_{\gamma 2} \cos \theta_2}{\sqrt{(E_{\gamma 1} + E_{\gamma 2})^2 - m_{\gamma\gamma}^2}} \right) \quad (5.15)$$

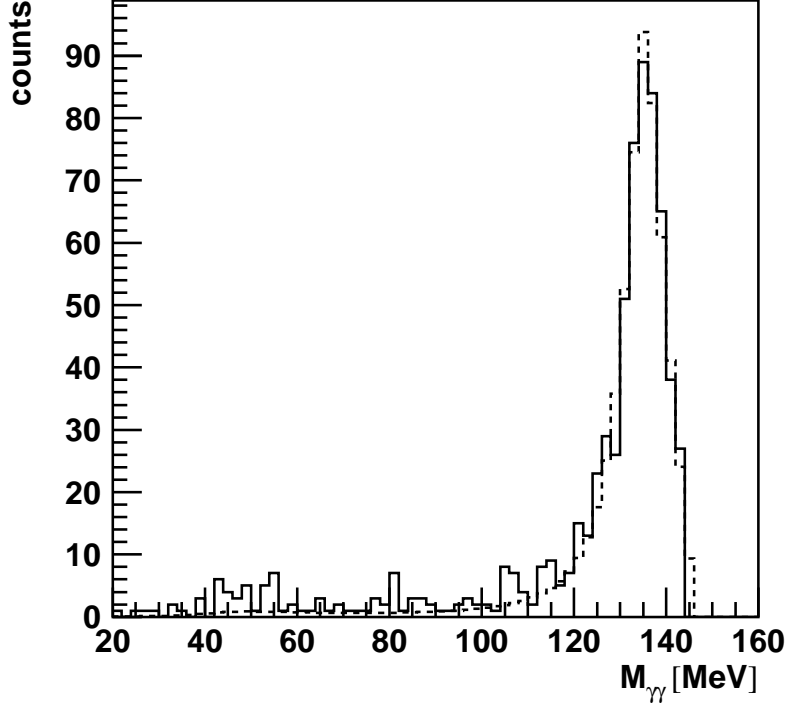


Figure 5.22: Reconstructed two-photon invariant mass from the data (solid) compared to the one obtained from the simulation (dashed).

and in the center-of-mass system

$$\theta_{c.m.}^{\pi} = \arccos\left(\frac{\gamma(p_{\pi} \cos \theta_{lab}^{\pi} - \beta E_{\pi})}{p_{c.m.}^{\pi}}\right), \quad (5.16)$$

where  $E_{\pi}$  and  $p_{\pi}$  are pion energy and momentum in the laboratory system,  $p_{c.m.}^{\pi}$  is the pion momentum in the center-of-mass system,  $\beta$  is the velocity of the center of mass in the laboratory frame and

$$\gamma = \frac{1}{\sqrt{1 - \beta^2}}.$$

## CHAPTER 5. DATA ANALYSIS

The angular distribution obtained by the kinematical reconstruction described above is shown by the dashed line in Fig. 5.23. Due to the finite resolution of input parameters in the kinematical reconstruction, the distribution is distorted and is not equal to the real one. The pion angle is a more sensitive variable to the reconstruction procedure than the invariant mass. To unfold the distribution, results of the simulations are used (Fig. 4.10). The original distribution in the simulations is known and the final distribution is obtained by simulating the detector response and executing the same analysis as for the experimental data.

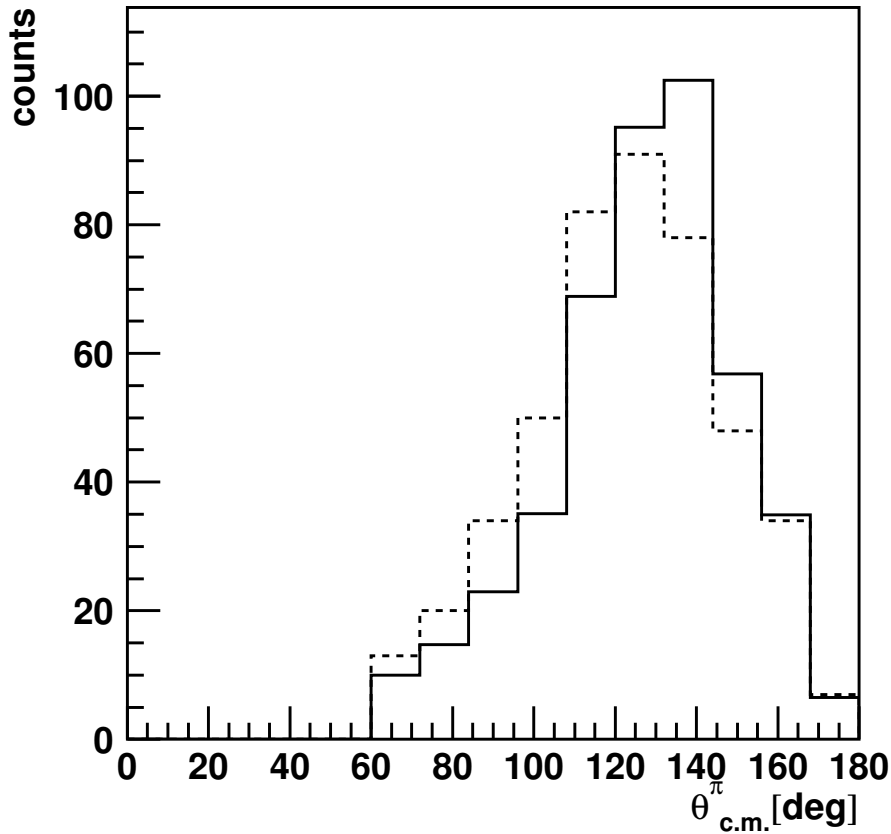


Figure 5.23: The measured distribution (dashed) and the reconstructed one (solid) obtained by unfolding of the measured one.

The full angular range of the true and the reconstructed (or observed) distributions is divided into 15 bins of  $12^\circ$  around  $\theta_i$ . The simulation gives

## CHAPTER 5. DATA ANALYSIS

the probability  $R_{ij}$  that the detectors and the reconstruction procedure give a reconstructed angle in the bin  $\theta_i$  for a true angle in the bin  $\theta_j$ . If the true distribution is given by the number of counts in each bin  $T_j$  ( $j$  runs from 1 to 15), the observed distribution  $O_i$  would be

$$O_i = \sum_j R_{ij} T_j. \quad (5.17)$$

The true angular distribution of pions will be obtained from the observed one and from the response matrix derived from the simulations. An unfolding procedure using correction factors will be applied. This is an iterative procedure which starts from the trial distribution  $T^{(0)}$  to calculate the observed  $O^{(0)}$ . Then a new  $T^{(1)}$  is obtained iteratively from the previous one:

$$T_i^{(1)} = \frac{O_i}{O_i^{(0)}} T_i^{(0)} = O_i \frac{T_i^{(0)}}{\sum_j R_{ij} O_j^{(0)}}. \quad (5.18)$$

By applying this method to the distribution from the simulations, the original distributions are recovered successfully after several iterations. The results of unfolding the experimental data are shown in Fig. 5.23 (solid line). To estimate the errors the measured distribution is varied within the statistical errors resulting in the uncertainties of the real distribution.

### 5.4 Cross section evaluation

Apart from the number of good events and their distribution over the pion angle, the luminosity, the acceptance of the detector system and the data-acquisition dead-time must be determined. The cross section is given by:

$$\sigma = \frac{N_{react}}{\mathcal{L}}, \quad (5.19)$$

## CHAPTER 5. DATA ANALYSIS

where  $N_{react}$  is the number of measured reactions and  $\mathcal{L}$  is the luminosity. The differential cross section depending on  $\theta$  is

$$\frac{d\sigma}{d\theta}(\theta) = \frac{1}{\mathcal{L}} \frac{dN_{react}}{d\theta}. \quad (5.20)$$

From the measurement where the events are grouped in finite-size bins the differential cross section is evaluated with

$$\frac{\Delta\sigma}{\Delta\theta}(\theta) = \frac{1}{\mathcal{L}} \frac{\Delta N_{react}^{within\Delta\theta}}{\Delta\theta}. \quad (5.21)$$

The  $\Delta N_{react}^{within\Delta\theta}$  is the total number of reactions with a kinematical variable  $\theta$  within a region  $\Delta\theta$ .

The number of observed reactions  $N_{obs}$  is not equal to the number of reactions  $N_{react}$  that truly happened because of the limited acceptance of the detector setup and the data-acquisition dead time.

### 5.4.1 Luminosity

The total integrated luminosity is given in terms of the total number of beam particles that passed through the target and the number of target particles per area

$$\mathcal{L} = \frac{N_{beam} N_{target}}{S}, \quad (5.22)$$

where  $S$  is the cross-sectional area of the beam. For this experiment the luminosity is

$$\mathcal{L} = \frac{Q_{tot}}{Z_{3He^{2+}} e} \frac{\rho L N_A}{M_{4He}}, \quad (5.23)$$

where  $Q_{tot}$  is the total beam charge passed through the target,  $Z_{3He^{2+}}$  the atomic number of  $^3\text{He}$ ,  $e$  the elementary charge,  $\rho$  the target density,  $L$  the target thickness,  $N_A$  the Avogadro constant and  $M_{4He}$  is the molar mass of  $^4\text{He}$ .

The integration of the measured beam current (Fig. 3.19) provides the total charge. The target density depends on the temperature which was constantly monitored. As already mentioned in Sec. 3.1 the target density

## CHAPTER 5. DATA ANALYSIS

varied between 130-140 mg/cm<sup>2</sup>. A better information about the target density variations is given by the scaler events. If the raw count rate in any detector, e.g. the HI detector, is divided by the current, a stable ratio is observed through the entire experiment. In Fig. 5.24 the distribution of the ratios of the count rate of the HIOR signal and the beam current is shown. A narrow distribution of 8 % FWHM can be attributed to the target density variations and it is consistent with the rough estimate from the temperature measurements.

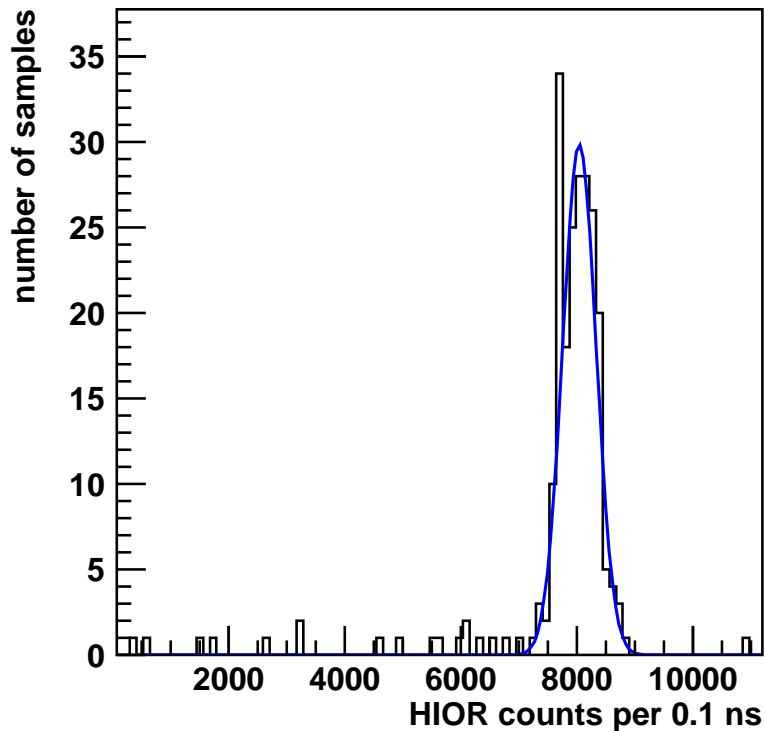


Figure 5.24: Distribution of the ratio of the HIOR raw event count rate and the beam current as a measure of the target density variations.

The nominal target thickness is equal to 1 cm. The real target thickness cannot be determined because of the target bulging. But only the part of



## CHAPTER 5. DATA ANALYSIS

the target is active in producing the pionic-fusion event that can be observed in the experimental setup (see Fig. 4.6). In other words, the inefficiency due to the energy loss in the target fixes the active target thickness.

A dead-time correction to the luminosity is also obtained from the scaler events with the raw counting rates of different signals and the corresponding decreased rates due to the dead-time of the data-acquisition

$$\epsilon_{dt} = \frac{N_{acc}}{N_{raw}}, \quad (5.24)$$

where  $N_{raw}$  is the number of counts entering the trigger box and  $N_{acc}$  is the number of counts during the time when the trigger box is inhibited (or when the data-acquisition system is busy).

The integrated luminosity in the experiment corrected for the dead time was  $(270 \pm 20) \text{ nb}^{-1}$ . The dominant uncertainty comes from the variations of the target density.

### 5.4.2 The acceptance

Besides the events lost during the dead time of the data acquisition, many events are not detected because of the limitations of the detectors or the conditions applied during the analysis to reject the background. First, the geometry of detectors is limited and therefore, when the particle is emitted outside the range of the detector, such an event will be lost. The acceptance depends on the kinematics and some types of events are rejected more than the others. The acceptance has been determined from the simulations (Ch. 4). The influence of different constraints is shown in Fig. 4.9.

The kinematics of a pionic fusion reaction where a fused nucleus is emitted at small polar angles, allows a highly efficient detection of the ion with a spectrometer with a very small opening window around the beam direction. The maximal polar angle allowed for the fused nuclei in the pionic fusion reactions  ${}^3\text{He}+{}^4\text{He}$  and  ${}^4\text{He}+{}^6\text{Li}$  reactions are  $2.6^\circ$  and  $2.2^\circ$ , respectively. The BBS acceptance, defined as the ratio of the number of accepted to the number of produced  ${}^7\text{Be}$  ions is shown in Fig. 5.25 as a function of the polar

## CHAPTER 5. DATA ANALYSIS

angle. The total BBS acceptance depends on the original distribution and for a phase space distribution is equal to 72% and 86% for  ${}^7\text{Be}$  and  ${}^{10}\text{B}$ , respectively.

A ray-tracing simulation [86] is employed to determine the acceptance of the HI detector for the particles that enter the BBS. In Fig. 5.26 the horizontal and the vertical coordinates of the particles in the HI detector are shown as functions of parameters of the reaction at the target. The rectangle in the middle of the plot represents the geometry of the active area of the HI detector. The rigidity increases in the positive x-axis direction. The solid and

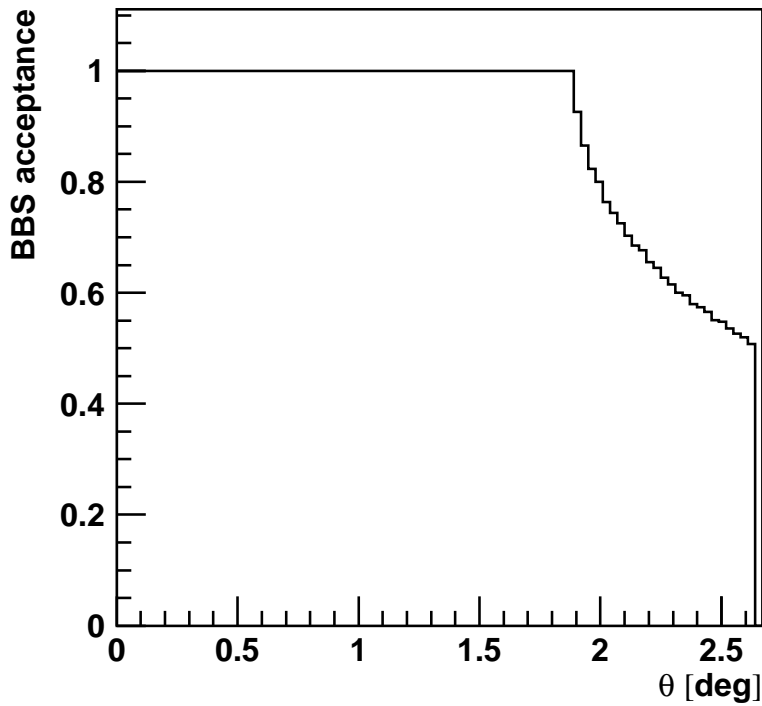


Figure 5.25: The BBS acceptance as function of the heavy-ion polar angle for the reaction  ${}^4\text{He}({}^3\text{He},\pi^0){}^7\text{Be}$ . Because of the rectangular shape of the BBS window, a part of the azimuthal range is obstructed for polar angles  $\theta > 1.9^\circ$ .

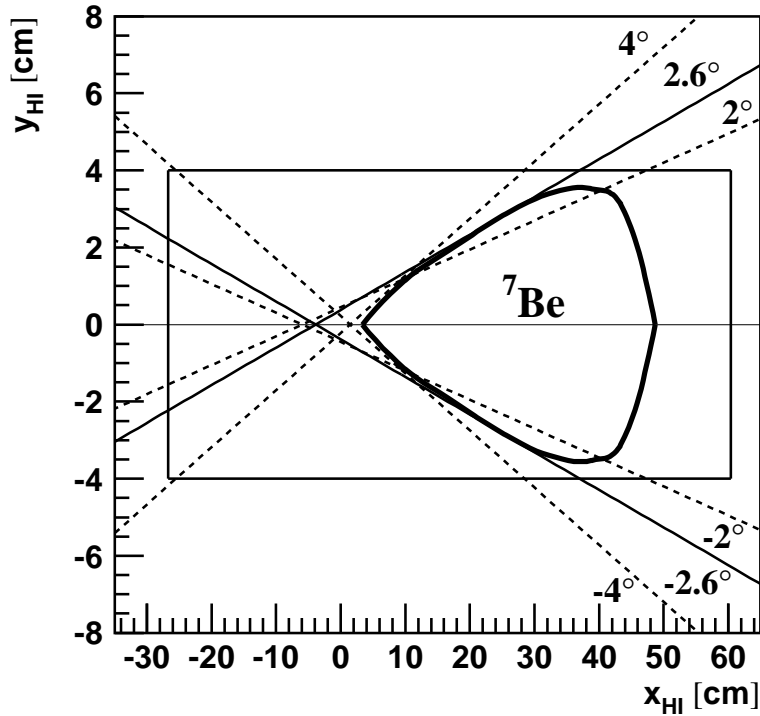


Figure 5.26: The HI detector acceptance in the focal plane obtained by the RAYTRACE code [86]. For the description see the text.

dashed straight lines show the HI positions of the particles for original vertical angles (angles to the horizontal plane) at the target ( $\pm 2^\circ$ ,  $\pm 2.6^\circ$  and  $\pm 4^\circ$ ) and different energies. These are the maximal deviations from the horizontal symmetry plane for particles emitted at those polar angles. The curved thick line encompasses the area which is kinematically allowed for a  ${}^7\text{Be}$  produced in the pionic fusion reaction  ${}^4\text{He}({}^3\text{He}, \pi^0){}^7\text{Be}$  assuming it does not lose kinetic energy. Since the  ${}^7\text{Be}$  energy is significantly lost in the thick liquid  ${}^4\text{He}$  (LHe) target, this area spreads to the lower momentum side. However, all those particles hit the area between the two solid lines associated with the angles  $\pm 2.6^\circ$  which is the maximum allowed by the reaction kinematics.

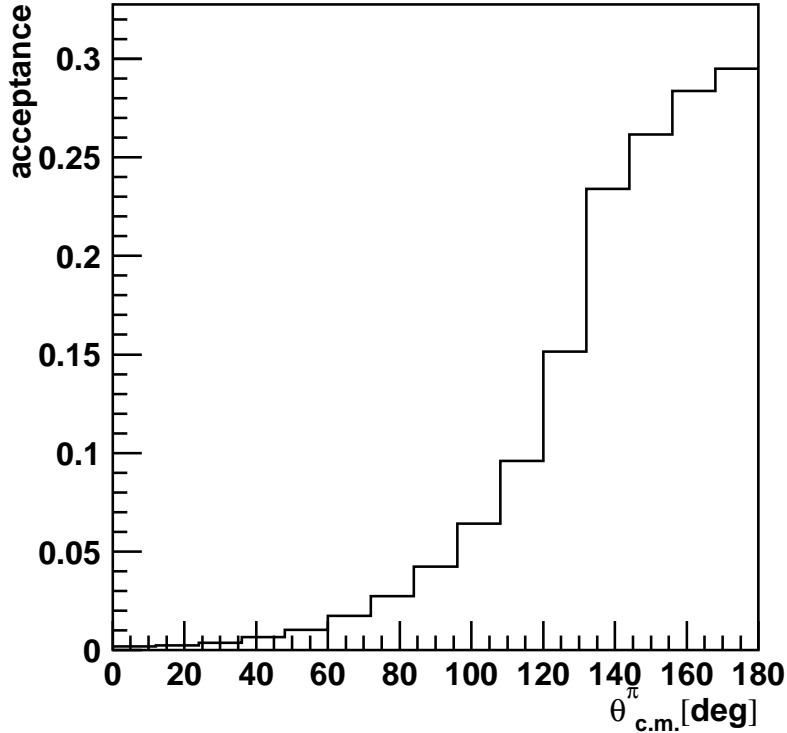


Figure 5.27: The neutral-pion acceptance as function of the pion center-of-mass angle. The acceptance is limited by the low-energy cuts, the absorption of the heavy-ion in the LHe target, the BBS window acceptance and the momentum-bite.

Therefore, all particles with sufficient kinetic energy that entered the BBS, end up in the HI detector. So the acceptance of the detector in the focal plane is only limited by the rigidity of the particles and the rigidity range is obtained from the momentum calibration (Sec. 5.1.1). In the case of the  ${}^3\text{He}+{}^4\text{He}$  experiment, the lowest accepted energy was 86.5 MeV.

The acceptance due to the thick LHe target is also simulated and shown in Fig. 4.6. It is assumed that the reaction can happen uniformly along the target. If the  ${}^7\text{Be}$  ion is produced more deeply in the target it will lose more energy escaping from the target. If the energy drops below the lowest energy

## CHAPTER 5. DATA ANALYSIS

of 86.5 MeV, the particle will not be observed. This acceptance depends on the original energy of the  ${}^7\text{Be}$ , i.e. on the kinematics of the reaction.

The cuts applied on the photon energy depositions ( $>5$  MeV) to reject a huge amount of background, are also taken into account in the calculation of the acceptance. The acceptance as a function of the pion angle is a bin-wise ratio of the number of the events, that passed the above described conditions, to the number of the generated events. It is shown in Fig. 5.27. The number of generated events is large ( $\sim 1000000$ ) and therefore the acceptance uncertainty comes mostly from the uncertainties of the energy cuts due to the energy resolution. The cut conditions are varied within the resolution and that gives an estimate of the acceptance uncertainty of 4%.

## Chapter 6

### Results and discussion

The final distribution obtained by the event selection and the kinematical reconstruction (solid line in Fig. 5.23) was normalized by the measured luminosity, corrected for the dead time and the simulated efficiencies and acceptances to obtain the differential cross section (Fig. 6.1 full circles). Since there is a two-body final state, only one kinematical variable is independent - the center-of-mass pion polar angle. The reaction possesses a cylindrical symmetry around the beam axis and the distribution with respect to the azimuthal pion angle is flat, i.e. the differential cross section does not depend on it.

As can be seen from the distribution in Fig. 6.1, the forward angles are not covered due to the limited acceptance. On the one hand, the PB coverage of the forward angles is smaller than for the backward hemisphere and on the other hand, forward emitted pions are related kinematically to the low-energy beryllium ions which are suppressed due to the absorption in the target and the momentum bite of the spectrometer (see Fig. 4.9). The errors shown in this plot are purely statistical.

The obtained limited distribution can be extrapolated to the whole phase space by expanding the distribution in a series of the Legendre polynomials. In the near-threshold region it is expected that only low partial waves participate in the reaction and for the description of the process only a few of them are sufficient to fit the data.

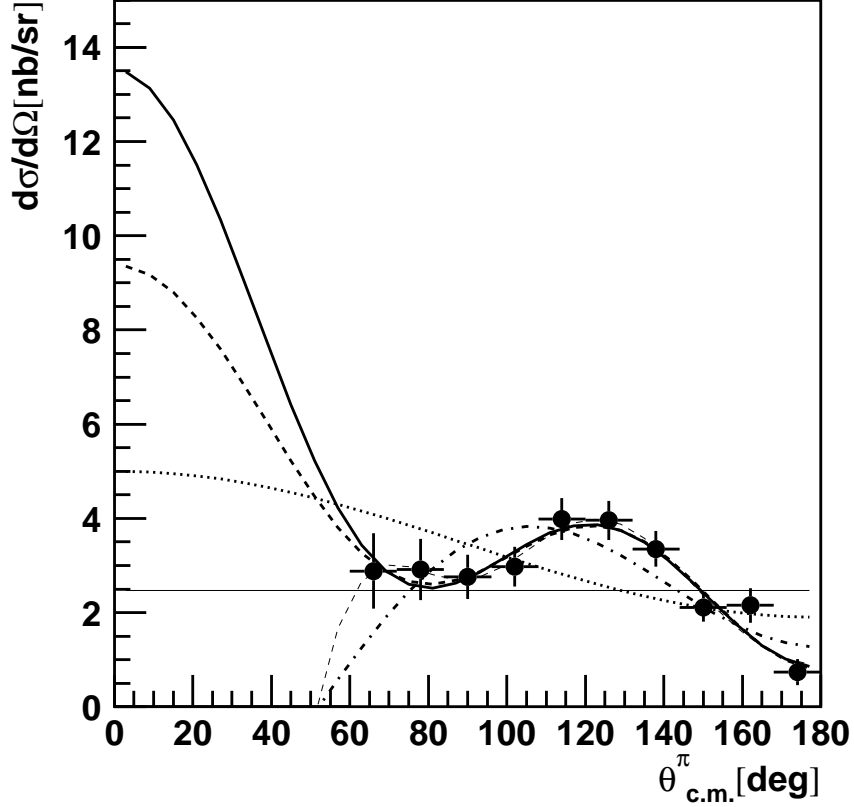


Figure 6.1: The measured differential cross section of the pionic fusion reaction  ${}^4\text{He}({}^3\text{He},\pi^0){}^7\text{Be}$  (full circles) and fit series of Legendre polynomials up to the 0th (thin solid), 1st (dashed), 2nd (dot-dashed), 3rd (solid), 4th (dashed), and 5th (thin dashed) polynomial order.

The Legendre polynomial expansion of the differential cross section is given by

$$\left(\frac{d\sigma}{d\Omega}\right)_{c.m.} = \sum_{k=0} a_k P_k(\cos\theta_{c.m.}) \quad (6.1)$$

The fit curves up to the 5th Legendre polynomial are shown in Fig. 6.1. The fit parameters for different order of expansion are shown in Table 6.1. The goodness of fit is given by the  $\chi^2$  per degree of freedom. The best fit is ob-

## CHAPTER 6. RESULTS AND DISCUSSION

Table 6.1: The results of the Legendre polynomial fit of the measured differential cross section for different orders.

degree	$\frac{\chi^2}{N_f}$	$a_0$	$a_1$	$a_2$	$a_3$	$a_4$	$a_5$
0	8.19	$2.5 \pm 0.1$					
1	6.34	$3.5 \pm 0.2$	$1.6 \pm 0.3$				
2	2.90	$1.8 \pm 0.4$	$-2.7 \pm 0.8$	$-3.2 \pm 0.6$			
3	1.00	$4.2 \pm 0.7$	$3 \pm 2$	$3 \pm 2$	$3.4 \pm 0.9$		
4	1.18	$3.8 \pm 0.7$	$1.8 \pm 1.7$	$1.7 \pm 1.9$	$2.5 \pm 1.5$	$-0.4 \pm 0.7$	
5	1.31	$0.2 \pm 0.6$	$-7 \pm 2$	$-10 \pm 2$	$-7 \pm 2$	$-6 \pm 1$	$-1.9 \pm 0.7$

tained for the 3rd order. This agrees with the analysis of the  ${}^6\text{Li}({}^4\text{He}, \pi^0){}^{10}\text{B}$  reaction [57, 58]. The 3rd and 4th order fits are consistent within the errors of the parameters. The coefficients  $a_1$  and  $a_2$  are very uncertain and the distribution is dominated by the  $a_0$  and  $a_3$ . In the 4th order expansion, the last coefficient  $a_4$  is small indicating that the expansion up to the 3rd order is sufficient. The difference between the 3rd and the 4th order curves shows the biggest uncertainties in the forward pion angle region which is expected since the experimental data points are limited to the region  $\theta > 60^\circ$ . The higher 5th order fit gives an unphysical negative cross section.

The Legendre polynomial fit shows that for the proper fit the term with  $\cos^3 \theta$  must be taken into account. That means that the pion d-wave contributes to the reaction otherwise the highest term would be the term with  $\cos^2 \theta$ . Since the center-of-mass energy is slightly above the production threshold, the produced pion has a low energy and therefore the higher partial waves should be suppressed.

From the fit, the total cross section can be evaluated by

$$\sigma_{tot} = 4\pi a_0. \quad (6.2)$$

So the measured total cross section for the reaction  ${}^4\text{He}({}^3\text{He}, \pi^0){}^7\text{Be}$  is

$$\sigma_{tot} = (53 \pm 9) \text{ nb}. \quad (6.3)$$



CHAPTER 6. RESULTS AND DISCUSSION

The error here includes the statistical uncertainties only. In addition there are systematical errors due to the luminosity uncertainty (7%), the acceptance correction (4%) and the remaining background (1%).

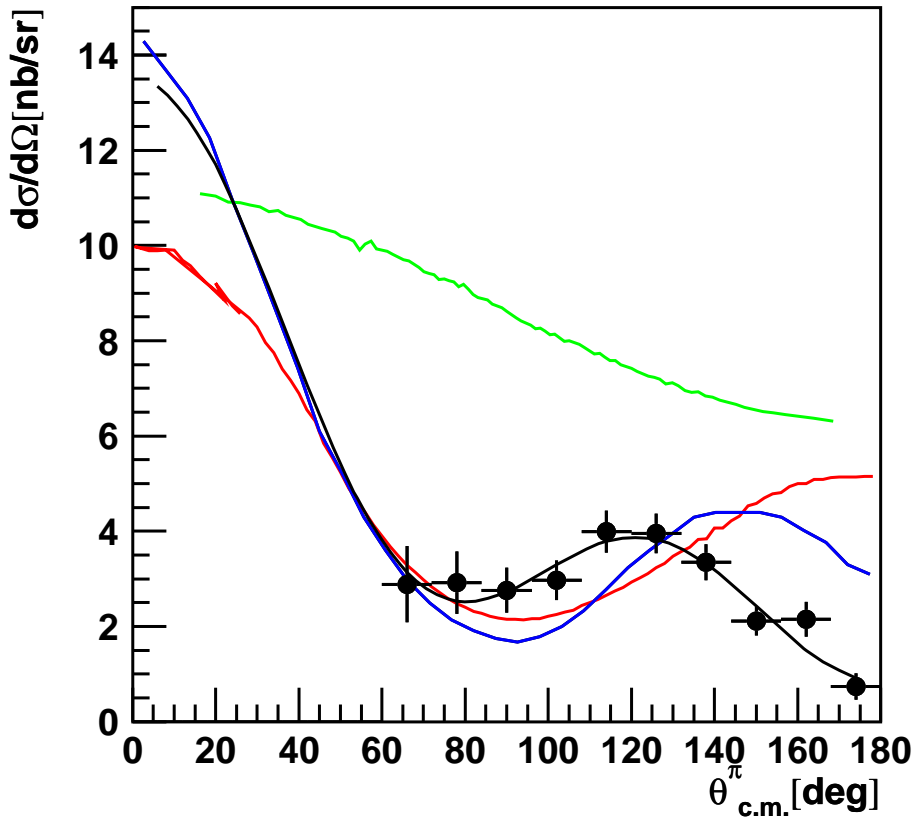


Figure 6.2: The measured differential cross section of the pionic fusion reaction  ${}^4\text{He}({}^3\text{He},\pi^0){}^7\text{Be}$  is shown together compared to predictions from available calculations (red [61], blue [67] and green [64]). The black line shows the best Legendre polynomial fit.

The comparison between the measured differential cross sections and the models is shown in Fig. 6.2. The measured total cross section agrees well with the  $\Delta$ -excitation model [61] (red line) and the cluster model [67] (blue

## CHAPTER 6. RESULTS AND DISCUSSION

line). The measured distribution appears to be slightly shifted to the forward angles compared to the model results. Both models disagree the most in the very backward angles. However, these models exhibit the similar shape of the differential cross section distribution and, therefore, contain a contribution from the ion d-wave. It has to be noted that the beam energy of the measurement (258 MeV) is slightly different than the beam energy used in the model calculations (266.5 MeV).

The semi-empirical model [64] over-predicts the total cross section and shows a different shape of the distribution. It seems that clustering in that model is not appropriate, i.e. the mechanism where one nucleon from the target nucleus in an interaction with the projectile produces the pion is probably not the dominant one.

The  $\Delta$ -model and the cluster model both emphasize the importance of the nuclear cluster structure in the final state which has to match the initial relative motion of the projectile and the target.

Interesting is the very good agreement between the two models although they use different production mechanisms. The first neglects the one-body non-resonant pion production and uses the production via the  $\Delta$ -resonance only, while the other neglects the  $\Delta$ . The  $\Delta$ -resonance is a dominant channel in the pion-nucleon interaction unless when the available energy is very close to the production threshold energy or when selection rules suppress this. In the experiment the available energy was very close to the threshold and this would suppress the  $\Delta$  mechanism. However, we investigated not the elementary NN system but a few-body nuclear system and the transition to the  $\Delta$  can be enhanced at lower energies. In fact, this is shown in [60] where the  $\Delta$ -hole excitations are shifted to lower energies and the resonance is broader. It can also be seen in the  $\pi$ -nucleus reactions where the resonant structure is shifted and becomes broader [11]. On the other hand, in [67] it is shown that without the resonant production approximately the same result can be obtained.

The total cross section of the pionic fusion reaction  ${}^4\text{He}({}^3\text{He},\pi^0){}^7\text{Be}$  can be compared to the existing experimental data (Table 1.1). It has been noticed in experimental data that the cross sections of pionic fusion decrease

## CHAPTER 6. RESULTS AND DISCUSSION

drastically with the system size. It would be interesting to see how the new data fit into the observed systematics.

The dependence of the total cross section on the system size is shown in Fig. 6.3. The system size is represented with the average number of nucleons in the target and the projectile. All pionic fusion measurements with energies up to a few tens of MeV above the absolute threshold are taken into account. Also, the total cross sections of the elementary pp [21] and the pd [28] reactions at the same  $\eta = \frac{p_{c.m.}^{\pi}}{m_{\pi}} = 0.4$  are included.

The system-size dependence is clearly seen and the new data agree well with the trend. However, large uncertainties in the cross section appear due to the other features of the reactions. For instance, the cross section values for the systems with 6 nucleons vary over an order of magnitude because of the different beam energies. The available energy ranges from  $\sim 1$  MeV up to several tens of MeV. It influences the available phase-space and the transition amplitude since different momentum transfers probe the wave functions.

Apart from that, in different reactions different nuclear states are populated. Some experiments can distinguish those states and some do not, which poses an additional problem for the comparison. In general, the pionic fusion reactions lead to bound states where the motion of nucleons within the nucleus, i.e. the nuclear wave function is crucial. Therefore, the number of participating nucleons does not have to be a distinctive factor.

Another property of the reactions that determines the cross section is the isospin of the initial and the final states. example is the comparison of the isospin rotated reactions  ${}^4\text{He}({}^3\text{He}, \pi^0){}^7\text{Be}$  and  ${}^4\text{He}({}^3\text{He}, \pi^+){}^7\text{Li}$ . Although the same number of nucleons is involved in the reactions and the kinematics is approximately the same, their cross sections differ by a factor of two.

But despite the differences between the reactions, on the large scale the number of participating nucleons in the reaction plays an important role. One would expect that the system size is dominant effect in inclusive pion production reactions at higher beam energies per nucleon (about the free NN threshold). The pion is than produced in the continuum and the production cross section depends on the available phase space which in turn depends on the system size. It has been shown [31] in such reactions that the production

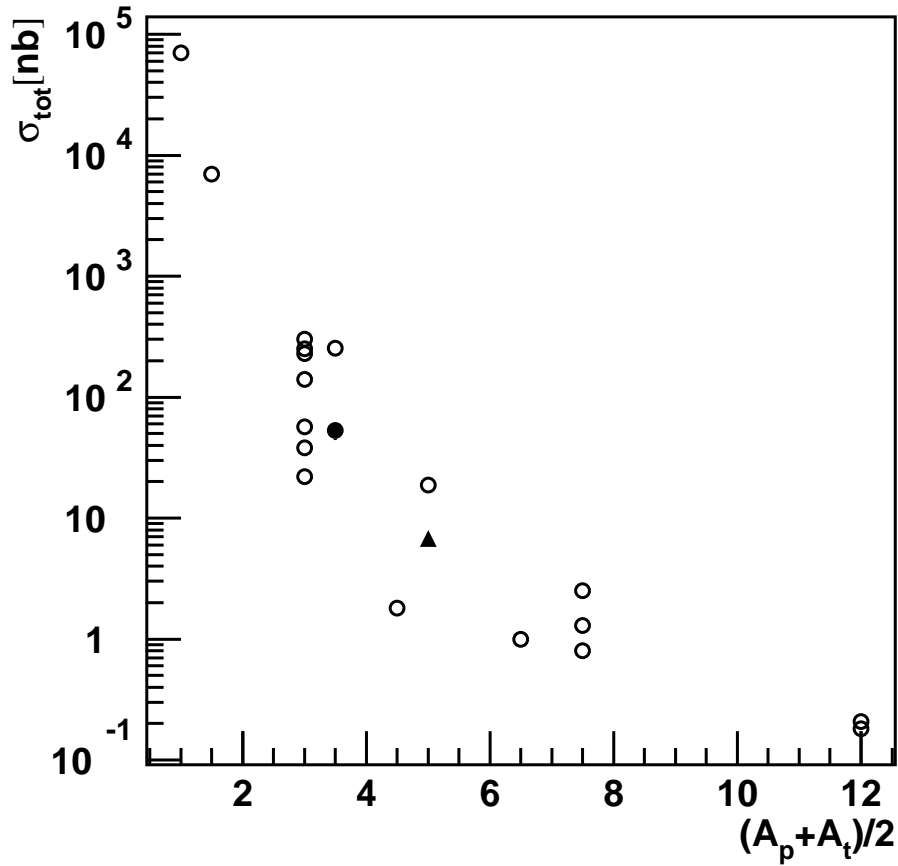


Figure 6.3: Total cross section of pionic fusion reactions as function of the average number of nucleons in projectile and target. The empty circles represent the existing data from [9, 21, 28, 44–46, 48–52, 55]. The full circle and triangle represent the new data from this work and [57], respectively.

cross section scales with the number of possible individual NN collisions which is proportional to the  $A_t A_p$ . This indicates that the most of the pions are produced in the individual NN collisions. It is clear that such scenario is impossible in the pionic fusion since here all nucleons must necessarily participate in the reaction. Data show that the probability of coherence decreases when the number of nucleons in the reaction increases.

## Chapter 7

### Conclusions and outlook

Two pionic-fusion experiments were carried out at KVI in Groningen, the Netherlands. A neutral pion production at the center-of-mass energies of only 10 MeV above the absolute threshold is measured for reactions  ${}^4\text{He}({}^3\text{He},\pi^0){}^7\text{Be}$  and  ${}^6\text{Li}({}^4\text{He},\pi^0){}^{10}\text{B}$  [57, 58].

The pionic-fusion reaction is an extreme example of a nuclear reaction where almost all available energy is converted into one pion. The appearance of such reactions points to the ultimate coherence of all nucleons available in the reaction. Therefore, the nuclear structure of produced bound states and its coupling to the initial relative motion of the projectile and the target is crucial. A mechanism which would provide a satisfactory explanation of such reactions is still insufficiently known. Apart from that, the pion production at threshold is a process of high momentum transfer and consequently probes the high-momentum part of the nuclear wave function. These components are associated to the short-range correlations between the nucleons. Moreover, the reactions near threshold are suitable for study because of the limited phase space and therefore, the simpler treatment of the configurations in the initial and the final state.

Since the experimental data of the pionic fusion reactions is scarce, new measurements are necessary to improve the understanding of the reaction mechanism and to give more insight into the high-momentum parts of the nuclear wave functions.

## CHAPTER 7. CONCLUSIONS AND OUTLOOK

In the experiment described in this work, all produced particles in the final state have been detected in coincidence. For that purpose a complex detection system measuring different types of final-state particles was developed, tested, and applied. The neutral pion decays in the target and is detected via its two-photon decay in different groups of detectors. The Plastic Ball detector covers 70% of the full solid angle and has a granularity of about 17 msr. It is of phoswich nature and allows a discrimination between photons and charged background protons. The plastic scintillator provided fast signals for the trigger and timing purposes. Because of the poor photon energy response (resolution and efficiency) it is equipped with the Inner Shell active converter which partially removes those weaknesses. The large solid angle coverage and the great granularity together with the improved resolution and efficiency make this photon detection system very suitable for the neutral pion detection. A possible upgrade of the Inner Shell detector at forward angles would largely enhance the performance.

The fused nuclei have been detected and identified by the system consisting of the Big-Bite-Spectrometer and the new Heavy-Ion detector array installed in the focal plane of the spectrometer. Such configuration provides a powerful tool for particle identification up to  $Z \leq 5$  on the basis of the momentum analysis, the pulse-shape discrimination, and the time-of-flight measurement.

In order to achieve a high luminosity, the liquid helium target was used in the experiment. The thickness of the target was such that considerable amount of the energy of the produced nucleus was deposited in the target. A thinner liquid helium target would absorb relatively too much energy which would prevent it to stay in the liquid state. The large energy loss of the produced nucleus is successfully overcome in the data analysis with a help of the simulations. Another option for the target would be a gaseous target which has a thickness of 8 orders of magnitude smaller than the liquid one (e.g. [9]) and needs much higher beam currents to reach a sufficient luminosity. Also, it requires special care in the determination of the target thickness.

About 500 background-free pionic-fusion events are selected and their kinematics is determined by the reconstruction of measured angles and the

## CHAPTER 7. CONCLUSIONS AND OUTLOOK

energy of one photon. Since the resolutions in angles and especially in the photon energy measurement distort the kinematics, the real distribution is obtained by unfolding the measured one. For this purpose, a simulation of the reaction kinematics, the detector response and the analysis is used. The measured differential cross sections are extrapolated over the full angular range by the expansion in the series of the Legendre polynomials.

The measured data is compared to the available models for the  ${}^4\text{He}({}^3\text{He},\pi^0){}^7\text{Be}$  reaction. It is shown that coherent models like the  $\Delta$ -excitation model [61] and the interacting cluster model [67] reproduce the measured total cross section well. The agreement for the differential cross sections is less satisfactorily but it shows some common features like the forward-backward asymmetry and the unexpected appearance of the pion d-wave.

The very good agreement between the two models is surprising since they use different production mechanisms. The first uses the  $\Delta$ -resonance intermediate state only, whereas the latter uses the non-resonant pion production only. Both take the clustering structure of the fused nucleus into account, so that might be the most dominant part of the theory. In order to reconcile these two approaches and to separate contributions from the production operator and the final nuclear wave function, a consistent calculation should be done with all different mechanisms taken into account. That also includes the neglected s-wave production contributions which are expected to dominate at the threshold.

The third model based on the semi-empirical approach [64] does not reproduce the measured data, neither in the absolute cross section, nor in the shape of the angular distribution.

The measured total cross section is also compared with the available measured cross sections of other pionic-fusion reactions. The system-size dependence is studied and the new data fit in the overall trend where the total cross section steeply decreases over several orders of magnitude with an increase of the system size of several nucleons. Also it is noticed that the total cross sections depends strongly on the beam energy, the isospin channel, and the nuclear structure of the target, the projectile and the final-state nucleus.

The need for more experimental data is obvious when different pionic-

## CHAPTER 7. CONCLUSIONS AND OUTLOOK

fusion reactions are compared. There are many parameters which have to be disentangled - the available energy, the nuclear structure, the kinematics of the reaction, the system size and the covered phase space. The data taken at different energies above the absolute threshold would allow to study contributions of different mechanisms with energy change. Also the full angular coverage is necessary to clearly disentangle different partial waves. Once, the reaction mechanism is well known, the pion fusion reaction can be used as a unique probe of the high-momentum components of the nuclear wave functions.



## Bibliography

- [1] E. Epelbaum et al., *Rev. Mod. Phys.* 81, 1773 (2009).
- [2] S. Dürr et al., *Science* 322, 1224 (2008).
- [3] H. Yukawa, *Proc. Phys. Math. Soc. Japan* 17, 48 (1935).
- [4] C.M.G. Lattes et al., *Nature* 160, 453, 486 (1947).
- [5] E. Gardner and C.M.G. Lattes, *Science* 107, 270 (1948).
- [6] J. Steinberger, W.K.H. Panofsky, and J. Steller, *Phys.Rev.* 78, 802 (1950).
- [7] A.K. Opper et al., *Phys. Rev. Lett.* 91, 212302 (2003).
- [8] E.J. Stephenson et al., *Phys. Rev. Lett.* 91, 142302 (2003).
- [9] M. Andersson et al., *Nucl. Phys. A* 779, 47 (2006).
- [10] T.E.O. Ericson and W. Weise, *Pions in Nuclei*, Oxford University Press, Oxford, England (1988).
- [11] T.-S.H. Lee and R.P. Redwine, *Annu. Rev. Nucl. Part. Sci.* 52, 23 (2002).
- [12] H. Machner and J. Haidenbauer, *J. Phys. G* 25 R231 (1999).
- [13] P. Moskal et al., *Prog. Part. Nucl. Phys.* 49, 1 (2002).
- [14] C. Hanhart, *Phys. Rep.* 397, 155 (2004).
- [15] B.J. VerWest and R.A. Arndt, *Phys. Rev. C* 25, 1979 (1982).

## BIBLIOGRAPHY

- [16] D.S. Koltun and A. Reitan, Phys. Rev. 141, 1413 (1966).
- [17] H.O. Meyer et al., Phys. Rev. Lett. 65, 2846 (1990).
- [18] H.O. Meyer et al., Nucl. Phys. A 539, 633 (1992).
- [19] A. Bondar et al., Phys. Lett. B 356, 8 (1995).
- [20] W.W. Daehnick et al., Phys. Rev. Lett. 74, 2913 (1995).
- [21] M. Drochner et al., Nucl. Phys. A 643, 55 (1998).
- [22] C. Hanhart et al., Phys. Rev. C 61, 064008 (2000).
- [23] H.O. Meyer et al., Phys. Rev. C 63, 064002 (2001).
- [24] W.W. Daehnick et al., Phys. Rev. C 65, 024003 (2002).
- [25] B.v. Przewoski et al., Phys. Rev. C 61, 064604 (2000).
- [26] V. Baru, EPJ Web of Conferences 3, 03003 (2010).
- [27] J.A. Niskanen, Phys. Lett. B 289, 227 (1992).
- [28] M. Betigeri et al., Nucl. Phys. A 690, 473 (2001).
- [29] W.G. McMillan and E. Teller, Phys. Rev. 72, 1 (1947).
- [30] P. Braun-Munzinger and Johanna Stachel, Ann. Rev. Nucl. Part. Sci. 37, 97 (1987).
- [31] W. Cassing et al., Phys. Rep. 188, 363 (1990).
- [32] A. Bonasera, R. Coniglione, and P. Sapienza, Eur. Phys. J. A 30, 47 (2006).
- [33] W. Reisdorf et al., Nucl. Phys. A 781, 459 (2007).
- [34] G.F. Bertsch, Phys. Rev. C 15, 713 (1977).
- [35] R. Shyam and J. Knoll, Phys. Lett. B 136, 221 (1984).

## BIBLIOGRAPHY

- [36] S. Dahlgren et al., Phys. Lett. B 35, 219 (1971).
- [37] H.W. Fearing, Prog. Part. Nucl. Phys. 7, 113 (1981).
- [38] H.W. Wilschut et al., Phys. Rev C 65, 014610 (2001).
- [39] J. Eggermann et al., Z. Phys A 273, 381 (1975).
- [40] T.E. Ward, Phys. Rev. C 36, 2680 (1987).
- [41] E. Aslanides et al., Phys. Rev. Lett. 43, 1466 (1979), Phys. Rev. Lett. 45, 1738 (1980).
- [42] T. Bressani et al., Phys. Rev. C 30, 1745 (1984).
- [43] E. Aslanides et al., Phys. Lett. B 108, 91 (1982).
- [44] Y. Le Bornec et al., Phys. Rev. Lett. 47, 1870 (1981).
- [45] Y. Le Bornec et al., Phys. Lett. B 133, 149 (1983).
- [46] L. Bimbot et al., Phys. Lett. B 114, 311, (1982).
- [47] N. Willis et al., Phys. Lett. B 136, 334 (1984).
- [48] L. Bimbot et al., Phys. Rev. C 30, 739, (1984).
- [49] W. Schott et al., Phys. Rev. C 34, 1406 (1986).
- [50] J. Homolka et al., Phys. Rev. C 38, 2686 (1988).
- [51] D. Horn et al., Phys. Rev. Lett. 77, 2408 (1996).
- [52] M. Andersson et al., Phys. Lett. B 481, 165 (2000), Phys. Lett. B 484, 375 (2000).
- [53] M. Andersson et al., Acta Phys. Pol. B 31, 2343 (2000).
- [54] M. Andersson et al., Phys. Atom. Nucl. 65, 628 (2002).
- [55] M. Andersson et al., Phys. Scr. T104, 96 (2003).

## BIBLIOGRAPHY

- [56] M. Andersson et al., Phys. Scr. T104, 105 (2003).
- [57] L. Joulaeizadeh et al., Phys. Lett. B 694, 310 (2011).
- [58] L. Joulaeizadeh, PhD thesis, University of Groningen (2009).
- [59] K. Klingenbeck, M. Dillig, and M.G. Huber, Phys. Rev. Lett. 47, 1654 (1981).
- [60] M.G. Huber and K. Klingenbeck, AIP Conf. Proc. 79, Pion Production and Absorption in Nuclei (IUCF), Ed. R.D. Bent, AIP, New York (1982).
- [61] M.G. Huber, K. Klingenbeck, and R. Hupke, Nucl. Phys. A 396, 191c (1983).
- [62] L. Harzheim et al., Z. Phys. A 340, 399 (1991).
- [63] J.-F. Germond and C. Wilkin, Phys. Lett. B 106, 449 (1981).
- [64] J.-F. Germond and C. Wilkin, J. Phys. G 10, 745 (1984).
- [65] J.-F. Germond and C. Wilkin, J. Phys. G 16, 381 (1990).
- [66] G. Fäldt and C. Wilkin, Phys. Lett. B 486, 67 (2000).
- [67] T. Kajino, H. Toki, and K. Kubo, Phys. Rev. C 35, 1370 (1987).
- [68] J.A. Wheeler, Phys. Rev. 52, 1083 (1937); Phys. Rev. 52, 1107 (1937).
- [69] D.R. Tilley et al., Nucl. Phys. A 708, 3 (2002).
- [70] A. Baden et al., Nucl. Instr. and Meth. 203, 189 (1982).
- [71] L. Joulaeizadeh et al., Nucl. Instr. and Meth. A 622, 176 (2010).
- [72] A.M. van den Berg, Nucl. Instr. and Meth. B 99, 637 (1995).
- [73] I. Gasparic et al., Nucl. Instr. and Meth. A 631, 62 (2011).
- [74] P. Dendooven and H. Timersma, private communication.
- [75] <<http://www.scionix.nl>>, The Netherlands.

## *BIBLIOGRAPHY*

- [76] M. Kis, PhD thesis, University of Groningen (2005).
- [77] M. Mahjour-Shafiei et al., Phys. Lett. B 632, 480 (2006).
- [78] R. Brun, F. Bruyant, A.C. McPherson and P. Zancarini, GEANT3, CERN Report DD/EE/84-1 (1986), unpublished.
- [79] F. Zwarts, KVI DAQ software, KVI Groningen (2006).
- [80] GENBOD, CERN Program Library Long Write-up W515 (1993).
- [81] J.D. Valentine et al., Nucl. Instr. and Meth. A 325, 147 (1993).
- [82] D. Horn et al., Nucl. Instr. and Meth. A 320, 273 (1992).
- [83] M. Pârlog et al., Nucl. Instr. and Meth. A 482, 674 (2002).
- [84] M. Pârlog et al., Nucl. Instr. and Meth. A 482, 693 (2002).
- [85] D. Fox et al., Nucl. Instr. and Meth. A 374, 63 (1996).
- [86] S. Kowalski and H.A. Enge, Nucl. Instr. and Meth. A 258, 407 (1987).

## Curriculum vitae

Igor Gašparić was born on the 22nd of April 1975 in Čakovec, Croatia. He attended a primary school in Čakovec and a grammar school in Varaždin. From 1993 to 1999 he studied physics at the Faculty of Science, University of Zagreb. His diploma thesis titled "Density of states in the interacting boson model with broken pairs" under the supervision of Prof. Slobodan Brant was defended on the 20th of December 1999. Since 2000 he has been employed as a research assistant in the Laboratory for Heavy-Ion Physics (since 2008 in the Laboratory for Nuclear Physics) of the Division of Experimental Physics at the Ruđer Bošković Institute in Zagreb and a postgraduate student in experimental nuclear physics at University of Zagreb. He has been involved in the FOPI collaboration at the Gesellschaft für Schwerionenforschung (GSI) in Darmstadt, Germany and at the Kernfysisch Versneller Instituut (KVI) in Groningen, The Netherlands. This doctoral thesis is the result of the work done at KVI.

He is married and has three children.

## List of CC publications

1. I. Gašparić et al., Nucl. Instr. and Meth. A 631, 62 (2011),
2. L. Joulaeizadeh, I. Gašparić et al., Phys. Lett. B 694, 310 (2011),
3. A. Ramazani-Moghaddam-Arani et al., Phys. Rev. C 83, 024002 (2011),
4. L. Joulaeizadeh, I. Gašparić et al., Nucl. Instr. and Meth. A 622, 176 (2010),
5. X. Lopez et al., Phys. Rev. C 81, 061902 (2010),
6. L. Joulaeizadeh et al., Int. J. Mod. Phys. A 24, 539 (2009),
7. M. Mahjour-Shafiei et al., Eur. Phys. J. A 41, 25 (2009),
8. M.L. Benabderrahmane et al., Phys. Rev. Lett. 102, 182501 (2009),
9. A. Ramazani-Moghaddam-Arani et al., Mod. Phys. Lett. A 24, 835 (2009),
10. M. Eslami-Kalantari et al., Mod. Phys. Lett. A 24, 839 (2009),
11. A. Ramazani-Moghaddam-Arani et al., Phys. Rev. C 78, 014006 (2008),
12. A. Ramazani-Moghaddam-Arani et al., Few-Body Syst. 44, 27 (2008),
13. X. Lopez et al., Phys. Rev. C 76, 052203 (2007),
14. M. Merschmeyer et al., Phys. Rev. C 76, 024906 (2007),

*LIST OF CC PUBLICATIONS*

15. X. Lopez et al., Phys. Rev. C 75, 011901 (2007),
16. M. Mahjour-Shafiei et al., Phys. Lett. B 632, 480 (2006),
17. N. Bastid et al., Phys. Rev. C 72, 011901 (2005),
18. A. Andronic et al., Phys. Lett. B 612, 173 (2005),
19. R. Kotte et al., Eur. J. Phys. A 23, 271 (2005),
20. N. Bastid et al., Nucl. Phys. A 742, 29 (2004),
21. R. Čaplar et al., Acta Phys. Hung. 19, 163 (2004).